

THE UNIVERSITY OF CALGARY

Drag Reduction with Riblets in Pipe Flow

by

Marvin Harvey Weiss

A DISSERTATION

SUBMITTED TO THE FACULTY OF GRADUATE STUDIES
IN PARTIAL FULFILLMENT OF THE REQUIREMENTS FOR THE
DEGREE OF DOCTOR OF PHILOSOPHY

DEPARTMENT OF MECHANICAL ENGINEERING

CALGARY, ALBERTA

SEPTEMBER, 1993

© Marvin Harvey Weiss 1993

THE UNIVERSITY OF CALGARY
FACULTY OF GRADUATE STUDIES

The undersigned certify that they have read, and recommend to the Faculty of Graduate Studies for acceptance, a dissertation entitled "Drag Reduction with Riblets in Pipe Flow" submitted by Marvin Harvey Weiss in partial fulfillment of the requirements for the degree of Doctor of Philosophy.



Dr. G. Walker, Supervisor
Department of Mechanical Engineering



Dr. R. D. Rowe
Department of Mechanical Engineering



Dr. A. A. Jeje
Department of Chemical and Petroleum Engineering



Dr. E. Rhodes
Department of Chemical and Petroleum Engineering



Dr. C.R. Smith, External Examiner
Lehigh University

5 Oct 93
Date



National Library
of Canada

Acquisitions and
Bibliographic Services Branch

395 Wellington Street
Ottawa, Ontario
K1A 0N4

Bibliothèque nationale
du Canada

Direction des acquisitions et
des services bibliographiques

395, rue Wellington
Ottawa (Ontario)
K1A 0N4

Your file *Votre référence*

Our file *Notre référence*

The author has granted an irrevocable non-exclusive licence allowing the National Library of Canada to reproduce, loan, distribute or sell copies of his/her thesis by any means and in any form or format, making this thesis available to interested persons.

L'auteur a accordé une licence irrévocable et non exclusive permettant à la Bibliothèque nationale du Canada de reproduire, prêter, distribuer ou vendre des copies de sa thèse de quelque manière et sous quelque forme que ce soit pour mettre des exemplaires de cette thèse à la disposition des personnes intéressées.

The author retains ownership of the copyright in his/her thesis. Neither the thesis nor substantial extracts from it may be printed or otherwise reproduced without his/her permission.

L'auteur conserve la propriété du droit d'auteur qui protège sa thèse. Ni la thèse ni des extraits substantiels de celle-ci ne doivent être imprimés ou autrement reproduits sans son autorisation.

ISBN 0-315-94001-8

Canada

Name Marrin Harvey Weiss

Dissertation Abstracts International is arranged by broad, general subject categories. Please select the one subject which most nearly describes the content of your dissertation. Enter the corresponding four-digit code in the spaces provided.

Engineering - Mechanical

SUBJECT TERM

0548

U·M·I

SUBJECT CODE

Subject Categories

THE HUMANITIES AND SOCIAL SCIENCES

COMMUNICATIONS AND THE ARTS

Architecture 0729
Art History 0377
Cinema 0900
Dance 0378
Fine Arts 0357
Information Science 0723
Journalism 0391
Library Science 0399
Mass Communications 0708
Music 0413
Speech Communication 0459
Theater 0465

EDUCATION

General 0515
Administration 0514
Adult and Continuing 0516
Agricultural 0517
Art 0273
Bilingual and Multicultural 0282
Business 0688
Community College 0275
Curriculum and Instruction 0727
Early Childhood 0518
Elementary 0524
Finance 0277
Guidance and Counseling 0519
Health 0680
Higher 0745
History of 0520
Home Economics 0278
Industrial 0521
Language and Literature 0279
Mathematics 0280
Music 0522
Philosophy of 0998
Physical 0523

Psychology 0525
Reading 0535
Religious 0527
Sciences 0714
Secondary 0533
Social Sciences 0534
Sociology of 0340
Special 0529
Teacher Training 0530
Technology 0710
Tests and Measurements 0288
Vocational 0747

LANGUAGE, LITERATURE AND LINGUISTICS

Language
General 0679
Ancient 0289
Linguistics 0290
Modern 0291
Literature
General 0401
Classical 0294
Comparative 0295
Medieval 0297
Modern 0298
African 0316
American 0591
Asian 0305
Canadian (English) 0352
Canadian (French) 0355
English 0593
Germanic 0311
Latin American 0312
Middle Eastern 0315
Romance 0313
Slavic and East European 0314

PHILOSOPHY, RELIGION AND THEOLOGY

Philosophy 0422
Religion
General 0318
Biblical Studies 0321
Clergy 0319
History of 0320
Philosophy of 0322
Theology 0469

SOCIAL SCIENCES

American Studies 0323
Anthropology
Archaeology 0324
Cultural 0326
Physical 0327
Business Administration
General 0310
Accounting 0272
Banking 0770
Management 0454
Marketing 0338
Canadian Studies 0385
Economics
General 0501
Agricultural 0503
Commerce-Business 0505
Finance 0508
History 0509
Labor 0510
Theory 0511
Folklore 0358
Geography 0366
Gerontology 0351
History
General 0578

Ancient 0579
Medieval 0581
Modern 0582
Black 0328
African 0331
Asia, Australia and Oceania 0332
Canadian 0334
European 0335
Latin American 0336
Middle Eastern 0333
United States 0337
History of Science 0585
Law 0398
Political Science
General 0615
International Law and Relations 0616
Public Administration 0617
Recreation 0814
Social Work 0452
Sociology
General 0626
Criminology and Penology 0627
Demography 0938
Ethnic and Racial Studies 0631
Individual and Family Studies 0628
Industrial and Labor Relations 0629
Public and Social Welfare 0630
Social Structure and Development 0700
Theory and Methods 0344
Transportation 0709
Urban and Regional Planning 0999
Women's Studies 0453

THE SCIENCES AND ENGINEERING

BIOLOGICAL SCIENCES

Agriculture
General 0473
Agronomy 0285
Animal Culture and Nutrition 0475
Animal Pathology 0476
Food Science and Technology 0359
Forestry and Wildlife 0478
Plant Culture 0479
Plant Pathology 0480
Plant Physiology 0817
Range Management 0777
Wood Technology 0746
Biology
General 0306
Anatomy 0287
Biostatistics 0308
Botany 0309
Cell 0379
Ecology 0329
Entomology 0353
Genetics 0369
Limnology 0793
Microbiology 0410
Molecular 0307
Neuroscience 0317
Oceanography 0416
Physiology 0433
Radiation 0821
Veterinary Science 0778
Zoology 0472
Biophysics
General 0786
Medical 0760
EARTH SCIENCES
Biogeochemistry 0425
Geochemistry 0996

Geodesy 0370
Geology 0372
Geophysics 0373
Hydrology 0388
Mineralogy 0411
Paleobotany 0345
Paleoecology 0426
Paleontology 0418
Paleozoology 0985
Palynology 0427
Physical Geography 0368
Physical Oceanography 0415

HEALTH AND ENVIRONMENTAL SCIENCES

Environmental Sciences 0768
Health Sciences
General 0566
Audiology 0300
Chemotherapy 0992
Dentistry 0567
Education 0350
Hospital Management 0769
Human Development 0758
Immunology 0982
Medicine and Surgery 0564
Mental Health 0347
Nursing 0569
Nutrition 0570
Obstetrics and Gynecology 0380
Occupational Health and Therapy 0354
Ophthalmology 0381
Pathology 0571
Pharmacology 0419
Pharmacy 0572
Physical Therapy 0382
Public Health 0573
Radiology 0574
Recreation 0575

Speech Pathology 0460
Toxicology 0383
Home Economics 0386

PHYSICAL SCIENCES

Pure Sciences

Chemistry
General 0485
Agricultural 0749
Analytical 0486
Biochemistry 0487
Inorganic 0488
Nuclear 0738
Organic 0490
Pharmaceutical 0491
Physical 0494
Polymer 0495
Radiation 0754
Mathematics 0405
Physics
General 0605
Acoustics 0986
Astronomy and Astrophysics 0606
Atmospheric Science 0608
Atomic 0748
Electronics and Electricity 0607
Elementary Particles and High Energy 0798
Fluid and Plasma 0759
Molecular 0609
Nuclear 0610
Optics 0752
Radiation 0756
Solid State 0611
Statistics 0463

Applied Sciences

Applied Mechanics 0346
Computer Science 0984

Engineering
General 0537
Aerospace 0538
Agricultural 0539
Automotive 0540
Biomedical 0541
Chemical 0542
Civil 0543
Electronics and Electrical 0544
Heat and Thermodynamics 0348
Hydraulic 0545
Industrial 0546
Marine 0547
Materials Science 0794
Mechanical 0548
Metallurgy 0743
Mining 0551
Nuclear 0552
Packaging 0549
Petroleum 0765
Sanitary and Municipal 0554
System Science 0790
Geotechnology 0428
Operations Research 0796
Plastics Technology 0795
Textile Technology 0994

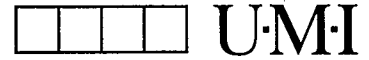
PSYCHOLOGY

General 0621
Behavioral 0384
Clinical 0622
Developmental 0620
Experimental 0623
Industrial 0624
Personality 0625
Physiological 0989
Psychobiology 0349
Psychometrics 0632
Social 0451



Nom _____

Dissertation Abstracts International est organisé en catégories de sujets. Veuillez s.v.p. choisir le sujet qui décrit le mieux votre thèse et inscrivez le code numérique approprié dans l'espace réservé ci-dessous.



SUJET

CODE DE SUJET

Catégories par sujets

HUMANITÉS ET SCIENCES SOCIALES

COMMUNICATIONS ET LES ARTS

Architecture 0729
 Beaux-arts 0357
 Bibliothéconomie 0399
 Cinéma 0900
 Communication verbale 0459
 Communications 0708
 Danse 0378
 Histoire de l'art 0377
 Journalisme 0391
 Musique 0413
 Sciences de l'informatique 0723
 Théâtre 0465

ÉDUCATION

Généralités 515
 Administration 0514
 Art 0273
 Collèges communautaires 0275
 Commerce 0688
 Économie domestique 0278
 Éducation permanente 0516
 Éducation préscolaire 0518
 Éducation sanitaire 0680
 Enseignement agricole 0517
 Enseignement bilingue et multiculturel 0282
 Enseignement industriel 0521
 Enseignement primaire 0524
 Enseignement professionnel 0747
 Enseignement religieux 0527
 Enseignement secondaire 0533
 Enseignement spécial 0529
 Enseignement supérieur 0745
 Évaluation 0288
 Finances 0277
 Formation des enseignants 0530
 Histoire de l'éducation 0520
 Langues et littérature 0279

Lecture 0535
 Mathématiques 0280
 Musique 0522
 Orientation et consultation 0519
 Philosophie de l'éducation 0998
 Physique 0523
 Programmes d'études et enseignement 0727
 Psychologie 0525
 Sciences 0714
 Sciences sociales 0534
 Sociologie de l'éducation 0340
 Technologie 0710

LANGUE, LITTÉRATURE ET LINGUISTIQUE

Langues
 Généralités 0679
 Anciennes 0289
 Linguistique 0290
 Modernes 0291

Littérature
 Généralités 0401
 Anciennes 0294
 Comparée 0295
 Médiévale 0297
 Moderne 0298
 Africaine 0316
 Américaine 0591
 Anglaise 0593
 Asiatique 0305
 Canadienne (Anglaise) 0352
 Canadienne (Française) 0355
 Germanique 0311
 Latino-américaine 0312
 Moyen-orientale 0315
 Romane 0313
 Slave et est-européenne 0314

PHILOSOPHIE, RELIGION ET THEOLOGIE

Philosophie 0422

Religion
 Généralités 0318
 Clergé 0319
 Études bibliques 0321
 Histoire des religions 0320
 Philosophie de la religion 0322

Théologie 0469

SCIENCES SOCIALES

Anthropologie
 Archéologie 0324
 Culturelle 0326
 Physique 0327

Droit 0398

Economie
 Généralités 0501
 Commerce-Affaires 0505
 Économie agricole 0503
 Économie du travail 0510
 Finances 0508
 Histoire 0509
 Théorie 0511

Études américaines 0323
Études canadiennes 0385
Études féministes 0453
Folklore 0358
Géographie 0366
Gérontologie 0351

Gestion des affaires
 Généralités 0310
 Administration 0454
 Banques 0770
 Comptabilité 0272
 Marketing 0338

Histoire
 Histoire générale 0578

Ancienne 0579
 Médiévale 0581
 Moderne 0582
 Histoire des noirs 0328
 Africaine 0331
 Canadienne 0334
 États-Unis 0337
 Européenne 0335
 Moyen-orientale 0333
 Latino-américaine 0336
 Asie, Australie et Océanie 0332

Histoire des sciences 0585
Loisirs 0814
Planification urbaine et régionale 0999
Science politique
 Généralités 0615
 Administration publique 0617
 Droit et relations internationales 0616

Sociologie
 Généralités 0626
 Aide et bien-être social 0630
 Criminologie et établissements pénitentiaires 0627
 Démographie 0938
 Études de l'individu et de la famille 0628
 Études des relations interethniques et des relations raciales 0631
 Structure et développement social 0700
 Théorie et méthodes 0344
 Travail et relations industrielles 0629
 Transports 0709
 Travail social 0452

SCIENCES ET INGÉNIERIE

SCIENCES BIOLOGIQUES

Agriculture
 Généralités 0473
 Agronomie 0285
 Alimentation et technologie alimentaire 0359
 Culture 0479
 Élevage et alimentation 0475
 Exploitation des péturages 0777
 Pathologie animale 0476
 Pathologie végétale 0480
 Physiologie végétale 0817
 Sylviculture et faune 0478
 Technologie du bois 0746

Biologie
 Généralités 0306
 Anatomie 0287
 Biologie (Statistiques) 0308
 Biologie moléculaire 0307
 Botanique 0309
 Cellule 0379
 Écologie 0329
 Entomologie 0353
 Génétique 0369
 Limnologie 0793
 Microbiologie 0410
 Neurologie 0317
 Océanographie 0416
 Physiologie 0433
 Radiation 0821
 Science vétérinaire 0778
 Zoologie 0472

Biophysique
 Généralités 0786
 Médicale 0760

Géologie 0372
 Géophysique 0373
 Hydrologie 0388
 Minéralogie 0411
 Océanographie physique 0415
 Paléobotanique 0345
 Paléocologie 0426
 Paléontologie 0418
 Paléozoologie 0985
 Palynologie 0427

SCIENCES DE LA SANTÉ ET DE L'ENVIRONNEMENT

Économie domestique 0386
 Sciences de l'environnement 0768
 Sciences de la santé

Généralités 0566
 Administration des hôpitaux 0769
 Alimentation et nutrition 0570
 Audiologie 0300
 Chimiothérapie 0992
 Dentisterie 0567
 Développement humain 0758
 Enseignement 0350
 Immunologie 0982
 Loisirs 0575

Médecine du travail et thérapie 0354
Médecine et chirurgie 0564
Obstétrique et gynécologie 0380
Ophthalmologie 0381
Orthophonie 0460
Pathologie 0571
Pharmacie 0572
Pharmacologie 0419
Physiothérapie 0382
Radiologie 0574
Santé mentale 0347
Santé publique 0573
Soins infirmiers 0569
Toxicologie 0383

SCIENCES PHYSIQUES

Sciences Pures
Chimie
 Généralités 0485
 Biochimie 487
 Chimie agricole 0749
 Chimie analytique 0486
 Chimie minérale 0488
 Chimie nucléaire 0738
 Chimie organique 0490
 Chimie pharmaceutique 0491
 Physique 0494
 Polymères 0495
 Radiation 0754

Mathématiques 0405

Physique
 Généralités 0605
 Acoustique 0986
 Astronomie et astrophysique 0606
 Électronique et électricité 0607
 Fluides et plasma 0759
 Météorologie 0608
 Optique 0752
 Particules (Physique nucléaire) 0798
 Physique atomique 0748
 Physique de l'état solide 0611
 Physique moléculaire 0609
 Physique nucléaire 0610
 Radiation 0756

Statistiques 0463

Biomédicale 0541
Chaleur et thermodynamique 0348
Conditionnement (Emballage) 0549
Génie aérospatial 0538
Génie chimique 0542
Génie civil 0543
Génie électronique et électrique 0544
Génie industriel 0546
Génie mécanique 0548
Génie nucléaire 0552
Ingénierie des systèmes 0790
Mécanique navale 0547
Métallurgie 0743
Science des matériaux 0794
Technique du pétrole 0765
Technique minière 0551
Techniques sanitaires et municipales 0554
Technologie hydraulique 0545
Mécanique appliquée 0346
Géotechnologie 0428
Matières plastiques (Technologie) 0795
Recherche opérationnelle 0796
Textiles et tissus (Technologie) 0794

SCIENCES DE LA TERRE

Biogéochimie 0425
 Géochimie 0996
 Géodésie 0370
 Géographie physique 0368

PSYCHOLOGIE
 Généralités 0621
 Personnalité 0625
 Psychobiologie 0349
 Psychologie clinique 0622
 Psychologie du comportement 0384
 Psychologie du développement 0620
 Psychologie expérimentale 0623
 Psychologie industrielle 0624
 Psychologie physiologique 0989
 Psychologie sociale 0451
 Psychométrie 0632



Abstract

An extensive study of pipe flow with small surface grooves, or *riblets*, has been conducted in an attempt to elucidate the mechanism which causes drag reduction in turbulent flow. The effect of the small surface structures was investigated from several perspectives, beginning with measurements of friction factor in smooth and riblet-lined pipes over a wide range of Reynolds numbers utilizing laboratory and field experiments. A complementary theoretical analysis of laminar pipe flow with blade-type riblets was followed by a detailed comparison of turbulence structure in a low Reynolds number turbulent pipe flow over a smooth and a drag-reducing riblet surface.

Careful measurements of friction factor provided unambiguous confirmation of drag reduction in turbulent pipe flow with properly sized riblets. A significant amount of drag reduction occurs even at very small non-dimensional heights. Field applications of riblets may result in even higher levels of drag reduction since, at high Reynolds numbers, even honed pipe walls are no longer hydraulically smooth.

Consideration of viscous effects stressed the importance of knowing the effective diameter when making statements about friction losses in ribbed pipes. Furthermore, scaling parameters based on longitudinal and cross-flow viscous protrusion heights have been deduced which result in an almost universal drag reducing curve for riblets.

Using X-wire anemometry techniques, turbulent statistics along with detailed radial and azimuthal space-correlations of all three velocity components and turbulent shear stress over a smooth and riblet-covered pipe wall were obtained at $Re_b \approx 5500$. New measurements of length scales confirm the existence of intense vortex structures in the near-wall region with a characteristic dimension, perpendicular to the vortex core, of less than 20 wall units. Comparative measurements established that riblets inhibit the induction of lateral flow near the surface, thus hindering the ability of convecting vortices to provoke focused eruptions of the surface shear layer. Specifically, vortex induced cross-flow above the rib peaks creates secondary vorticity of the opposite sense within the rib valley, which tends to weaken any surface layer eruptions. Numerous single-point statistics and two-point space correlations provide support for this drag reduction mechanism.

Acknowledgments

It is a pleasure to express my thanks to those individuals from whom I have benefited throughout the course of this study.

I would especially like to thank my supervisor, Dr. G. Walker, for his support and encouragement, Dr. R.D. Rowe for his interest and helpful advice, and Dr. A.G. Doige for his contribution during the initial stages of this work.

In particular, I am indebted to Dr. Wojciech Studzinski for his foresight, guidance, support of the research, and genuine friendship. Thanks are also due to my colleagues, Prof. Wiktor Jungowski and Dr. Umesh Karnik, for constructive criticisms and numerous valuable discussions, and to Dr. Kamal Botros for his interest and concern.

Financial support from the Natural Sciences and Engineering Research Council (NSERC), the Alberta Heritage Scholarship Fund and the Isaak Walton Killam Memorial Scholarship Fund is gratefully acknowledged in addition to the research support from the Alberta Gas Transmission Division of NOVA CORPORATION OF ALBERTA. The use of the laboratory, computing, work-shop and office facilities at the Novacor Research & Technology Center for the duration of the work was greatly appreciated.

Finally, I would like to offer sincere thanks to my wife, Anita, and my parents for their unselfishness, encouragement and steadfast support during this endeavor. And thanks to my Creator, the source of all knowledge.

This dissertation is dedicated to

Anita..

and to my parents.

Table of Contents

Approval Sheet	ii
Abstract	iii
Acknowledgments	iv
Dedication	v
Table of Contents	vi
List of Tables	ix
List of Figures	x
Nomenclature	xiv
1 Introduction	1
1.1 Viscous Drag Reduction with Riblets	1
1.2 Scope of the Study	4
1.3 Dissertation Format	5
2 Background and Literature Review	7
2.1 Turbulent Pipe Flow	7
2.1.1 Smooth Pipes	9
2.1.2 Rough-walled Pipes	12
2.2 Synopsis of Viscous Drag Reduction Techniques	13
2.3 Origin of Riblets	16

2.4	Survey of Available Riblet Data	20
2.4.1	Direct Drag and Friction Factor Measurements	20
2.4.2	Turbulence Structure	22
2.5	Existing Concepts of Riblet Drag Reduction	25
3	Friction Factor Measurements: Moderate Reynolds Number in Air Flow	28
3.1	Apparatus and Measurement Techniques	28
3.1.1	Test Facility	29
3.1.2	Instrumentation and Data Analysis	31
3.2	Experiments with Smooth and Riblet Surfaces	34
3.2.1	Smooth Pipe Benchmark	34
3.2.2	Tests of Three Different Riblet Surfaces	36
3.2.3	Half-lined Pipe Test	42
3.3	Summary of Results	43
4	Friction Factor Measurements: High Reynolds Number in Natural Gas Flow	44
4.1	High Pressure Test Facility	44
4.2	Instrumentation and Data Analysis	46
4.3	Experimental Results	47
5	Consideration of Viscous Effects	51
5.1	Laminar Flow in Pipes with Blade-type Riblets	51
5.1.1	Description of the Geometry	52
5.1.2	Analytical Solution of the Governing Equations	53
5.1.3	Shear Stress and Friction Factor Calculations	55
5.1.4	Implications of Protrusion Heights	57
5.2	Scaling Parameters for Riblet Drag Reduction	58

6	Drag Reduction Mechanism in a Low Reynolds Number Turbulent Flow	62
6.1	Apparatus and Experimental Techniques	62
6.1.1	Test Facility	62
6.1.2	Hot-wire Anemometry Probes	65
6.1.3	Probe Calibration	67
6.1.4	Measurement Procedures and X-wire Signal Analysis	68
6.2	Turbulence Statistics	71
6.2.1	Mean Velocity Profiles and Turbulence Intensities	71
6.2.2	Reynolds Stresses	75
6.2.3	Higher-order Statistics and Triple Correlations	79
6.3	Turbulence Structure	85
6.3.1	Radial Correlations	85
6.3.2	Azimuthal Correlations	91
6.4	Proposed Drag Reduction Mechanism	96
7	Conclusions	103
	References	109

List of Tables

2.1 Detailed investigations of turbulent flow over riblets as reported in the literature	23
3.1 Uncertainty of basic measurement parameters for friction factor analysis	32
6.1 Geometry and experimental flow conditions	65

List of Figures

1.1	Various drag-reducing riblet shapes	2
2.1	Comparison of laminar and turbulent velocity profiles in a pipe for the same mean velocity ($Re_b \approx 4000$)	8
2.2	The universal velocity-distribution for smooth pipes	10
2.3	Friction velocity and viscous wall unit scaling with Reynolds number	11
2.4	Frictional resistance in rough pipes (from Nikuradse 1933)	12
2.5	Summary of drag reduction measurements with riblets in pipe flow	21
2.6	Viscous longitudinal and cross-flow protrusion heights of a ribbed surface	26
3.1	Schematic of open-loop apparatus with interchangeable test pipes	29
3.2	Typical pressure profile along the test pipe axis	35
3.3	Measured friction factor in smooth pipes	35
3.4	Triangular riblet sheet from 3M ($h = s = 120 \mu\text{m}$)	37
3.5	Triangular riblet sheet from 3M ($h = s = 150 \mu\text{m}$)	37
3.6	Scalloped riblet sheet from Hoechst AG ($h = 100 \mu\text{m}$; $s = 200 \mu\text{m}$)	38
3.7	Typical cored pressure tap in a riblet sheet (large 3M triangular profile)	39
3.8	Friction factor measurements in riblet-lined pipes	40
3.9	Drag reduction in riblet-lined pipes compared to smooth pipes	41
3.10	Friction factor measurements in a half-lined riblet pipe	42

4.1	A portion of NOVA's Gas Dynamic Test Facility.....	45
4.2	Schematic of test section within the larger high pressure piping.....	46
4.3	Low aspect ratio triangular riblet sheet from 3M ($h = 4 \mu\text{m}$; $s = 23 \mu\text{m}$) ...	48
4.4	Friction factor measurements in smooth and riblet pipe at high pressure.....	49
4.5	Drag reduction with riblets in high Reynolds number pipe flow	50
5.1	Blade-riblet flow field geometry	53
5.2	Effect of blade ribs on dimensionless shear stress per unit length	56
5.3	Longitudinal protrusion height in laminar pipe flow with blade riblets	58
5.4	Effect of aspect ratio on drag reduction (data from Bruse <i>et al.</i> 1993)	59
5.5	Scaling of non-dimensional riblet height with ratio of longitudinal protrusion height to riblet height ($1-h_{pl}/h$) for various riblet shapes.....	60
5.6	Scaling of riblet drag reduction with $(1-h_{pc}/h) / \Delta h/s$ for various riblet shapes	61
6.1	Open-loop pipe apparatus with adaptable test section	63
6.2	Cross-sections of riblet pipes: (a) blade ribs covering half of pipe periphery; (b) scalloped ribs.....	64
6.3	Hot-wire probes: (a) single wire TSI 1260A-T1.5; (b) DANTEC 55P51 X-wire; (c) TSI 1249A-T1.5 miniature angle X-wire.....	66
6.4	Variation of yaw coefficient k with velocity for X-wire probes	68
6.5	Inferred velocity vector V resulting from X-wire probe measurement in a mean velocity gradient perpendicular to the planes of the support needles (sensors are oriented at 90° to each other)	70
6.6	Mean streamwise velocity above smooth and riblet surfaces normalized with the pipe centerline velocity U_c	72
6.7	Streamwise velocity over smooth and riblet surfaces in local wall units	73
6.8	Turbulence intensities over smooth and blade riblet surfaces	74

6.9	Turbulence intensities over smooth and blade riblet surfaces normalized with the local mean streamwise velocity	75
6.10	Diagonal components of the stress anisotropy tensor b_{ij} over smooth and blade riblet surfaces	76
6.11	Comparison of Reynolds shear stress over smooth and blade riblet surfaces normalized with centerline velocity U_c^2	77
6.12	Reynolds shear stress above smooth and blade riblet surfaces normalized with the local mean streamwise velocity U^2	77
6.13	Skewness and flatness factors of Reynolds shear stress over smooth and blade riblet surfaces: (a) $S(u_x u_r)$; (b) $F(u_x u_r)$	78
6.14	Skewness and flatness factors of streamwise velocity over smooth and blade riblet surfaces: (a) $S(u_x)$; (b) $F(u_x)$	80
6.15	Skewness and flatness factors of radial velocity over smooth, blade riblet and scalloped riblet surfaces: (a) $S(u_r)$; (b) $F(u_r)$	81
6.16	Skewness and flatness factors of azimuthal velocity over smooth and blade riblet surfaces: (a) $S(u_\theta)$; (b) $F(u_\theta)$	83
6.17	Shear stress flux due to radial and streamwise velocity fluctuations over smooth and blade riblet surfaces: (a) $\overline{u_x u_r^2} / \overline{u_x' u_r'^2}$; (b) $\overline{u_x^2 u_r} / \overline{u_x'^2 u_r'}$	84
6.18	Shear stress flux due to azimuthal and streamwise velocity fluctuations over smooth and blade riblet surfaces: (a) $\overline{u_x u_\theta^2} / \overline{u_x' u_\theta'^2}$; (b) $\overline{u_x^2 u_\theta} / \overline{u_x'^2 u_\theta'}$	84
6.19	Two-point radial correlations of streamwise velocity $R_{u_x u_x}(r_1, r_2)$: (a) smooth surface ; (b) blade riblet surface	86
6.20	Two-point radial correlations of radial velocity $R_{u_r u_r}(r_1, r_2)$: (a) smooth surface ; (b) blade riblet surface	88
6.21	Two-point radial correlations of azimuthal velocity $R_{u_\theta u_\theta}(r_1, r_2)$: (a) smooth surface ; (b) blade riblet surface	89

6.22 Two-point radial correlations of Reynolds shear stress $R_{u_x u_r, u_x u_r}(r_1, r_2)$:	
(a) smooth surface ; (b) blade riblet surface	90
6.23 Two-point azimuthal correlations of streamwise velocity $R_{u_x u_x}(r\theta_1, r\theta_2)$:	
(a) smooth surface ; (b) blade riblet surface	92
6.24 Two-point azimuthal correlations of radial velocity $R_{u_r u_r}(r\theta_1, r\theta_2)$:	
(a) smooth surface ; (b) blade riblet surface	93
6.25 Two-point azimuthal correlations of azimuthal velocity $R_{u_\theta u_\theta}(r\theta_1, r\theta_2)$:	
(a) smooth surface ; (b) blade riblet surface	94
6.26 Two-point azimuthal correlations of Reynolds shear stress	
$R_{u_x u_r, u_x u_r}(r\theta_1, r\theta_2)$: (a) smooth surface ; (b) blade riblet surface	95
6.27 Schematic of proposed riblet drag reduction mechanism.....	99
6.28 Experimental test for presence of flow reversals in a blade riblet valley (single wire probe located in riblet groove midway between valley floor and blade peak): (a) bridge voltage signature of controlled flow reversal; (b) bridge voltage signal during normal operation showing absence of flow reversals.....	101

Nomenclature

b_{ij}	Stress anisotropy tensor
D	Pipe diameter
D_{eff}	Effective pipe diameter based on equivalent cross-sectional area
\hat{F}_τ	Non-dimensional shear force
h	Rib height
h_{pc}	Cross-flow protrusion height
h_{pl}	Longitudinal protrusion height
Δh	Difference between longitudinal and cross-flow protrusion heights
k	Yaw coefficient
k_s	Sand grain size
L	Distance between pressure taps
\hat{L}	Unit length
l_w	Viscous wall unit ν/u_τ
\dot{m}	Mass flow rate
M	Number of ribs
P	Static pressure
ΔP	Pressure difference
r	Radial coordinate
R	Radial coordinate
\hat{R}	Dimensionless radial coordinate, R/R_o
R_a	Root-mean-square surface roughness

R_i	Radius from pipe center-line to blade rib tip
R_o	Radius from pipe center-line to bottom of blade rib valley
\hat{R}_i	Non-dimensional pipe radius, R_i/R_o
Re_b	Reynolds number based on pipe diameter and bulk velocity
Re_H	Reynolds number based on channel height and bulk velocity
Re_θ	Reynolds number based on momentum thickness and free-stream velocity
s	Spanwise rib spacing
t	Blade riblet thickness
u	Streamwise fluctuating velocity
u_x	Axial fluctuating velocity
u_r	Radial fluctuating velocity
u_θ	Azimuthal fluctuating velocity
u_τ	Friction or shear velocity
U	Streamwise velocity
\hat{U}	Dimensionless axial velocity, $U/\{(1/\mu)R_o^2(-dP/dx)\}$
U_b	Bulk velocity
U_{eff}	Effective cooling velocity
U_x	Mean axial velocity
v	Normal fluctuating velocity
w	Spanwise (cross-stream) fluctuating velocity
x	Axial coordinate
y	Distance from wall

Greek Symbols

α	Half-angle between base of adjacent ribs
β	Half-angle of rib

γ	Half-angle between two adjacent ribs
δ	Boundary layer thickness
δ_{ij}	Kronecker delta: for $i = j$, $\delta_{ij} = 1$; $i \neq j$, $\delta_{ij} = 0$
ε	Absolute pipe roughness
θ	Angular coordinate
λ	Darcy friction factor
μ	Dynamic viscosity
ν	Kinematic viscosity
ξ_1, ξ_2	Weighting factors
ρ	Fluid density
τ_w	Wall shear stress
τ^*	Non-dimensional time
ϕ	Angle between velocity vector and the normal to the X-wire
Φ	Angle between hot-wire sensor and probe axis
ψ	Angle between inferred velocity vector and probe axis
ω	Ratio γ/α

Superscripts

+	Non-dimensionalized with wall coordinates
/	Root-mean-square value (intensity)
—	Average

Chapter 1

Introduction

1.1 Viscous drag reduction with riblets

The rather intriguing concept that a rough surface consisting of streamwise grooves, or *riblets*, can reduce friction drag in turbulent wall-flows has aroused considerable interest over the past decade. In considering the *total* or *profile drag* of an object moving through a fluid, it was well known that by deliberately disturbing a laminar boundary layer to make it turbulent, the *form* or *pressure drag* component can be reduced. Using roughness to initiate the laminar-to-turbulent transition, the flow separation, which causes an energy dissipating wake behind the body, can be delayed to produce a smaller wake and thus less drag. However, when considering the other component of the total drag, the *skin friction* or *viscous drag*, it was believed that a smooth surface resulted in the least resistance for a turbulent boundary layer or pipe flow. Indeed, the experiments of Nikuradse (1932, 1933) had demonstrated that sand of a definite grain size glued to the inside wall of circular pipes resulted in a frictional resistance larger than that of a smooth surface. For flow through a straight smooth pipe, the entire drag is due to skin friction which manifests itself as a loss of pressure in the direction of flow. In light of Nikuradse's experiments, it seemed almost inconceivable that this loss of pressure could be *reduced* by roughening the pipe surface or increasing the surface area through extended surfaces. Nevertheless, the results of a resurgence in turbulent boundary layer structure research changed this notion.

Although the idea that longitudinal fins might modify the near-wall turbulence structure had been proposed much earlier, it was not until Walsh & Weinstein (1978) reported reductions with direct drag measurements that the concept was demonstrated. Since then, a significant number of independent measurements have confirmed that flow over properly sized riblets undoubtedly exhibits up to 10% less drag compared to the same flow over a smooth surface. Several different geometrical riblet shapes for which various levels of drag reduction have been measured are shown in figure 1.1.

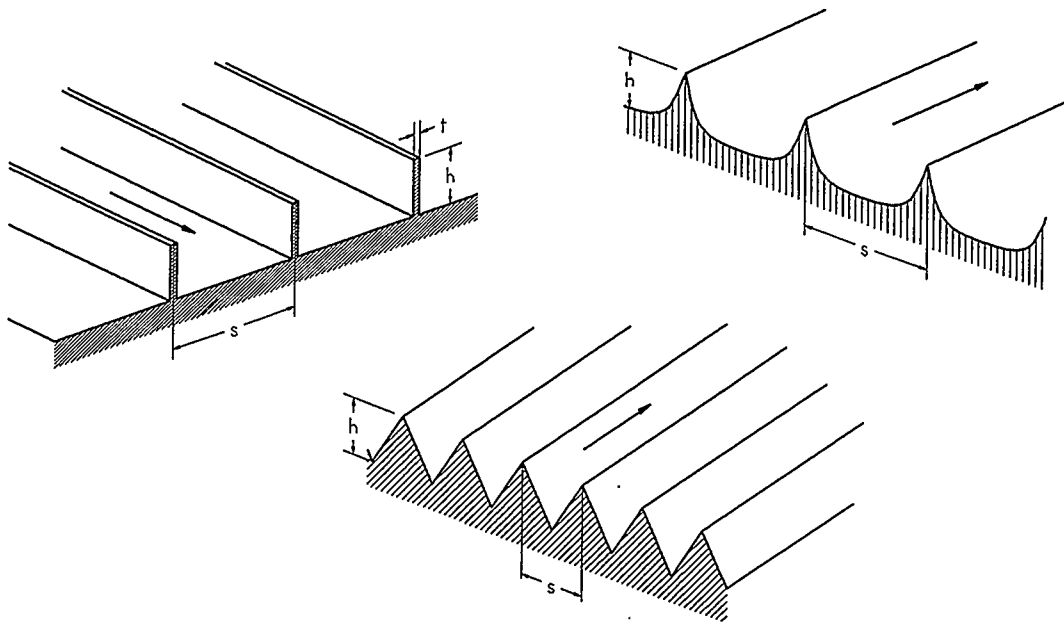


FIGURE 1.1. Various drag-reducing riblet shapes.

A unique feature of these surfaces is that they all reduce skin friction despite the substantially increased wetted surface area, but only when the non-dimensional height h^+ is in the range 1-30 (the parameter h^+ can also be thought of as a local Reynolds number based on the rib height h and the friction velocity u_τ ; i.e. $h^+ = h u_\tau / \nu$). Furthermore, the aspect ratio h/s of the ribs (where s is the spanwise rib spacing), the sharpness of the rib peaks, and the riblet profile are all important parameters which affect the level of drag reduction and the range in which it occurs.

In an attempt to gain an understanding of the underlying physical mechanisms responsible for the observed drag reduction, several investigations of the turbulent structure over such riblets had already been conducted by the time the present study was initiated. However, a clear picture of the differences between turbulence structure over smooth and riblet surfaces had not yet emerged. In the mean time, the salient features of turbulence statistics and flow structures over riblets have been ascertained through numerous further studies utilizing hot-wire anemometry, laser-Doppler anemometry (LDA), flow visualization techniques and, recently, direct numerical simulations (DNS). Based on these new findings and the analysis of longitudinal and transverse viscous flow over riblets, certain plausible explanations of the basic drag reduction mechanism have been proposed.

The proposed mechanisms have to some degree captured the symptoms or effects of riblets and identified that transverse velocity fluctuations and vortex interactions likely play a key role in the drag-reducing mechanism. However, in the attempt to associate riblet drag reduction with a specific dynamical process, strong experimental evidence for the conjectures has typically been lacking. Although significant progress has been made during the past decade towards the establishment of cause-and-effect relationships for the observed flow behavior in the near-wall region of turbulent flows over *smooth surfaces*, this new information has not been fully exploited in the effort to determine the riblet drag reduction mechanism. Furthermore, proper scaling parameters leading to a universal riblet drag reduction curve have not been found, despite the fact that some explanations for the effects of aspect ratio, shape and rib sharpness have been offered. Evidently, additional insight into the near-wall dynamical processes which are *directly* responsible for riblet drag reduction is needed.

1.2 Scope of the Study

The intent of the present study is to provide a detailed account of drag reduction with riblets in turbulent pipe flow. Emphasis is placed on conducting relatively simple but precise experiments to compare the flow structure over smooth and riblet surfaces. Then, in light of the experimental evidence, theoretical and analytical concepts are applied in an attempt to elucidate the drag reduction mechanism.

Specifically, the effectiveness of riblet drag reduction and scaling of riblet dimensions over a wide range of Reynolds numbers is investigated. The application of riblets towards very high Reynolds number flows in high pressure gas transmission systems is also considered experimentally, which is of particular interest for industry.

The present study also attempts to provide much needed information about the turbulence structure in pipe flow with and without optimum drag-reducing riblets. Considering the vast amount of interest which riblets have generated, there is a definite lack of turbulence structure information for pipe flows. To date, only four studies of turbulent flow in ribbed pipes have been reported (Nitschke 1983; Liu *et al.* 1989/90; Rohr *et al.* 1989; Nakao 1991) and of these, only Nitschke (1983) has measured any turbulence quantities. Only the streamwise velocity component was measured in ribbed pipes with very little drag reduction, due to the riblet geometry. In the present study, measurements of azimuthal and radial correlations for all three velocity components and turbulent shear stress in the near-wall region are made possible by the increased spatial resolution of a judiciously chosen low Reynolds number turbulent flow. As such, important information regarding length scales is provided—length scales which have not been measured even for smooth-plate boundary layers. Ultimately, in particular for gas flows, information contributing to the understanding of the riblet drag-reducing mechanism will hopefully lead to the development of better ways of reducing drag.

1.3 Dissertation Format

The contents of each major section in this dissertation are briefly summarized.

BACKGROUND AND LITERATURE REVIEW: Some basic turbulent pipe flow concepts are covered, followed by a synopsis of several viscous drag reduction methods. After tracing the genesis of riblets, findings from direct drag and turbulence structure measurements which pertain specifically to the issue of drag reducing mechanisms are deliberated. Finally, some existing ideas of how rib structures might reduce drag are considered.

FRICITION FACTOR MEASUREMENTS: MODERATE REYNOLDS NUMBER IN AIR FLOW: Experiments conducted over a wide range of Reynolds number ($Re_b = 1 \times 10^4 - 2 \times 10^5$) with several different riblet surfaces in a split-pipe are described. Particular attention is drawn to the accuracy and repeatability of the experimental results and the unique case of riblets covering only half of the pipe (longitudinally).

FRICITION FACTOR MEASUREMENTS: HIGH REYNOLDS NUMBER IN NATURAL GAS FLOW: The results of a novel experiment with riblets in a high pressure (6000 kPa) natural gas pipeline at relatively high Reynolds number ($Re_b = 7.5 \times 10^5 - 6.5 \times 10^6$) are presented.

CONSIDERATION OF VISCOUS EFFECTS: The hypothesis that turbulent drag reduction with riblets is due only to greatly reduced viscous shear stress in the riblet valleys is considered by extending an existing analytical solution for laminar pipe flow with blade-type riblets. Though it is shown that only an increase in wall shear stress can be expected for laminar flow, the examination of viscous effects does provide scaling parameters leading to an almost universal drag reducing curve for riblets.

DRAG REDUCTION MECHANISM IN A LOW REYNOLDS NUMBER TURBULENT FLOW: An experimental study comparing turbulence structure over a drag-reducing blade riblet

surface and smooth pipe wall at $Re_b \approx 5500$ is presented. Using single and X-wire anemometry techniques, turbulence statistics as well as detailed radial and azimuthal space-correlations of all three velocity components and turbulent shear stress in the near-wall region were obtained. The results quantitatively confirm that riblets primarily interfere with the viscous-inviscid interaction process in the near-wall region.

In the final chapter, the most important findings of the present study are summarized and conclusions concerning the riblet drag reduction mechanism are presented.

Chapter 2

Background and Literature Review

The purpose of this chapter is essentially threefold: to present the salient features of turbulent flow in smooth and rough pipes; to briefly introduce various viscous drag reduction methods and their associated mechanisms; and to review the existing experimental data on riblet drag reduction. A basic understanding of the dynamic physical processes in the near-wall region of a turbulent pipe flow, along with an understanding of other types of viscous drag reduction, provides a sound basis for examining the mechanism of riblet drag reduction.

2.1 Turbulent Pipe Flow

A few fundamental concepts provide a useful starting point in the discussion of turbulent pipe flow. Figure 2.1 compares laminar and turbulent mean streamwise velocity profiles for the same flow rate. The much flatter turbulent velocity profile with the higher velocity gradient and shear stress at the wall, results from random fluctuating vorticity which causes mixing or fluctuations of velocity. At the wall, these velocity fluctuations, as well as the mean velocity, must vanish due to the no-slip boundary condition there. Thus, in the near-wall region, viscosity plays an important role in the dynamics of the fluid motion even in a turbulent flow.

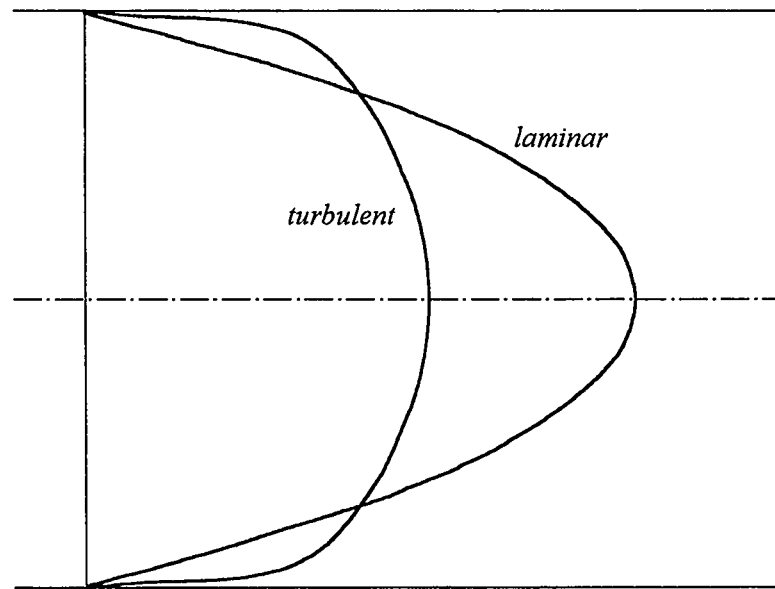


FIGURE 2.1. Comparison of laminar and turbulent velocity profiles in a pipe for the same mean velocity ($Re_b \approx 4000$).

A turbulence-energy balance across the pipe indicates that the *wall* or *inner region* is in 'local equilibrium'—indicating that a local balance exists between the processes supplying energy to the turbulence and those dissipating or removing it. The *core* or *outer region*, on the other hand, is characterized by an excess dissipation which requires a constant source of energy to sustain the turbulent velocity fluctuations. This source is supplied by the mean-flow kinetic energy, which is transferred to the surface shear layer by sweep-like events where it is converted into turbulent kinetic energy and also into heat through viscous dissipation. The turbulent kinetic energy is in turn diffused outward from the wall region towards the core of the pipe. Clearly, a mechanism of turbulence regeneration is necessary to introduce vorticity from the wall layer into the core region. Smith *et al.* (1991) have proposed a model of such a mechanism for which the hairpin vortex is the key element. It has been demonstrated that hairpin vortices not only form near the wall but are also able to generate new hairpin vortices, thus providing a self-sustained turbulence production mechanism.

2.1.1 Smooth pipes

The region adjacent to the wall is the most important part of a pipe flow and, because of the local equilibrium, its structure is substantially independent of the core flow. When the wall is perfectly smooth, there exists a thin layer at the wall, known as the *viscous sublayer*, where the flow is predominantly viscous. This viscous sublayer has sometimes been referred to as the *laminar sublayer*, however the latter term does not accurately reflect the large velocity fluctuations which do occur in this region. The flow in the wall region, including the viscous sublayer, is characterized by a velocity scale termed the friction or shear velocity u_τ , which is expressed in terms of the wall shear stress τ_w :

$$u_\tau = \sqrt{\frac{\tau_w}{\rho}} \quad (2.1)$$

The friction velocity and the kinematic viscosity together form a characteristic length scale, or 'viscous wall unit' l_w , which can be defined as:

$$l_w = \frac{\nu}{u_\tau} \quad (2.2)$$

Plotting the local mean velocity and distance from the pipe wall in wall coordinates, that is, normalizing the mean velocity U_x with the friction velocity and the distance from the pipe wall y with the viscous wall unit, results in the universal velocity-distribution for smooth pipes shown in figure 2.2. This relation of U^+ and y^+ is valid for turbulent pipe flows with $Re_b > 1 \times 10^4$. An extreme diversity of processes and structures occur in the wall region which consists of the viscous sublayer ($y^+ < 5$) and the buffer region ($5 < y^+ < 50$). The core region ($y^+ > 50$) is also known as the *inertial sublayer* and is characterized by a logarithmic profile.

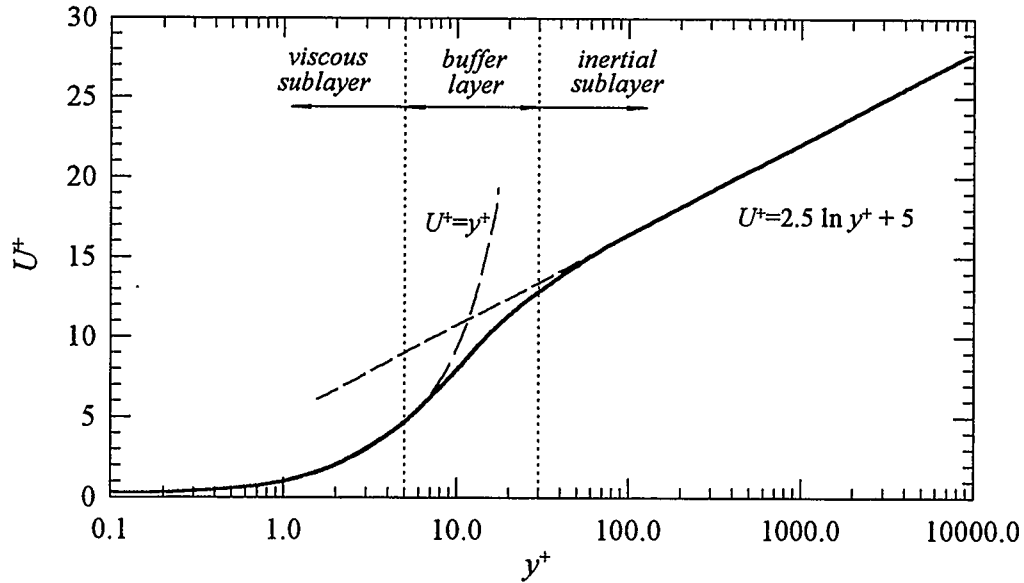


FIGURE 2.2. The universal velocity-distribution for smooth pipes.

For smooth pipes, it is very useful to develop expressions for the non-dimensional friction velocity and viscous wall unit which are functions of only the Reynolds number. From the balance of pressure and shear forces on a fluid element in steady, fully developed turbulent pipe flow we have

$$\tau_w = \frac{R}{2} \frac{dP}{dx} \quad (2.3)$$

and the empirically obtained expression for the pressure gradient is

$$\frac{dP}{dx} = \frac{\lambda}{D} \frac{\rho}{2} U_b^2 \quad (2.4)$$

Eliminating the pressure gradient term from (2.3) and (2.4) and substituting for τ_w in (2.1) results in a simple expression for the friction velocity normalized with the bulk velocity

$$\frac{u_\tau}{U_b} = \sqrt{\frac{\lambda}{8}} \quad (2.5)$$

Then, by substituting (2.5) into (2.2) and re-arranging, the following expression for the ratio of viscous wall unit to pipe diameter is obtained

$$\frac{l_w}{D} = \frac{\sqrt{8/\lambda}}{Re_b} \quad (2.6)$$

For smooth pipes the friction factor λ is a function of only the Reynolds number Re_b based on the bulk velocity and pipe diameter. Thus plotting equations (2.5) and (2.6) with respect to the Reynolds number, it is evident from figure 2.3 that the friction velocity remains essentially a constant fraction of the bulk velocity. However, with respect to the pipe diameter, the viscous wall unit experiences a logarithmic decrease with increasing Reynolds number (see also figure 2.3). This result clearly illustrates that, for large Reynolds numbers, the important wall layer events occur within an extremely narrow region. Thus, the difficulties encountered in obtaining near-wall turbulence measurements for high-Reynolds number flows can be appreciated.

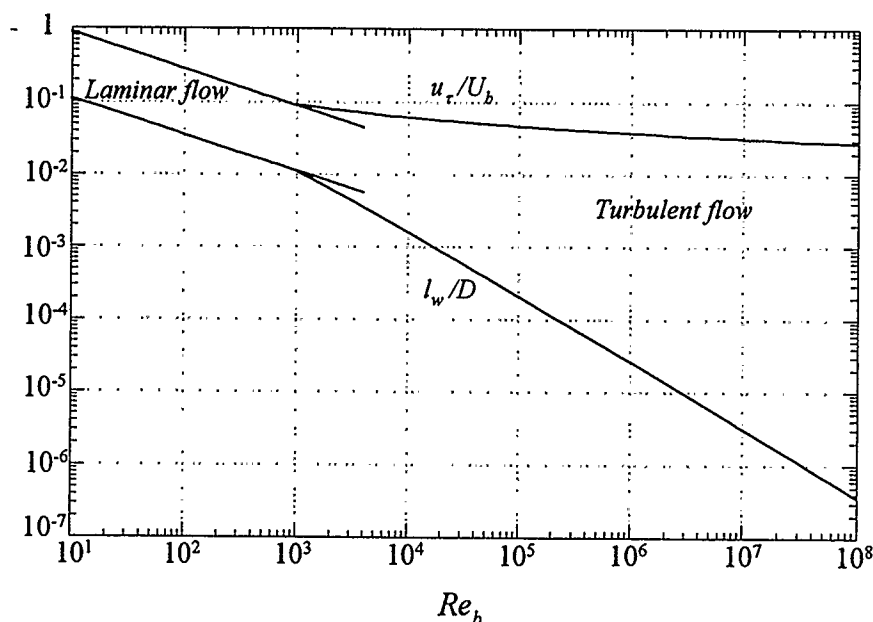


FIGURE 2.3. Friction velocity and viscous wall unit scaling with Reynolds number.

2.1.2 Rough-walled pipes

Nikuradse's (1933) experiments with sand of a definite grain size glued to the inside wall of circular pipes, showed that if the roughness is small enough to be completely contained within the viscous sublayer, the frictional resistance is identical to that of a perfectly smooth pipe. Such rough pipes are considered to be *hydraulically smooth*, since the friction factor depends only on the Reynolds number. However, if the roughness is large enough to protrude partly through the viscous sublayer, an additional form drag is experienced by the protrusions. This results in frictional resistance larger than that of the smooth surface and the friction factor becomes a function of both Reynolds number and the relative roughness k_s/R of the protrusions. Finally, when the protrusions become so large that they rise completely out of the viscous sublayer, the majority of the frictional resistance is due to form drag and the friction factor becomes a function of the relative roughness only. In this completely rough regime the viscous sublayer really has no importance since it is essentially destroyed by the roughness. The measurements of Nikuradse (1933), shown in figure 2.4, indicate that wall roughness will always result in frictional losses equal to or greater than those of smooth pipes.

pipes.

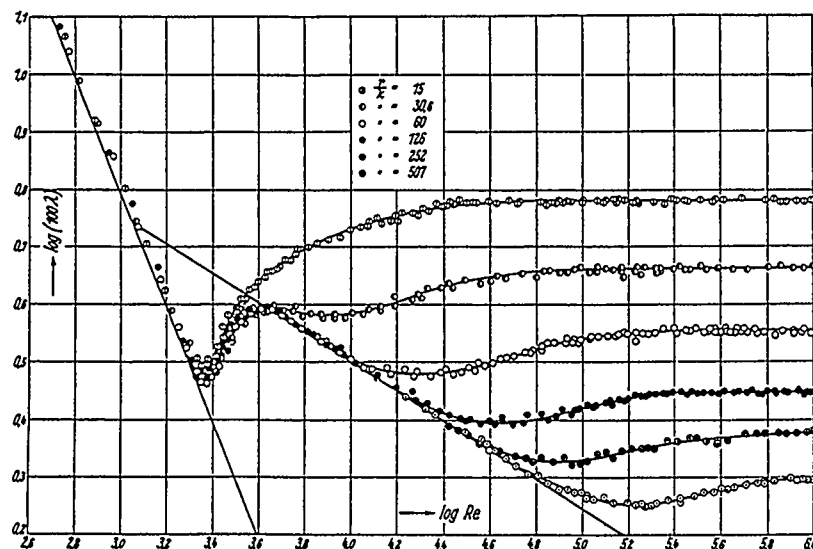


FIGURE 2.4. Frictional resistance in rough pipes (from Nikuradse 1933).

2.2 Synopsis of Viscous Drag Reduction Techniques

Before considering several viscous drag reduction techniques, which have been developed over the past 45 years, it is perhaps worthwhile to briefly mention some obvious fundamental limits of viscous drag reduction. It is well known that viscous drag cannot be eliminated by providing a very smooth or slippery surface, such as Teflon, since the no-slip wall boundary condition remains. If, however, a slip condition at the wall could be obtained, the ultimate viscous drag reduction would result—no viscous drag! This in fact does occur for very specific conditions in fluids such as liquid helium, which exhibits a complete absence of viscosity, or *superfluidity*, at extreme cryogenic temperatures (< 4 K), but this is extraordinary fluid behavior. If the bulk viscosity of the fluid cannot be changed, it is generally accepted that for any given flow condition, the drag due to laminar flow over a smooth surface would be the minimum achievable viscous drag. At present, there is no evidence which would indicate that viscous drag in laminar flow can be reduced.

An understanding of other types of viscous drag reduction can certainly aid in discerning the drag mechanism due to riblets. Therefore, a synopsis of several viscous drag reduction techniques and the present perception of their associated mechanisms follows. The discussion is limited to those techniques which are reported in literature and have foreseeable practical applications, with the exception of LEBUs (Large Eddy Break-Up devices) which are not as effective as originally anticipated.

Polymers

Since Toms (1949) reported that low concentration polymer solutions (≈ 100 wppm) can reduce the skin friction drag by up to 70 percent in pipe flows with liquids, many experiments have been performed which confirmed the phenomenon. Furthermore,

this drag reduction technique has been implemented since 1979 in the Trans Alaskan Pipeline with great success, eliminating the need to build two of the originally planned twelve pump stations (Motier & Carrier 1989).

Virk (1975) provides an excellent review of the research on drag reduction by dilute solutions of linear, random-coiling macromolecules (molecular weight $\approx 10^6$) in turbulent pipe flow and makes several interesting observations. In the buffer region of polymer drag-reducing solutions, the turbulence structure differs significantly from that of the Newtonian solvent alone: the axial intensity u' is higher while radial intensity, turbulent shear stress, and the u - v correlation coefficient are all lower. This indicates that the axial and radial flow fields are decoupled (as seen by a reduction in Reynolds shear stress and the reduced u - v correlation coefficient) which reduces the radial transport of axial momentum and turbulent kinetic energy. A re-adjustment (i.e. higher axial turbulence intensity) of the inner flow region occurs in order to maintain the cross-sectional turbulent energy balance, because the core region has essentially the same turbulence structure as the Newtonian solvent. Additionally, it seems that the polymer molecules interfere with the bursting process since the duration of a turbulent burst is of the same order as the relaxation time of the macromolecules. It appears that macromolecular extension, due to fluid shear, is the primary mechanism of drag reduction as it is the extended molecules which inhibit radial momentum exchange (Virk & Wagger 1989).

Fibers

McComb & Chan (1985) found that small asbestos fibers (diameter = 0.05 μm ; length = 1.4 mm), suspended in water, also resulted in drag reductions of up to 70 percent. From LDA measurements they found that the axial turbulent intensity increased, similar to polymer drag-reducing flows, suggesting a similar mechanism of

axial and radial flow field decoupling. Fiber drag reduction also lends support to the theory that it is the extended macromolecules in polymer flows which are primarily responsible for the observed drag reduction.

Microbubble injection

This technique involves the injection of gas into a liquid boundary layer to form a two-phase bubbly mixture, which results in drag reduction levels similar to that obtained with polymers. Once the microbubbles find their way into the near-wall region of the boundary layer, they seem to destroy the energy-producing velocity fluctuations in the buffer region. Merkle & Deutsch (1990) have provided an excellent review article on this subject.

Compliant walls

The use of a compliant wall to delay the transition from laminar to turbulent flow in liquids has been successful and involves cancellation of the discrete frequency Tollmien-Schlichting waves (Carpenter 1990). However, it has not been conclusively demonstrated that compliant wall motion could lead to drag reduction in a fully turbulent boundary layer, though work is presently underway at DLR in Berlin to model the compliant characteristics of shark-scales in an oil channel (Bruse *et al.* 1993). For air-flows, it is essentially impossible to construct a compliant wall with current technology, owing to the extremely small modulus of elasticity and damping required for such flows.

LEBUs or OLDs

Large-eddy breakup (LEBU) or outer-layer devices (OLD) consist of small airfoils placed in the wake region of the boundary layer (usually $0.5-0.8\delta$ from the wall). The local skin friction immediately downstream of the device is indeed reduced—through

interaction of the device's wake with the near-wall region momentum exchange normal to the wall—but there is no evidence of a *net* drag reduction due to the drag penalty of the device itself. Measurements based on velocity profiles seemed to indicate that net drag reductions would be attainable but direct device and friction drag measurements by Lynn *et al.* (1989) and others have shown that a net drag reduction is not expected for high Reynolds number flows. Additionally, Pollard *et al.* (1989) have demonstrated that such devices show no net drag reduction in fully developed turbulent pipe flow. It may, however, be possible to achieve some net drag reduction in low Reynolds number flows with much smaller devices placed closer to the wall (Nagib *et al.* 1989).

Riblets

Since it was discovered that finely grooved surfaces can provide less skin friction resistance in turbulent flow than smooth surfaces, considerable interest in riblets has been generated, including the initiation of the present study. In the three sections which follow, the genesis of the concept of riblets is traced, findings pertaining specifically to the issue of drag-reducing mechanisms are gleaned from the literature and some existing ideas of how rib structures might reduce drag are discussed.

2.3 Origin of Riblets

The notion that longitudinally grooved surfaces may reduce turbulent skin friction developed from three distinct concepts: i) modification of the near-wall structure may reduce skin friction; ii) friction is reduced in the corner regions of turbulent flows; and iii) fast-swimming sharks have scales whose structure may account for the incredible speeds attainable by some species. Each of these concepts contributed to the maturing

of riblets as a drag reduction technique—a process which extended over a period of more than ten years.

Modification of near-wall structure

Compared with isotropic turbulence, the near-wall region of turbulent wall-flows appears not to be purely stochastic. This was already noticed by Prandtl (1925) who based his mixing-length theory on observations of fluid motion, in particular the "Flüssigkeitsballen" (fluid balls or eddies) near the wall. Perhaps the first idea that such coherent turbulent structures in the near wall region might be modified to reduce skin friction was reported by Kramer (1939). In a 1937 German patent application, Kramer described a concept involving suspended streamwise wires which would shield the wall region from the outer turbulent fluctuations, however no data were reported. This basic idea was not pursued until somewhat later when a similar concept emerged out of a renaissance of boundary layer structure research, which began with Theodorsen's (1952) observation of horseshoe-like vortical structures in a turbulent boundary layer. Subsequent flow visualization studies (Kline & Runstadler 1959; Runstadler *et al.* 1963; Kline *et al.* 1967) indicated that the near-wall region of the turbulent boundary layer consisted of low- and high-speed regions of fluid which extended for up to 1000 wall units in the streamwise direction and had a mean spanwise spacing of about 100 wall units. The low-speed regions, or streaks, were observed to grow in the streamwise direction, oscillate and then lift off the surface, resulting in a substantial generation of Reynolds shear stress. The distance from the wall at which these eruptions occurred coincided approximately with the region where Reynolds shear stress production was a maximum. An exploratory study to constrain the low-speed streaks was carried out by Liu *et al.* (1966) using small longitudinal fins ranging from 45-110 wall units in height with spacing of 190-370 wall units. The frequency of low-speed streak eruptions appeared to be reduced, but perhaps not enough to give

significant overall drag reduction. Although the fins were too large to be drag reducing, the discovery that the low-speed streak behavior could be modified was one of the important findings which led to further experiments with smaller rib sizes which in fact do reduce the skin friction.

Reduced friction in corner flows

In the context of drag reduction in gas transmission pipelines, Bath (1968) performed a theoretical analysis of flow at the intersection of two perpendicular planes which utilized velocity profile data from turbulent flow in triangular and rectangular ducts (Nikuradse 1926; Nikuradse 1930; Leutheusser 1963). He determined that small streamwise fins of approximately 20 to 40 wall units in height, with an aspect ratio h/s of one to six, might be used to achieve significant drag reduction. It is rather remarkable that an attempt to exploit the low levels of skin friction in corner flows resulted in a suggestion of fins of almost proper drag-reducing dimensions. This suggestion was pursued in an experimental study by Kennedy *et al.* (1973), who claimed that ribs of the dimensionless height suggested by Bath (1968) were tested in a boundary layer flow. However, their drag balance measurements only showed skin friction *increases* when compared to a smooth surface. A closer inspection of their work shows that the height of the fins they tested were actually three to six times that of the dimensionless fin height suggested by Bath (1968). Thus, they did not measure any net drag reduction since the fins were of height 60 to 140 wall units—similar in size to those of the study by Liu *et al.* (1966)—and not around 20 wall units as suggested by Bath (1968). Unfortunately, Kennedy *et al.* (1973) omitted a gravitational conversion constant when calculating the actual fin dimension; the same error made by Bath (1968) in an illustrative design calculation. This oversight delayed progress in riblet drag reduction and it was not until a study at NASA Langley by

Walsh & Weinstein (1978) that fins of approximately the size prescribed by Bath (1968) were tested in a flat plate boundary layer flow.

Biological observations of shark skin

Research in Germany progressed along a somewhat different vein as scientists studying the biology of sharks discovered peculiarly shaped scales on the skin of fast swimming specimens. The suggestion followed that the rib-like scale shape may reduce skin friction drag and estimates of the non-dimensional height and spacing of these structures were provided. Based on this information, an experimental study of pipe flow with ribs was undertaken at the Max-Planck-Institut by Nitschke (1983). Only small amounts of drag reduction (3 %) were found with fairly large scatter in the measurements. Due to manufacturing limitations, the riblet profiles consisted of ribs with rounded peaks which accounted for the low levels of measured drag reduction. Later, Bechert (1987) measured drag reductions of about six percent in a flat-plate boundary layer flow with three dimensional riblets which were geometrically similar to structures found on shark scales.

Summarizing, the notion that very small grooves or riblets may reduce skin friction developed from three different concepts which led to a common conclusion: the riblets should have dimensions smaller than the low-speed streak spacing in the near-wall region of the boundary layer. Once direct drag measurements confirmed that riblets reduce viscous drag, various geometrical shapes were tested to determine an optimum riblet geometry and numerous investigations of the turbulence structure over riblets were conducted. In the next section, the important parameters governing riblet drag reduction are identified and the influence of riblets on turbulence structure is examined.

2.4 Survey of Available Riblet Data

A comprehensive review of riblet research has been provided by Walsh (1990) in which all available riblet data was evaluated. No attempt to summarize the material presented in that extensive review will be made here. Rather, in what follows, particular findings pertaining specifically to the issue of drag reducing mechanisms will be deliberated.

2.4.1 *Direct drag and friction factor measurements*

Measurements obtained with drag-balances in flat-plate and channel flows and pressure drop measurements in pipe flows have determined that riblets reduce drag in the turbulent regime when the non-dimensional rib height h^+ is in the range 1-30. This scaling has been confirmed for various geometrical shapes over a wide range of Reynolds numbers. Furthermore, the aspect ratio h/s of the ribs, the sharpness of the rib peaks, and the riblet profile are all important parameters which affect the level of drag reduction and the range in which it occurs. In particular, ribs with sharp peaks result in higher levels of drag reduction than those with rounded peaks and triangular shaped riblets, with an aspect ratio close to unity, provide drag reduction over a wider range of h^+ than blade riblets of the same height and spacing. If the ribs are imbedded deep within the viscous sublayer ($h^+ < 1$) neither an increase nor decrease in drag occurs, while for riblet heights greater than 30 wall units (or considerably less for low aspect ratios and blade or scalloped riblets) a drag *increase* is always observed. The presence of an optimal riblet height within these two extremes is perceived to be a significant factor in the determination of the drag-reduction mechanism. So far, the maximum drag reduction obtained is about 10 % using very thin blade-type riblets; the reader is referred to a paper by Bruse *et al.* (1993) for an experimental study of riblet optimization and other novel drag-reducing surfaces.

All drag reduction measurements with riblets in pipe flow are summarized in figure 2.5. Surprisingly, ribs of identical shape but different size result in dissimilar drag reduction curves. This may be due to the ambiguity in defining the diameter of the ribbed pipe, which occurs to the fifth power in the friction factor expression. The pipes tested by Nitschke (1983) had relatively large rounded ribs ($h/D = 0.012$) resulting in a $\pm 3\%$ variation in friction factor depending on the definition of pipe diameter. Liu *et al.* (1990) used considerably smaller riblets ($h/D = 0.00225$ - 0.0045) but the pressure tap holes within the ribbed pipe were altered until a linear pressure gradient was measured. Using a small split pipe with several accessible pressure taps, Rohr *et al.* (1989) compared the results from a linear pressure gradient in both smooth and ribbed pipes, however the relatively large ribs ($h/D = 0.006$ - 0.012) again resulted in ambiguity of the effective pipe diameter. Lastly, Nakao (1991) tested fairly large ribs ($h/D = 0.008$ - 0.017) without considering the effects of effective pipe diameter and did not locate any pressure taps within the riblet test pipe. The uncertainty associated with each of these measurements was the impetus for careful measurements of friction factor in air flow with $h/D < 0.0016$ which were undertaken in the present study.

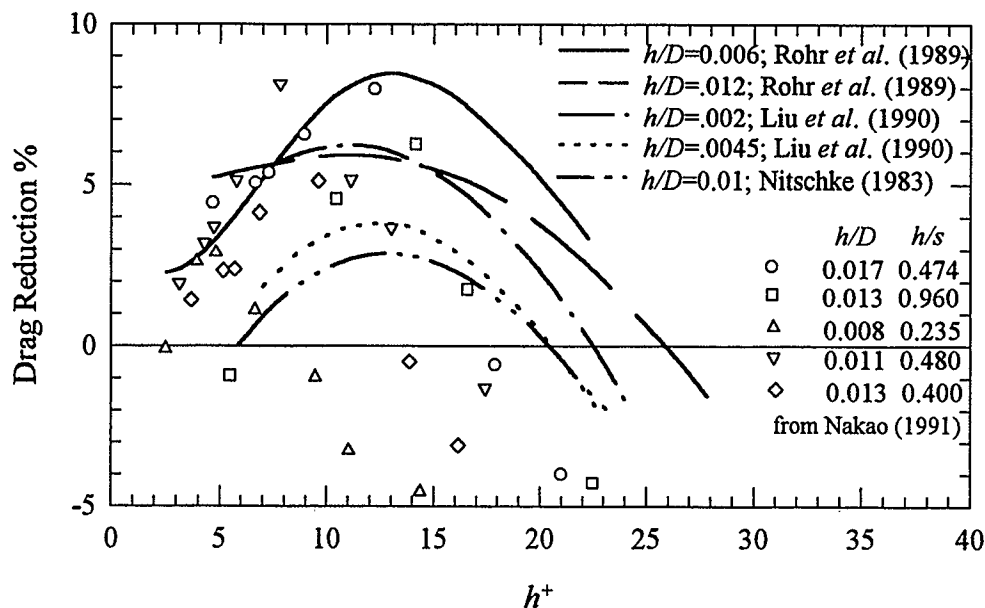


FIGURE 2.5. Summary of drag reduction measurements with riblets in pipe flow.

2.4.2 Turbulence structure

In an attempt to gain an understanding of the underlying physical mechanisms responsible for riblet drag reduction, numerous studies of the turbulence structure over riblets have been conducted. Flow parameters and other pertinent details of these investigations are summarized in table 2.1. Evidently, various flow visualization and velocity measurement techniques have been utilized to determine turbulence statistics and flow structures over riblets, primarily in flat-plate boundary layer flows. Various findings from these studies will be emphasized here. Due to the lack of detailed statistics for pipe flow, observations from flat-plate and channel flow investigations will be considered since the physical processes in the near-wall region of all three types of flow are expected to be similar.

When plotted in wall coordinates, the mean streamwise velocity profile over a riblet surface has essentially the same shape as over a smooth wall, although the profile is shifted upward. The magnitude of this shift depends on whether the rib valley, peak or some intermediate position is chosen as the origin. Nevertheless, drag-reducing ribs appear to thicken the viscous sublayer displacing the velocity profile upwards.

Turbulence statistics measured over riblet surfaces have been found to differ from those over smooth surfaces. When scaled with outer variables, such as the bulk, center-line or free-stream velocity, the maximum streamwise turbulence intensity is reduced by as much as 10%, depending on the level of drag reduction. Recent findings indicate that the transverse intensity, which is believed to play a key role in the drag-reducing mechanism, and the normal intensity are likewise reduced (Suzuki & Kasagi 1993; Chu & Karniadakis 1993). Vukoslavcevic *et al.* (1987) found an increase in both the skewness factor $\overline{u^3} / u'^3$ and flatness factor $\overline{u^4} / u'^4$ of the streamwise velocity fluctuations within the grooves of the ribs, indicating that sweeps, or penetrations of fluid from higher up in the flow, occur less frequently over the groove valley.

Experimental studies												
Source	Type of Flow	Re_θ, Re_b or Re_H	h^+	Fluid	Flow visualization	U	u'	v'	w'	uv	<i>other</i>	Measurement technique
1. Walsh (1982)	flat plate	867 - 3900	5-50	air	—	✓	✓	✓	-	✓	—	hot-wire
2. Nitschke (1983)	pipe	8000 - 45000	4-50	air	—	✓	✓	-	-	-	—	hot-wire
3. Hooshmand <i>et al.</i> (1983)	flat plate	3660	12	air	smoke wire	✓	✓	-	-	-	—	hot-wire
4. Gallagher & Thomas (1984)	flat plate	750 - 1850	15	water	hydrogen bubble/ dye injection	✓	-	-	-	-	<i>u' correlations</i>	hot-film
5. Bacher & Smith (1985)	flat plate	900 - 1300	15	water	hydrogen bubble/ dye injection	✓	✓	-	-	-	<i>skewness/flatness</i>	hot-film
6. Hooshmand (1985)	flat plate	3600	11	air	smoke wire	✓	✓	✓	✓	✓	<i>vorticity, etc.</i>	hot-wire
7. Coustols <i>et al.</i> (1987)	flat plate	2500	7-23	air	—	✓	✓	✓	✓	✓	—	hot-wire
8. Djenidi <i>et al.</i> (1987)	flat plate	630	15	water	dye injection	✓	✓	✓	-	-	—	LDA
9. Vukoslavcevic <i>et al.</i> (1987)	flat plate	1000	17	air	—	✓	✓	-	-	-	<i>skewness/flatness</i>	hot-wire
10. Pulles (1988), Pulles <i>et al.</i> (1989)	flat plate	650 - 1300	8-14	air	smoke wire	✓	✓	✓	-	✓	—	hot-wire
	flat plate	257 - 700	6-16	water	hydrogen bubble	✓	✓	✓	-	✓	—	LDA
11. Reidy & Anderson (1988)	flat plate	5000	13	water	—	✓	✓	-	-	-	—	LDA
12. Choi (1989)	flat plate	4600	13 & 26	air	smoke wire	✓	✓	✓	-	-	—	hot-wire
13. Benhalilou <i>et al.</i> (1991)	flat plate	300	15	water	—	✓	✓	✓	✓	-	—	LDA
14. Bruse <i>et al.</i> (1993)	channel	5000-33000	0-30	oil	—	-	-	-	-	-	—	direct drag
15. Park & Wallace (1993)	flat plate	1200	14	air	—	✓	✓	✓	✓	✓	—	hot-wire
16. Suzuki & Kasagi (1993)	channel	6000&14000	9&20	water	Particle Tracking Velocimetry	✓	✓	✓	✓	✓	—	3D-PTV
Direct Numerical Simulations												
Source	Type of Flow	Re_H	h^+			U	u'	v'	w'	uv		
17. Chu & Karniadakis (1991,1993)	channel	3500	18			✓	✓	✓	✓	✓		
18. Choi <i>et al.</i> (1992)	channel											

TABLE 2.1. Detailed investigations of turbulent flow over riblets as reported in the literature.

The bursting process, which is the ejection of a low-speed streak from the near-wall region into the outer region of the boundary layer, plays a dominant role in the momentum exchange normal to the wall and in the generation of turbulent shear stress. Thus, several attempts have been made to measure the burst frequency utilizing VITA (Variable-Interval Time Average) techniques. The results are inconclusive. For example, Hooshmand *et al.* (1983) and Pulles (1988) found that burst frequency increased, Gallagher & Thomas (1984) and Savill (1987) found it was reduced, while Walsh (1982) and Bacher & Smith (1985) found no change. Gallagher & Thomas (1984) have pointed out that VITA burst detection techniques depend on digitization rate, integration time, record length, probe size and location, and threshold levels: these factors likely account for the disparity in the measurements. Spanwise correlations of the streamwise velocity have also produced conflicting results (Gallagher & Thomas 1984; Pulles 1988), although it is commonly believed that correlations are better indicators of the turbulence structure than conditional averaged techniques because threshold levels are not involved. More correlation data are needed to determine the influence of riblets on turbulence structure.

Lastly, the analysis of basic flow patterns using flow visualizations showed that the lateral movement and spreading of low-speed streaks is dampened (Bacher & Smith 1985; Djenidi *et al.* 1987) and the flow in the valleys of the riblet grooves is extremely slow-moving. The outer flow structures remain essentially unchanged (Hooshmand 1985; Pulles 1988). All of these observations confirm that riblets indeed modify the turbulence structure near the wall and reduce skin friction; however, they fail to identify the specific dynamical processes which are being altered or affected.

2.5 Existing Concepts of Riblet Drag Reduction

From the more detailed measurements and comparisons of turbulence structure over riblets and smooth surfaces, a few physical explanations for riblet drag reduction have emerged. These concepts of drag reduction mechanisms are summarized in the following discussion.

A basic idea of how rib structures might reduce drag was originally put forth by Bechert *et al.* (1986) and Bechert & Bartenwerfer (1989) and later refined (Bechert *et al.* 1990; Bruse *et al.* 1993). Their idea utilizes the viscous flow concept of a *protrusion height* to explain why cross-flow fluctuations should be attenuated. The protrusion height is defined as the distance between the rib tip and the apparent (or average) origin of a viscous shear flow velocity profile over the ribbed surface. Protrusion heights for both longitudinal and cross-flow are defined in figure 2.6. The theoretical calculations of longitudinal protrusion height h_{pl} for various riblet profiles presented by Bechert & Bartenwerfer (1989), were later repeated and extended to include the cross-flow protrusion height h_{pc} (Luchini *et al.* 1991). These results indicate that it is the difference Δh between the longitudinal and cross-flow protrusion heights which is important. Specifically, Bruse *et al.* (1993) argue that since the cross-flow protrusion height is always closer to the riblet tip, a three-dimensional disturbance above the riblet surface would experience higher shear stress in the cross-flow direction, thus reducing cross-flow fluctuations and, consequently, shear stress. This explanation appears to be physically sound and suggests the approximate scaling of drag reduction with $\Delta h/s$ which is observed. Still, it is somewhat incomplete in the sense that it does not address the issue of cause-and-effect interaction with specific near-wall structures; an essential matter if one hopes to develop better ways of reducing drag.

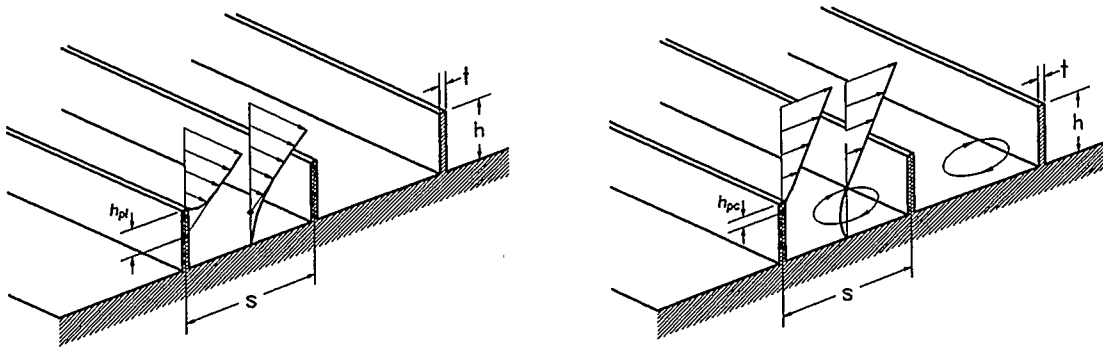


FIGURE 2.6. Viscous longitudinal and cross-flow protrusion heights of a ribbed surface.

Another explanation suggests that the observed drag reduction is due only to the low-speed region inside the valley of the riblets and, as such, drag reduction in laminar flow over riblets should also be expected (Djenidi *et al.* 1989). It is assumed that the local skin friction reduction in the valleys more than accounts for the increased wetted area and increased shear stress at the riblet peaks. For turbulent flow, properly sized riblets undoubtedly reduce the average shear stress over the surface, however, the sensitivity of the drag reduction level and range to riblet spacing and peak curvature would suggest that viscous effects alone cannot account for the observed drag reduction. Nevertheless, the conjecture of drag reduction in laminar flow will be investigated more thoroughly in the present study by exploring an existing analytical solution for laminar flow with blade-type riblets (Soliman & Feingold 1977). Two numerical studies of laminar channel flow with riblets have concluded that ribbed surfaces will always *increase* drag (Launder & Li 1989; Choi *et al.* 1991), though neither of these investigations have addressed the issue of protrusion height and the role it plays in determining the friction factor. Clearly, a more fundamental examination of all the issues is required.

A few models of riblet interaction with near-wall structures have been proposed. Choi (1989) has suggested a conceptual model for the near-wall region which involves the sweep of high momentum fluid toward the wall surface¹ between pairs of merging counter-rotating longitudinal vortices. Supposedly, the riblets would impede the lateral movement of the longitudinal vortices during the near-wall sweep, leading to a premature sweep of reduced duration and intensity; exactly how this process would occur has not been elucidated. Furthermore, the proposed mechanism relies on the implication that longitudinal vortices near the wall surface are essentially paired, even though experimental evidence in support of this inference is lacking.

Recently, a more fundamental influence of riblets on boundary layer structures has been suggested. Smith *et al.* (1991) reason that a likely effect of restricted lateral movement in the surface flow, due to riblets, is the less effective generation of local vorticity concentrations. Such concentrations are necessary for the formation of fluid eruptions near the surface and result from the imposed pressure gradient due to convecting hairpin vortices. Additional detailed turbulence measurements over riblet surfaces, which could confirm this mechanism, have not yet been acquired.

In light of the previous discussion it is evident that the physical explanation for riblet drag reduction is not yet complete, though it certainly appears that vortex interactions are at the root of the riblet drag-reducing mechanism and further investigation of such concepts is warranted.

¹ Choi (1989) has used the term *near-wall burst* to describe this event which is commonly known as a *sweep event* (Wallace *et al.* 1972; Willmarth & Lu 1972); a burst is usually associated with several *ejections* from a low speed streak.

Chapter 3

Friction Factor Measurements: Moderate Reynolds Number in Air Flow

A carefully designed experiment to accurately measure the friction factor in smooth and riblet-lined pipes was conducted in order to resolve uncertainties associated with previous pipe flow measurements. By paying close attention to experimental details related to flow metering and pressure taps, repeatability in the friction factor measurements of better than $\pm 0.2\%$ was achieved. In addition, the selection of very small riblets, relative to the pipe diameter, essentially eliminated any ambiguity in determining the effective pipe diameter. Details of the experimental apparatus, measurement techniques and the results of tests with two smooth pipes and four riblet-lined pipes over a wide Reynolds number range ($1 \times 10^4 - 2 \times 10^5$) are presented in this chapter.

3.1 Apparatus and Measurement Techniques

All experiments reported in this chapter were carried out in the Fluid Dynamics Laboratory at the Novacor Research & Technology Center. A special piping apparatus was designed and built for this study which utilized the existing air mover and the calibrated sonic nozzles which had been used in on-going acoustic and fluid dynamic research at the facility.

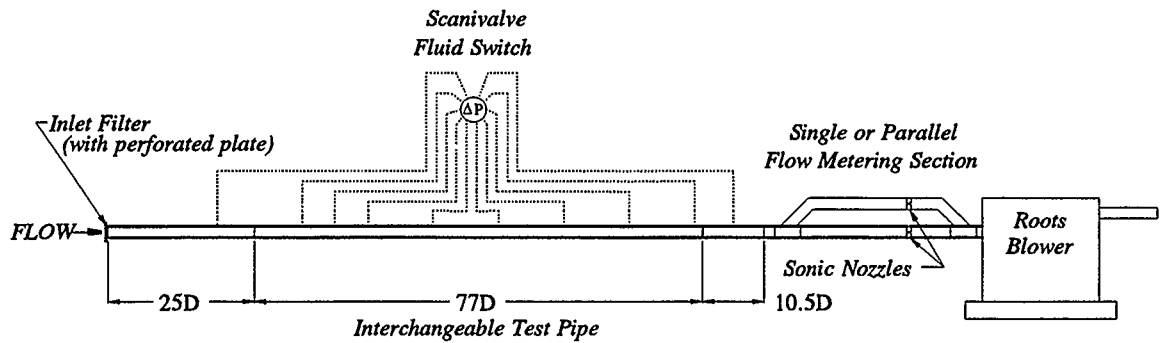


FIGURE 3.1. Schematic of open-loop apparatus with interchangeable test pipes.

3.1.1 Test facility

The apparatus consisted of an adaptable test section, a flow metering section, and a Roots blower as shown schematically in figure 3.1. Still air from the 1000 m³ laboratory was drawn into the test section through an inlet filter followed by a perforated plate to promote flow development. The perforated plate had 4.5 mm diameter holes on 6.5 mm centers (porosity = 44 %) and spanned the entire pipe cross-section.

The test section consisted of aluminum piping with an internal diameter of 95.45 mm and a honed surface finish of better than $R_a = 0.5 \mu\text{m}$ (relative roughness $\epsilon/D = 0.000005$). A flow development section of 2.375 m in length was followed by the interchangeable test pipe (7.316 m long), and a downstream spool piece of 1.000 m in length. Special split-ring flange joints resulted in concentric alignment between the internal wall surfaces of the pipes of better than 50 μm . Three test pipes of length

7.316 m were built. Each consisted of the honed aluminum piping with eight sets of pressure taps located along the pipe length. For two of these pipes, small blocks (bosses) were welded every 250 mm along opposing sides of the pipe. These bosses were drilled and tapped before the entire pipe was split longitudinally through the drilled and tapped bosses, which then allowed the pipe to be clamped back together. Two solid aluminum gaskets with an O-ring groove were glued to one half of each split-pipe to make up the material removed by slitting. The split pipes allowed surface modifications, primarily in the form of thin riblet sheets, to be applied with relative ease and also allowed access to the pressure tap holes. The remaining unsplit pipe served as the reference smooth pipe.

Following the test section was either a single or parallel flow metering section. Each meter run with the respective metering section consisted of a single perforated plate, 21 pipe diameters of smooth plastic pipe, and a sonic nozzle. The parallel metering section not only significantly extended the flow operating range of the experiment but also allowed various combinations of nozzles, thus increasing the number of discrete flow rates which could be obtained using eleven individual nozzles.

Although the use of sonic nozzles restricts the experiment to discrete flow rates, this limitation is far outweighed by the quiescent flow obtained by placing the choked nozzle between the test section and the blower. Effectively isolating the test section from any flow or pressure fluctuations induced by the blower enables precise measurements of pressure drop along the pipe axis to be made with a high degree of repeatability. Calibration of the sonic nozzles was carried out by an outside agency (CEESI) using secondary standard nozzles which had been calibrated against a primary standard (gravimetric facility). With this arrangement the flow rate could be determined with an absolute accuracy of about ± 0.5 %.

3.1.2 Instrumentation and data analysis

A minimal amount of instrumentation was required to measure pressure drop along the test pipe and mass flow rate through the sonic nozzle in order to determine the friction factor. Each of the eight sets of pressure taps, located along the test pipes, consisted of four equally spaced circumferential taps forming a Triple-T connection which provides a true average of the pressure at a particular cross-section (Blake 1976). Triple-T reference taps were also located 500 mm upstream and downstream of the test pipe in the flow development and downstream spool pieces, respectively. Gauge lines consisting of 1/8" (3.175 mm) vinyl tubing connected each Triple-T to a Scanivalve fluid switch wafer. This fluid switch wafer is essentially a twelve-pole, single-throw fluid switch which allows one precision transducer to be used to make all the pressure drop measurements. Connected to the collector port of the fluid switch was a capacitance-type Datametrix Barocel 590 pressure transducer with a full scale range of 0-1000 Pa differential and a quoted accuracy of 0.05 % of reading.

Mass flow rate through the choked nozzle was determined by measuring the static pressure and temperature one pipe diameter upstream of the nozzle and utilizing the nozzle calibration data. The pressure tap one pipe diameter upstream of the nozzle was also connected to the fluid switch and pressure transducer arrangement described above. Temperature was measured with a mercury thermometer (0-50°C with 0.1° divisions) mounted inside the pipe. Density was calculated from the ideal gas law.

The friction factor could be determined using the following expression

$$\lambda = \frac{\pi^2 \Delta P}{8 L} \frac{\rho D_{eff}^5}{\dot{m}^2} \quad (3.1)$$

where the basic uncertainty for each measured parameter is listed in table 3.1. Friction velocity was determined from

$$u_{\tau} = \sqrt{\frac{D_{eff} \Delta P}{4\rho L}} \quad (3.2)$$

The effective diameter for the riblet-lined pipes was defined as the diameter equivalent to a perfectly round smooth pipe having the same cross-sectional area. By measuring the volume of water necessary to fill the test pipe, an average cross-sectional area could be determined with a high degree of accuracy.

Parameter	Absolute Uncertainty	Relative Uncertainty %
L	0.5 mm	0.01-0.03
D_{eff}	25 μm	0.05
ΔP	0.1 Pa	0.01-5.0
\dot{m}	—	0.5
ρ	—	0.1

TABLE 3.1. Uncertainty of basic measurement parameters for friction factor analysis.

Applying a Constant-Odds uncertainty analysis (Kline & McClintock 1953) to (3.1)

$$\frac{\delta\lambda}{\lambda} = \left\{ \left(\frac{\delta\Delta P}{\Delta P} \right)^2 + \left(\frac{5\delta D_{eff}}{D_{eff}} \right)^2 + \left(\frac{\delta L}{L} \right)^2 + \left(\frac{2\delta\dot{m}}{\dot{m}} \right)^2 + \left(\frac{\delta\rho}{\rho} \right)^2 \right\}^{1/2} \quad (3.3)$$

and using the values from table 3.1, a *maximum relative uncertainty* in the measured friction factor λ of about 1.1% can be expected over most of the Reynolds number range. The major contribution to this error is the flow rate measurement uncertainty, which is the same for all flow rates, followed by the error in pressure drop

measurement. At very low flow rates the error in pressure drop measurement increases because the background acoustical noise and the electrical noise of the pressure transducer become significant when compared with the very small pressure drop signal. However, to detect drag reduction within a particular apparatus, the *precision* error is more important than relative uncertainty since fixed (bias) errors likely remain constant. From the measurements, the repeatability of the measured friction factor was found to be better than 0.2% over almost the entire Reynolds number range.

A PC computer program using LabWindows C language libraries was written to automatically acquire the signal from the pressure transducer and advance the fluid switch. This was accomplished using a TransEra Modular Data Acquisition System (MDAS) with a 16 bit A/D converter and TTL outputs. The pressure at each tap was monitored for five seconds, proceeding in a sequential manner starting at the upstream tap. From these average pressures, the pressure gradient along the test pipe was determined, and having also calculated the mass flow rate, the friction factor was obtained.

All the measurements presented in the following section were made with the parallel nozzle metering section. Because this metering technique utilizes a 45° dividing tee upstream of the individual nozzle meter runs, it was suspected that the dividing flow could perhaps induce unsteadiness into the system which in turn could affect both the flow rate and pressure drop measurements. Thus, a comparison of the measured smooth pipe friction factor using the parallel metering section and the single meter run was made in the Reynolds number range (1×10^4 - 1×10^5) where either section could be used. The difference in friction factor over the entire Reynolds number range was within the 0.2 % repeatability of the measurements, indicating that the dividing tee did not affect the flow. This test also confirmed the excellent repeatability of the measurements.

3.2 Experiments with Smooth and Riblet Surfaces

Measurements of friction factor in the lower range of non-dimensional riblet heights ($1 < h^+ < 15$) were performed for scalloped-type riblets and two sizes of triangular ribs and compared with a smooth pipe benchmark. In addition, a test with triangular riblets covering only half of the pipe surface was also conducted. The results are reported in this section.

3.2.1 *Smooth pipe benchmark*

In order to make proper comparisons of friction measurements a smooth pipe benchmark is needed. Thus, the smooth unsplit reference pipe was first tested. A typical axial pressure profile obtained from the measurements is shown in figure 3.2, in which the first tap was located 35 pipe diameters from the pipe inlet. From figure 3.2 it is evident that a linear pressure gradient exists in the test pipe indicating fully developed flow. Friction factor measurements from this pipe were used as a benchmark. Next, one of the smooth split pipes was tested and compared to the reference pipe. The results, shown in figure 3.3, indicate quite clearly that the splitting of the pipe, and subsequent rejoining with a solid gasket to make up the material removed in slitting, had no effect on the measured smooth pipe friction factor. This test provided satisfactory evidence that any effect measured in a split pipe modified by the application of thin riblet sheets would result directly from the surface modification and would not be due to inherent differences between the split pipe and the unsplit benchmark pipe. Also shown in figure 3.3 is Prandtl's universal law of friction and the Blasius resistance formula, both of which are defined in the figure. It has been found (Schlichting 1979) that the Blasius formula is only valid for Reynolds numbers $Re_b \leq 1 \times 10^5$ while Prandtl's law is valid for higher Reynolds numbers. This trend is confirmed by the present experiments.

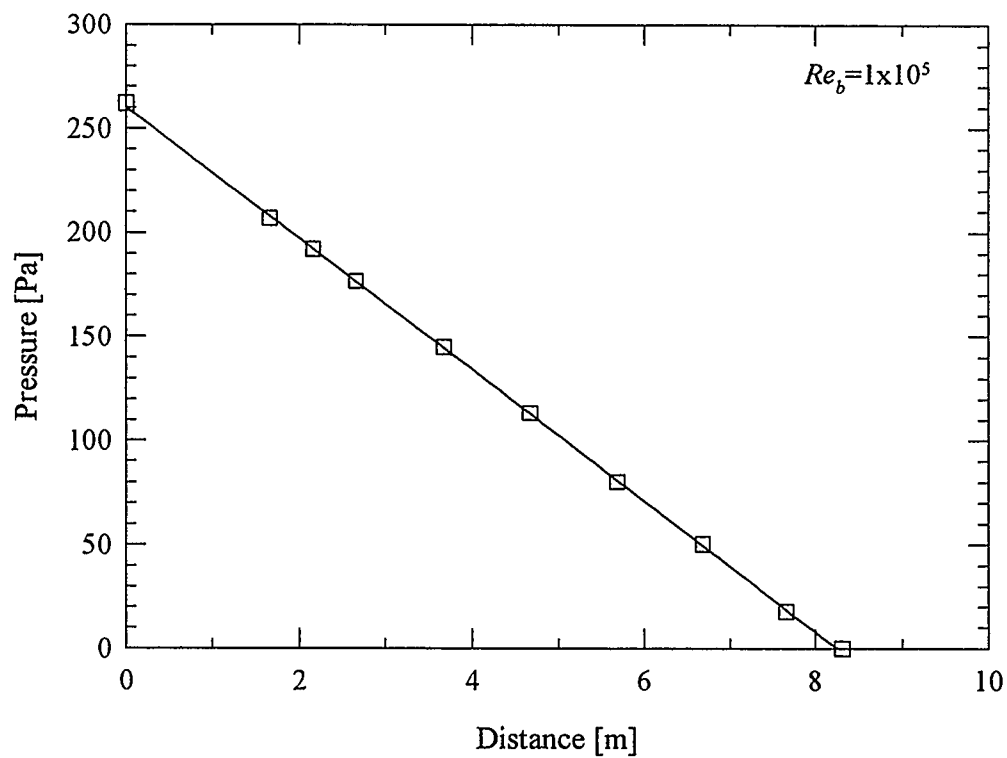


FIGURE 3.2. Typical pressure profile along the test pipe axis.

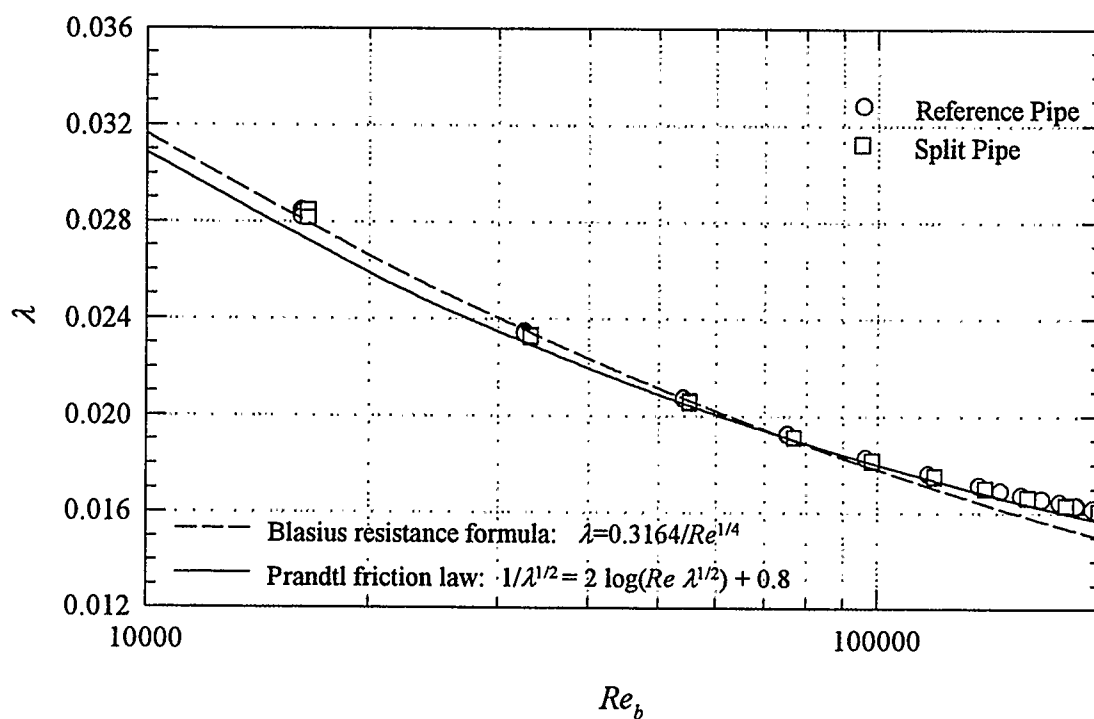


FIGURE 3.3. Measured friction factor in smooth pipes.

3.2.2 Tests of three different riblet surfaces

Next, friction factor measurements for three different types of thin riblet sheet attached to the pipe surface were performed. Scanning Electron Microscope (SEM) photographs of two sizes of triangular riblets purchased from the 3M company are shown in figures 3.4 and 3.5. Both sizes have an aspect ratio of approximately unity and are impregnated into a flexible plastic film having a base thickness of about $65\ \mu\text{m}$ with a self-adhesive backing. The smaller riblets have an average height of $120\ \mu\text{m}$ and are manufactured in a continuous roll 30 cm wide and 23 m long. The larger riblets are manufactured as individual sheets 29 cm wide and 91 cm long and have a height of about $150\ \mu\text{m}$. As seen in the SEM photographs, the $120\ \mu\text{m}$ triangular riblets exhibit a flattened peak with a sharp valley while the $150\ \mu\text{m}$ triangular riblets exhibit the exact opposite characteristics. This observation may explain some of the inconsistencies in previous pipe flow data (see figure 2.5) for which supposedly identically shaped riblets of different size provided quite different drag reduction characteristics. A third type of riblet film, manufactured by Hoechst AG in Germany, was kindly supplied by Dr. D.W. Bechert at DLR in Berlin and is shown in figure 3.6. This scalloped riblet configuration consisted of fairly sharp peaks spaced about $200\ \mu\text{m}$ apart and rising about $100\ \mu\text{m}$ above the bottom of rounded valleys. The profile was impregnated onto a semi-flexible plastic base of about $300\ \mu\text{m}$ thickness without a self-adhesive backing.

The riblet films were glued to the walls along the entire length (7.316 m) of the split pipes using the self-adhesive backing, except for the 3m long roll of Hoechst riblet film which was applied with double-sided adhesive tape starting about 1.2 m from the upstream end of the test pipe. While the triangular riblets encompassed the entire test pipe with its eight sets of pressure taps, the scalloped riblets only covered the first five sets of pressure taps.

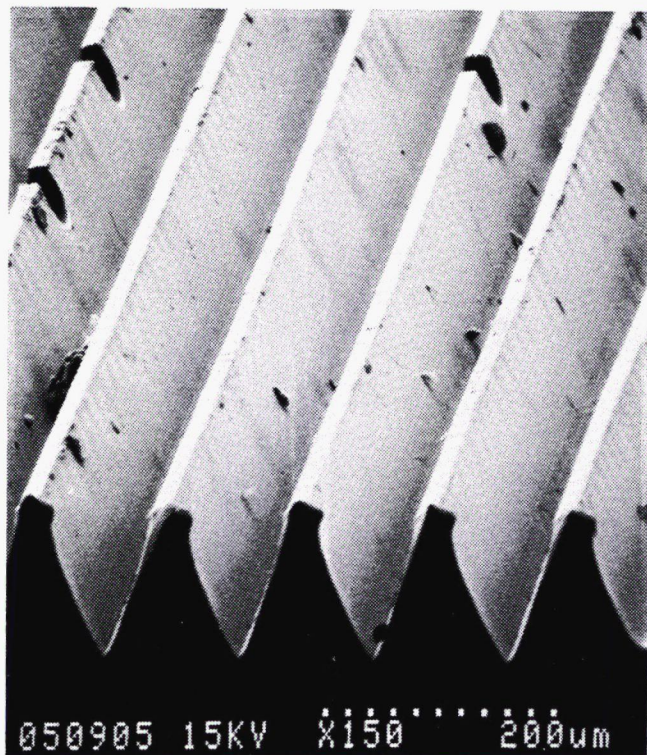


FIGURE 3.4. Triangular riblet sheet from 3M ($h = s = 120 \mu\text{m}$).

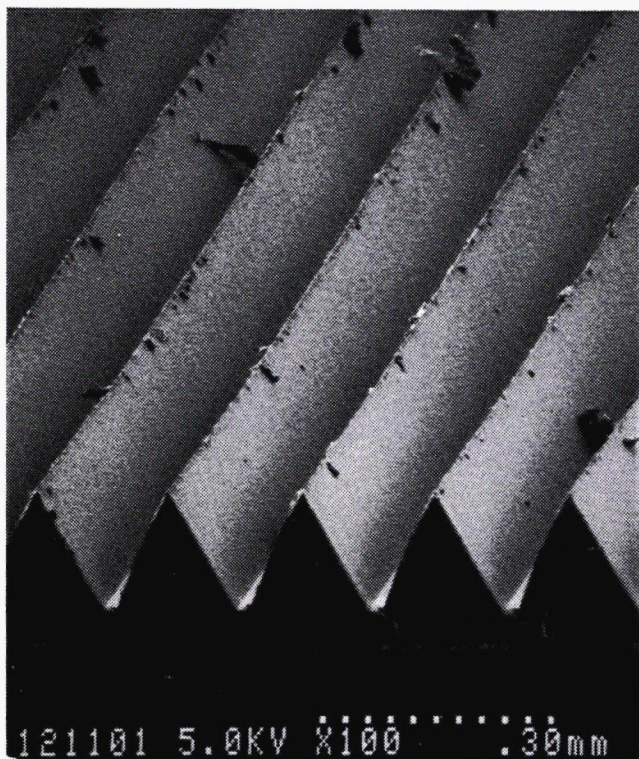


FIGURE 3.5. Triangular riblet sheet from 3M ($h = s = 150 \mu\text{m}$).

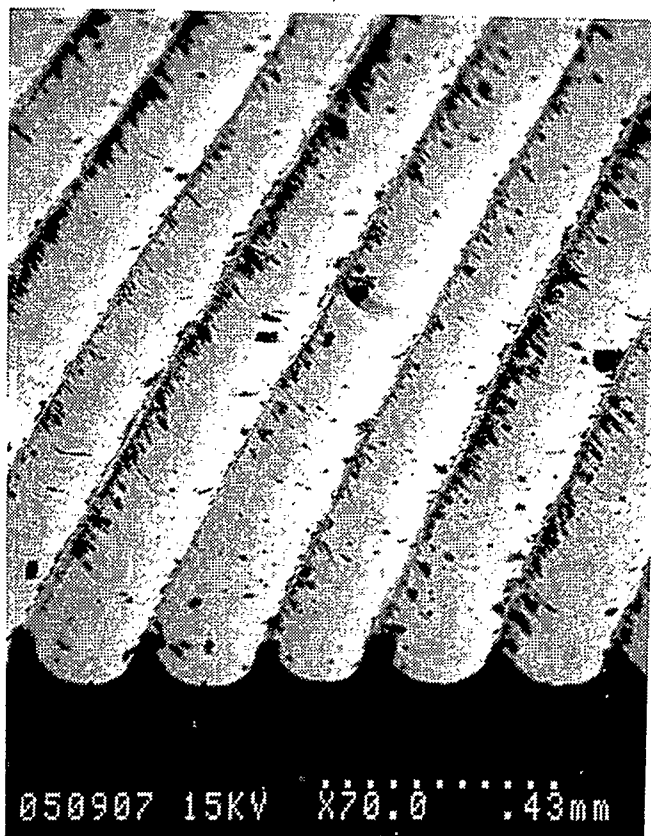


FIGURE 3.6. Scalloped riblet sheet from Hoechst AG ($h = 100 \mu\text{m}$; $s = 200 \mu\text{m}$).

Since the edge of the surface around a pressure tap can alter the measured pressure (Benedict 1984), a consistent geometry around all of the taps is required for proper results. This was accomplished using a small coring tool made from a 21 gage hypodermic needle (O.D. 0.8 mm) which was inserted through the pressure tap holes from the outside wall of the pipe, piercing the film and resulting in a clean hole. A SEM photograph of a piece of riblet sheet, which was previously located over a pressure tap on the pipe wall, is shown in figure 3.7. All holes were inspected in situ using an optical microscope and were found to be of the same quality as that shown in figure 3.7. Thus, even though the ribs may alter the measured pressure, essentially the same bias error would be introduced for all pressure taps, resulting in proper pressure drop measurements between any set of taps.



FIGURE 3.7. Typical cored pressure tap in a riblet sheet (large 3M triangular profile).

A comparison of the friction factor measured in the riblet-lined split pipes with that of the smooth pipe is shown in figure 3.8. The average pressure gradient determined from all but the first two taps in the test pipe was used in the calculation of the friction factor. Since the application of the riblet film to the internal walls reduces the inside cross-sectional area of the pipe, the effective diameter based on an equivalent cross-sectional area was used in the friction factor calculations. However, because the riblets are such a small fraction of the pipe diameter ($h/D < 0.0016$), the friction factor would differ by only $\pm 0.4\%$ if the riblet tip-to-tip or valley-to-valley diameter rather than the effective diameter based on equivalent cross sectional area were used in the

calculations. The measured results presented here unequivocally demonstrate drag reduction with properly sized riblets in pipe flow.

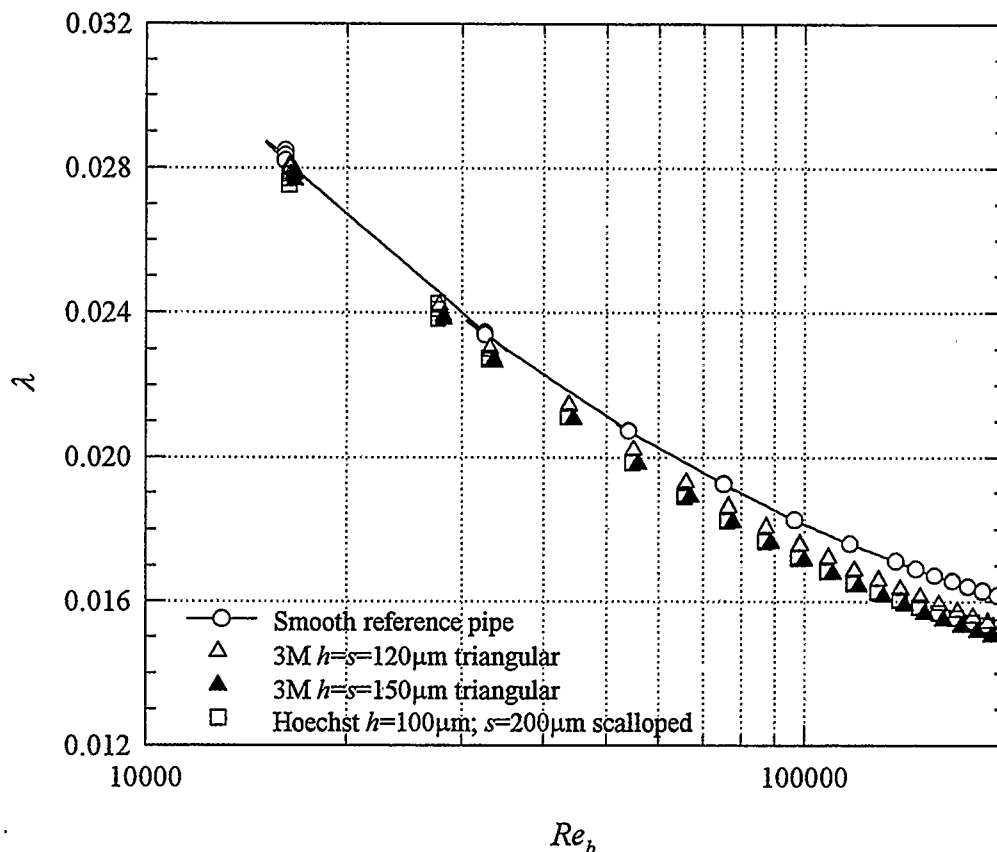


FIGURE 3.8. Friction factor measurements in riblet-lined pipes.

In figure 3.8, at least three experimental data points are plotted for every pipe at any particular Reynolds number. Close inspection of the figure indicates that for all but the lowest Reynolds numbers these individual data points essentially collapse on a single point, portraying the very good repeatability of the experiments. Using the smooth pipe as a reference, the amount of drag reduction for the three riblet types is plotted against the non-dimensional riblet height in figure 3.9. Here drag reduction is defined as

$$\text{drag reduction} = \frac{\lambda_{smooth} - \lambda_{rib}}{\lambda_{smooth}} \quad (3.4)$$

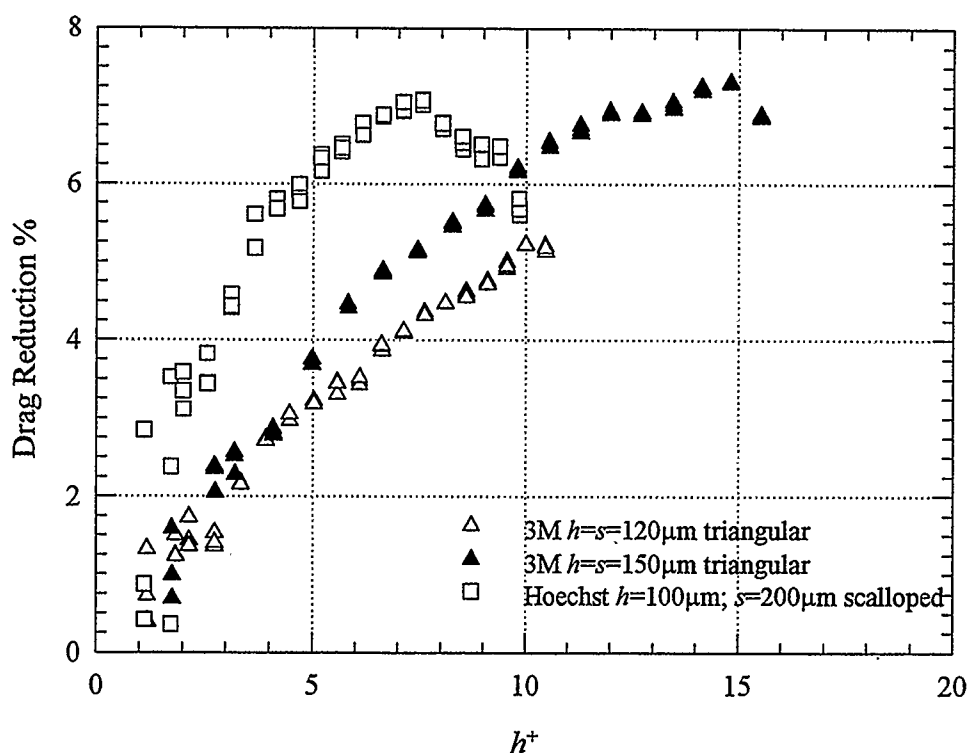


FIGURE 3.9. Drag reduction in riblet-lined pipes compared to smooth pipes.

A maximum drag reduction of about 7 % occurs at a non-dimensional height of about 15 for the large triangular 3M riblets with sharp peaks (see figure 3.5 for photograph of riblet surface) which, as expected, portrays better performance than the smaller ones with the somewhat flattened peaks (figure 3.4). The maximum drag reduction for the smaller triangular ribs was not quite reached but would appear to occur at a similar non-dimensional height as the larger ones but with at least 1% less drag reduction. For the scalloped riblets, the maximum level of drag reduction is about the same as for the larger triangular riblets but it occurs at a much lower value of non-dimensional height. Considering the aspect ratio and quality of the scalloped riblet surface (figure 3.6), the results are consistent with drag measurements of similar surfaces in channel flow (Bruse *et al.* 1993). For all three types of riblets tested, significant amounts of drag reduction already occur at very small non-dimensional riblet heights.

3.2.3 Half-lined pipe test

A novel extension of the riblet tests was to remove the riblet film from one of the split pipe halves and measure the pressure drop. The results of this experiment are shown in figure 3.10. Again, an effective diameter based on an equivalent cross-sectional area has been used in the friction factor calculations. Perhaps not surprisingly, the observed drag reduction was about half that of the fully lined pipe. Since two taps of each Triple-T connection were in the smooth half of the pipe and the other two in the riblet-lined half, the pressure drop along the pipe using either or both pairs of taps could be measured. Subsequent tests revealed that the measured pressure drop was the same whether either or both pairs of taps were used. This result confirms that, for steady developed flow, the static pressure gradient along the pipe is a proper indication of the average wall shear stress in the pipe. Physically, different static pressures at the smooth and at the riblet walls would not be expected, since this would suggest an unsustainable secondary flow across the pipe.

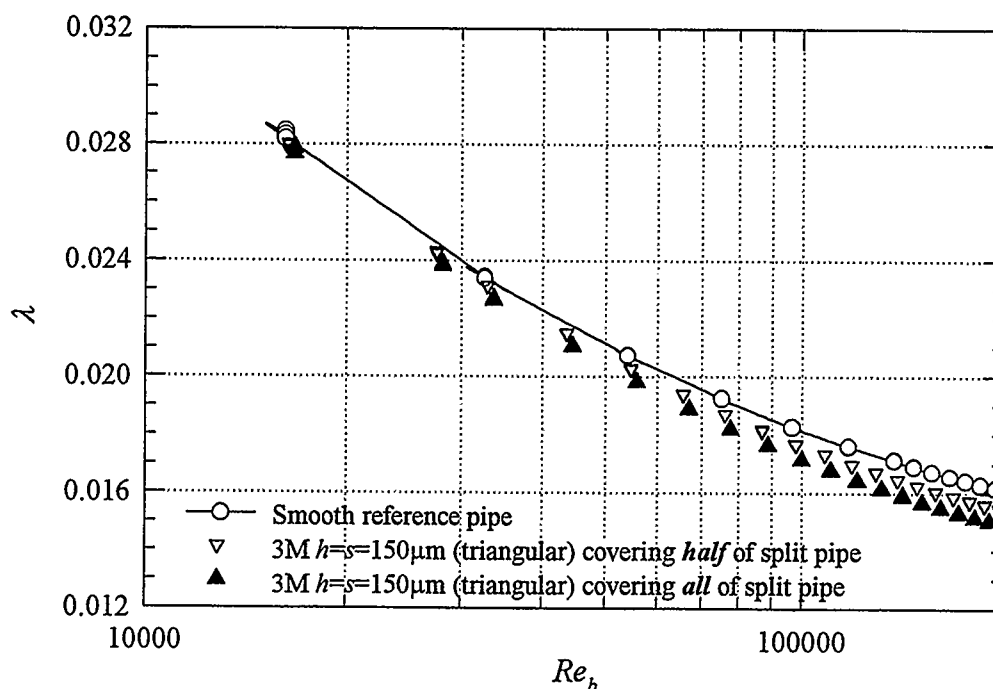


FIGURE 3.10. Friction factor measurements in a half-lined riblet pipe.

3.3 Summary of Results

Careful measurements of friction factor in smooth and riblet-lined pipes have provided unambiguous confirmation of drag reduction in turbulent air flow through pipes with properly sized riblets. The results indicate that drag reduction of about 7 percent is attainable using sharp-peaked triangular riblets with a non-dimensional height of about 15 wall units. Furthermore, significant amounts of drag reduction already occur at very small non-dimensional riblet heights ($2 < h^+ < 5$). Comparing the pipe flow results to channel or boundary layer flow with similar riblets, the maximum drag reduction level, as well as the non-dimensional height at which it occurs, were found to be virtually identical. This result is contrary to a previous finding of different riblet scaling in pipe flows compared to boundary layer flows (Nakao 1991). However, the friction factor calculations of Nakao (1991) did not include measurement of the pressure gradient *within* the riblet test pipe, rather only the measurement of pressure across the riblet test pipe was used. In such a case, effects due to a change in diameter at the entrance and exit of the test pipe are not factored out of the pressure gradient measurements. In particular for the large relative riblet sizes tested by Nakao (1991), the test pipe blockage effects, as well as the ambiguity in defining the effective diameter, will considerably influence the results.

Finally, a novel test, in which only half of the pipe periphery was covered with riblet sheets, was conducted. The measured drag reduction was about half of that measured with a completely lined pipe, confirming that the axial pressure gradient directly reflects the average wall shear stress at the pipe walls. Furthermore, the half-lined riblet experiment indicates that the riblet drag reduction mechanism is a very localized phenomenon.

Chapter 4

Friction Factor Measurements: High Reynolds Number in Natural Gas Flow

This chapter presents the results of a unique field experiment in which the friction factor for both a smooth and riblet-lined pipe was measured in a high pressure natural gas flow. Numerous technical difficulties associated with the high Reynolds number flow ($7.5 \times 10^5 < Re_b < 6.5 \times 10^6$) and the high pressure natural gas environment were overcome in making the measurements. Although the extremely small riblets tested were of non-optimum shape, the measurement of drag reduction was aided by the high Reynolds number for which the honed pipe was no longer hydraulically smooth.

4.1 High Pressure Test Facility

The experiments reported in this chapter were conducted at the NOVA CORPORATION OF ALBERTA Gas Dynamic Test Facility located 80 km northwest of Calgary, Alberta. The facility is part of an active compressor station site within the Alberta Gas Transmission Division's high pressure natural gas network and is used primarily for metering and compression research.

A general schematic view of a portion of the test facility is shown in figure 4.1. A centrifugal compressor is used to control flow within the test facility independent of the

flow through the station compressor. Any piping used in the facility must be pressure rated to at least one-and-a-half times the facility maximum operating pressure of 6000 kPa. Rather than design a special pressure rated piping section for the friction factor measurements, the aluminum piping used in the laboratory tests was mounted *inside* of the larger (300 mm diameter) high pressure piping, as shown in figure 4.2. An unsealed bellmouth inlet at the upstream end and a sealed flange on the downstream end were used to mount the 112 pipe diameter aluminum test section within the high pressure piping. The downstream seal forces all the gas through the aluminum piping while the unsealed bellmouth inlet allows gas to pack around the aluminum pipe. Thus, the aluminum pipe experiences a linearly varying positive pressure on the outside due to the flow pressure loss along the inside, since the gas packed around it is at the same pressure as the gas at the bellmouth inlet. This piping configuration implemented all the benefits of the split pipe arrangement within a high pressure natural gas environment.

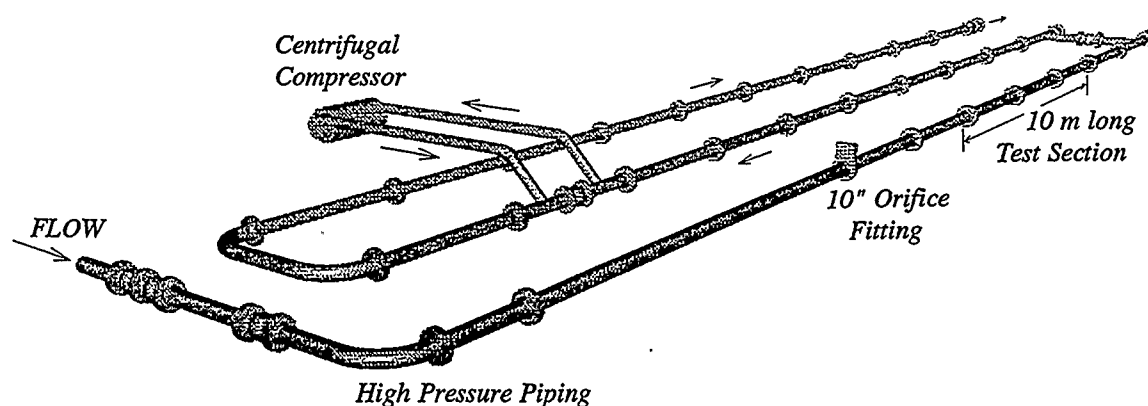


FIGURE 4.1. A portion of NOVA's Gas Dynamic Test Facility.

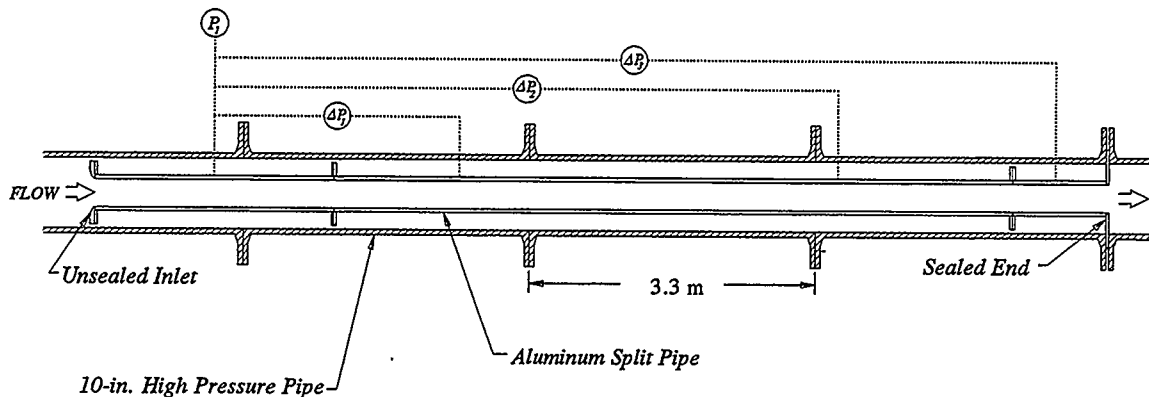


FIGURE 4.2. Schematic of test section within the larger high-pressure piping.

4.2 Instrumentation and Data Analysis

As with the laboratory experiments, a minimal amount of instrumentation was necessary to determine the mass flow rate and pressure drop within the test piping, both of which were required to calculate the friction factor.

Using the AGA Report No.3 standard for orifice metering, a 10-in. Senior Daniels orifice fitting with plates of $\beta = 0.15$, 0.2 and 0.3 was used to measure flow rate with an accuracy of $\pm 1.0\%$. The standard requires the static pressure and temperature upstream of the orifice and differential pressure across the orifice plate, all of which were measured with three suitable transmitters. Density was calculated using the AGA Report No.8 state equation for natural gas mixtures.

Since a Scanivalve fluid switch for high pressures was not readily available, only four sets of Triple-T pressure taps were utilized in the measurement of pressure drop along the test pipe. With the tap furthest upstream as a common reference, three individual differential pressure transmitters were used to measure the pressure at each of the other three tap locations. Accuracy of the differential pressure reading ranged

from 0.1-1.5 % of reading, depending on the transmitter and the pressure level. The static pressure at the upstream tap was also measured with an absolute pressure transmitter, as shown in figure 4.2. The 1/8-in. stainless steel tube gauge lines, leading from the Triple-T connections to the pressure transmitter, were routed out of the larger high pressure pipe using flexible stainless steel hose attached to special bored-through Swagelok fittings.

A general LabWindows based data acquisition software, developed in the course of the present study, was used to acquire data simultaneously from all seven transducers at a sampling frequency of 40 Hz. For each data point, the data signals were averaged over a 25 second time period and then used to calculate the friction factor. Using the quoted uncertainty of pressure drop and orifice flow rate, with additional values from table 3.1, a maximum *relative uncertainty* in the measured friction factor of 2.5% was calculated from equation (3.3). However, the *precision* error between friction factor measurements in the smooth and riblet-lined pipe is around 1%.

4.3 Experimental Results

In Section 2.1.1 it was pointed out that, for a given pipe diameter, the viscous wall unit size decreases with increasing Reynolds number. For the present study, the Reynolds number was of order 10^6 for which the ratio of viscous wall unit to pipe diameter is about 1×10^{-5} (see figure 2.3). Thus, a physical riblet height of about 10 μm is required to procure optimum drag reduction. A riblet film purchased from 3M for this study was supposed to have triangular riblets with both height and spacing of 4 μm . However, the SEM photograph in figure 4.3 revealed the disappointing result that only the height was 4 μm while the spacing was about 23 μm . Such an aspect ratio is far from optimum and even under ideal conditions a drag reduction of no more than

about 2 percent could be expected compared with a hydraulically smooth surface. Furthermore, the optimum drag reduction for this riblet geometry occurs at flow rates for which the pressure drop is quite small, making measurements in a field application more difficult. The measurements were further complicated by the presence of low frequency pressure pulsations in the pipeline which, for very low flow rates, were the same order of magnitude as the pressure drop being measured. The latter problem was circumvented by averaging the pressure drop signal over longer periods of time.

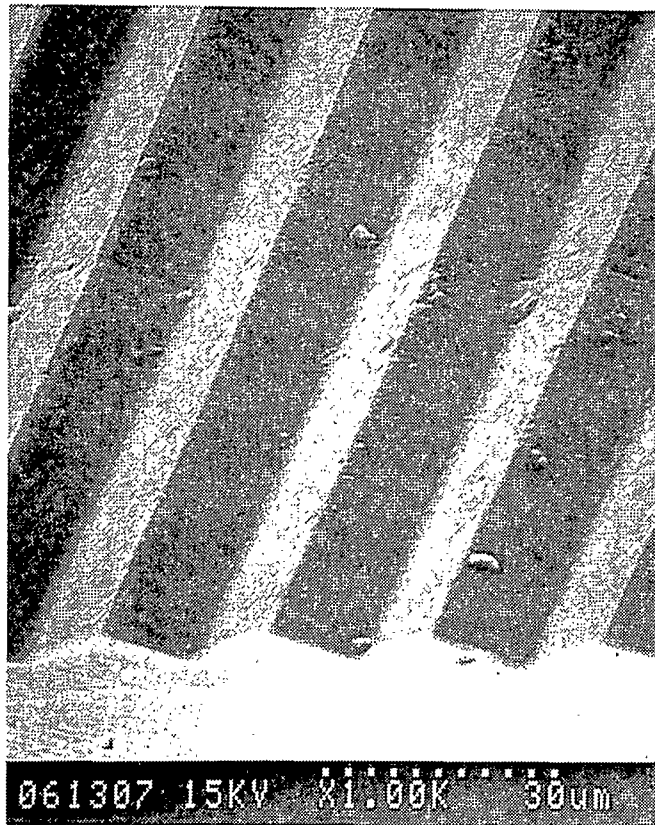


FIGURE 4.3. Low aspect ratio triangular riblet sheet from 3M ($h = 4 \mu\text{m}$; $s = 23 \mu\text{m}$).

The unsplit smooth reference pipe was tested first and then replaced with the split pipe which had been internally covered with the riblet sheet shown in figure 4.3. The resulting friction factor measurements are given in figure 4.4 where drag reduction with respect to the smooth pipe is evident. Although the relative roughness of the

smooth pipe is very small ($\epsilon/D = 0.000005$) the pipe is no longer hydraulically smooth at such large Reynolds numbers, due to the extremely thin viscous sublayer. For this reason, drag reduction even with a non-optimum riblet shape is significant, since the comparison is no longer with a hydraulically smooth surface. In figure 4.5, the friction factor measurements are plotted in terms of drag reduction as a function of the non-dimensional riblet height. Low levels of drag reduction over a wide range are evident with a maximum of about 5% occurring at a non-dimensional rib height of about two. This result is again consistent with flat-plate boundary layer measurements of similar sized riblets (Walsh 1982) and provide the first confirmation of drag reduction with riblets in a high Reynolds number pipe flow within a high pressure natural gas environment.

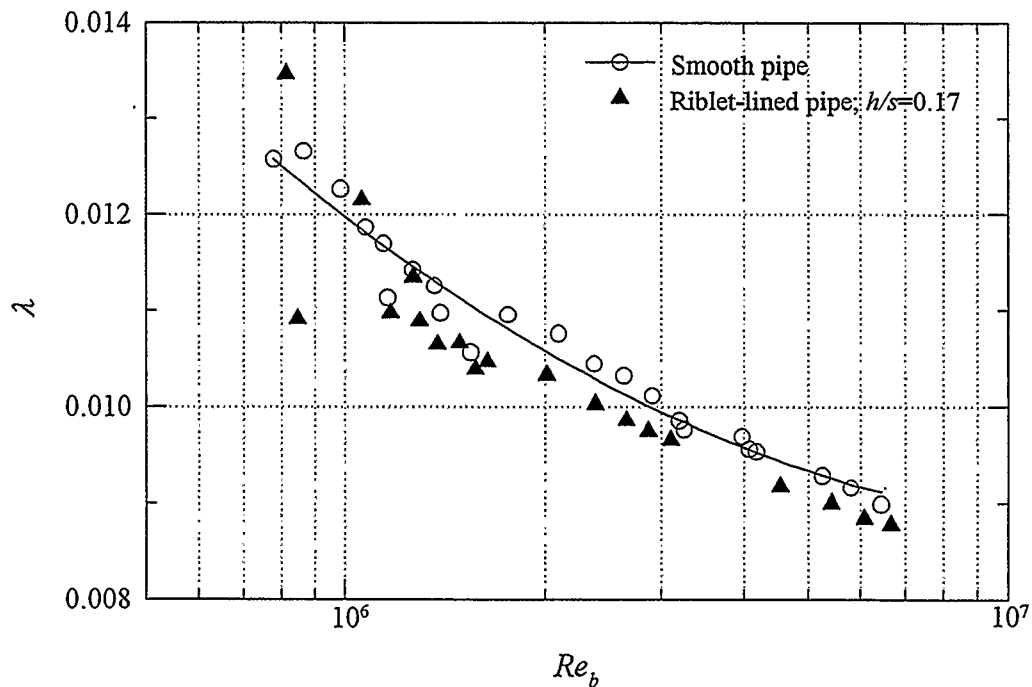


FIGURE 4.4. Friction factor measurements in smooth and riblet pipe at high pressure.

The results in figures 4.4 and 4.5 unfortunately could not be repeated due to a partial de-pressurization of the test facility which caused the riblet film to blister away from the wall. Small amounts of high pressure gas became entrained in tiny air

bubbles under the film which then forced the film away from the wall in the form of large bubbles or blisters, rendering the modified surface useless for drag reduction measurements. Nevertheless, the limited data qualitatively confirm the phenomenon.

Despite the difficulties encountered in the field experiments, there is sufficient evidence to suggest that levels of drag reduction similar to that measured in the laboratory can be obtained in field applications. Furthermore, for high Reynolds number flows, even higher levels of drag reduction with riblets occurs since pipes with even relatively small roughness are no longer hydraulically smooth. In terms of utilization within the natural gas industry, however, the degree to which the riblet profiles would deteriorate or become fouled over time in an actual field application remains to be determined.

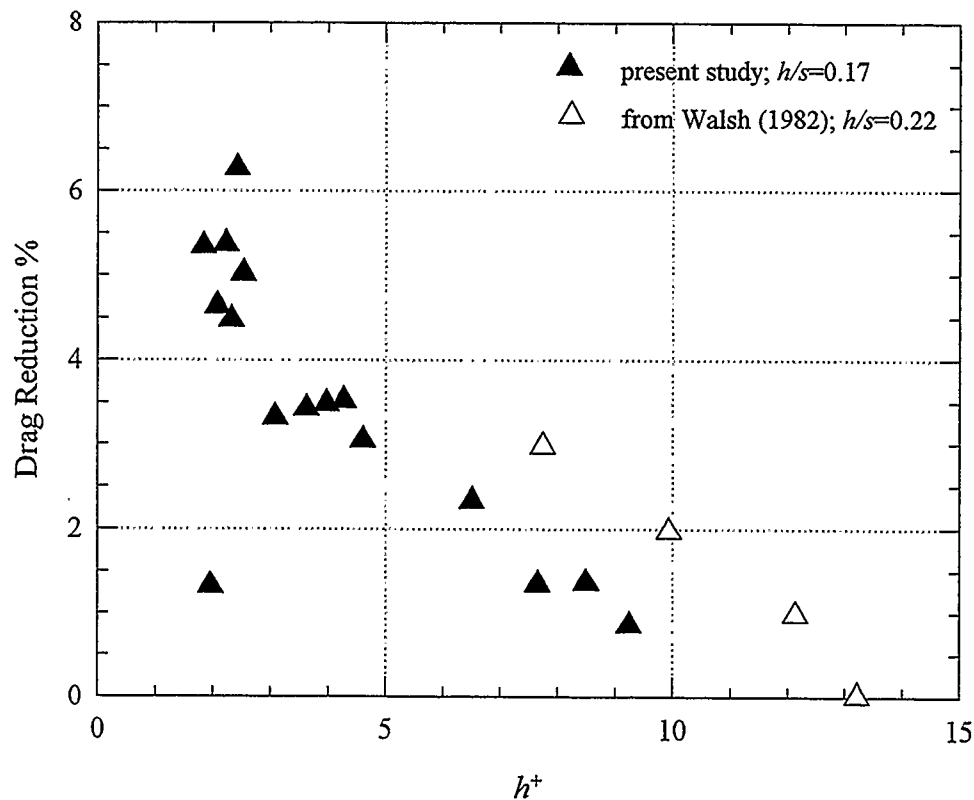


FIGURE 4.5. Drag reduction with riblets in high Reynolds number pipe flow.

Chapter 5

Consideration of Viscous Effects

Many independent experiments, including the ones reported in the previous two chapters, have confirmed that riblets reduce skin friction drag in turbulent flow when the ribs protrude less than a few viscous sublayer thicknesses from the wall. Because of this scaling, it has been suggested that viscous effects at the wall are primarily responsible for the observed drag reduction rather than interaction of the ribs with the turbulence structure near the wall. In this chapter, viscous effects are examined by exploring and extending an analytical solution for laminar flow in pipes with blade-type riblets. In particular, the virtual origin of the streamwise velocity profile over the ribbed surface is considered in some detail and its meaning in terms of drag reduction is investigated.

5.1 Laminar Flow in Pipes with Blade-type Riblets

In turbulent flow, it is reported that thin blade-type riblets produce drag reductions of up to nine percent (Wilkinson & Lazos 1987; Bruse *et al.* 1993). Here, however, *laminar* pipe flow with similar riblets will be considered in order to obtain a more fundamental understanding of the viscous effects associated with riblets.

5.1.1 Description of the geometry

The basic geometry considered is shown in figure 5.1. Assuming fully developed laminar flow, the momentum equation governing the flow is:

$$\frac{1}{r} \frac{\partial}{\partial r} \left(r \frac{\partial U}{\partial r} \right) + \frac{1}{r^2} \frac{\partial^2 U}{\partial \theta^2} = \frac{1}{\mu} \frac{dP}{dx} \quad (5.1)$$

Making use of symmetry planes and splitting the circularly symmetric domain into two regions, the following boundary value problem results. The equations have been expressed in non-dimensional form.

$$\frac{1}{\hat{R}} \frac{\partial}{\partial \hat{R}} \left(\hat{R} \frac{\partial \hat{U}}{\partial \hat{R}} \right) + \frac{1}{\hat{R}^2} \frac{\partial^2 \hat{U}}{\partial \theta^2} = -1 \quad (5.2)$$

Region 1

$$\hat{U}_1 = 0 \text{ at } \hat{R}=1 \quad 0 \leq \theta \leq \alpha$$

$$\hat{U}_1 = 0 \text{ at } \hat{R}_i \leq \hat{R} \leq 1 \quad \theta = \alpha$$

$$\frac{\partial \hat{U}_1}{\partial \theta} = 0 \text{ at } \hat{R}_i \leq \hat{R} \leq 1 \quad \theta = 0$$

Region 2

$$\frac{\partial \hat{U}_2}{\partial \theta} = 0 \text{ at } 0 \leq \hat{R} \leq \hat{R}_i \quad \theta = 0$$

$$\frac{\partial \hat{U}_2}{\partial \theta} = 0 \text{ at } 0 \leq \hat{R} \leq \hat{R}_i \quad \theta = \gamma$$

$$\frac{\partial \hat{U}_2}{\partial \hat{R}} = 0 \text{ at } \hat{R}=0 \quad \text{all } \theta$$

and at the interface between regions 1 and 2 there must be continuity of velocity and shear stress

$$\hat{U}_2(\hat{R}_i, \theta) = \hat{U}_1(\hat{R}_i, \theta) \quad 0 \leq \theta \leq \alpha \quad \frac{\partial \hat{U}_2}{\partial \hat{R}}(\hat{R}_i, \theta) = \frac{\partial \hat{U}_1}{\partial \hat{R}}(\hat{R}_i, \theta) \quad 0 \leq \theta < \alpha$$

$$\hat{U}_2(\hat{R}_i, \theta) = 0 \quad \alpha \leq \theta \leq \gamma$$

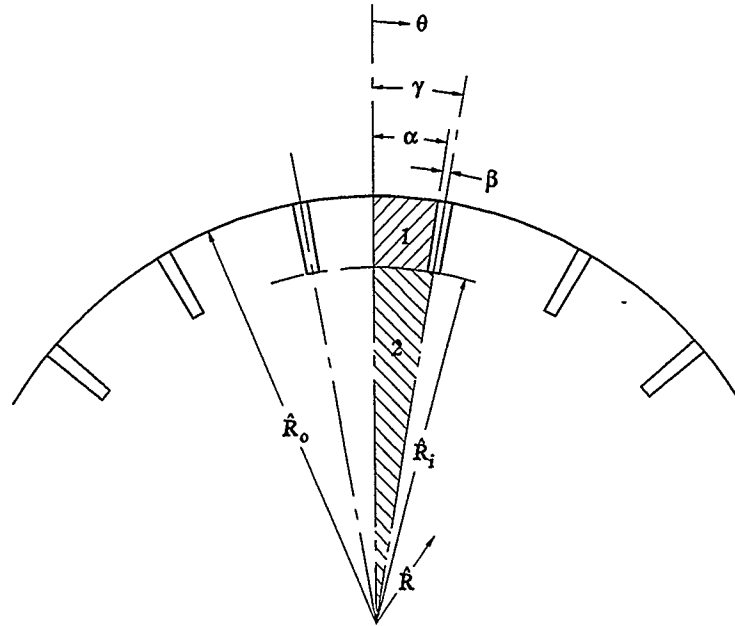


FIGURE 5.1. Blade-riblet flow field geometry.

5.1.2 Analytical solution of the governing equations

An analytical solution for the velocity distribution within the two regions was obtained by Soliman & Feingold (1977) in the form of an infinite series and the results follow.

$$\hat{U}_1 = \sum_{j=1}^N \frac{-4(-1)^j}{(2j-1)\pi \{(j-\frac{1}{2})^2 M^2 \omega^2 - 4\}} (\hat{R}^2 - \hat{R}^{(j-\frac{1}{2})M\omega}) \cos\left(\frac{2j-1}{2} M\omega\theta\right) + \sum_{j=1}^N b_j \hat{R}^{-(j-\frac{1}{2})M\omega} (1 - \hat{R}^{(2j-1)M\omega}) \cos\left(\frac{2j-1}{2} M\omega\theta\right) \quad (5.3)$$

and

$$\hat{U}_2 = a_0 - \frac{\hat{R}^2}{4} + \sum_{j=1}^N a_j \hat{R}^{jM} \cos(jM\theta) \quad (5.4)$$

where the coefficients a_0 and a_j are defined as

$$a_0 = \frac{\hat{R}_i^2}{4} + \sum_{j=1}^N \frac{8}{(2j-1)^2 \pi^2 \omega \{(j-1/2)^2 M^2 \omega^2 - 4\}} (\hat{R}_i^2 - \hat{R}_i^{(j-1/2)M\omega}) - \sum_{j=1}^N \frac{2(-1)^j}{\pi \omega (2j-1)} b_j \hat{R}_i^{-(j-1/2)M\omega} (1 - \hat{R}_i^{(2j-1)M\omega}) \quad (5.5)$$

and

$$\frac{a_j \hat{R}_i^{jM}}{\cos(jM\alpha)} = \sum_{k=1}^N \frac{4\omega (\hat{R}_i^2 - \hat{R}_i^{(k-1/2)M\omega})}{\pi^2 \{(k-1/2)^2 M^2 \omega^2 - 4\} \{(k-1/2)^2 \omega^2 - j^2\}} - \sum_{k=1}^N \frac{2b_k}{\pi} \hat{R}_i^{-(k-1/2)M\omega} (1 - \hat{R}_i^{(2k-1)M\omega}) \left\{ \frac{(k-1/2)(-1)^k \omega}{(k-1/2)^2 \omega^2 - j^2} \right\} \quad (5.6)$$

The constants b_j are determined by applying the continuity of the radial velocity gradient along N equally spaced points on the interface between regions 1 and 2 corresponding to $\theta = 0, \Delta\theta, 2\Delta\theta, \dots, (N-1)\Delta\theta$ where $\Delta\theta = \alpha/N$. This results in a system of linear algebraic equations (which was solved using LU decomposition) of the form

$$G_{n,j} Z_j = H_n \quad (5.7)$$

where

$$G_{n,j} = \frac{2(-1)^j (j-1/2)M\omega}{\pi \hat{R}_i} (1 - \hat{R}_i^{(2j-1)M\omega}) \sum_{k=1}^N \frac{k \cos\{kM(n-1)\Delta\theta\} \cos(kM\alpha)}{(j-1/2)^2 \omega^2 - k^2} - \frac{(j-1/2)M\omega}{\hat{R}_i} (1 + \hat{R}_i^{(2j-1)M\omega}) \cos\left\{ \frac{2j-1}{2} M\omega(n-1)\Delta\theta \right\} \quad (5.8)$$

$$Z_j = b_j \hat{R}_i^{-(j-1/2)M\omega} \quad (5.9)$$

$$H_n = -\frac{\hat{R}_i}{2} + \sum_{j=1}^N \left[\frac{jM \cos\{jM(n-I)\Delta\theta\} \cos(jM\alpha)}{\pi^2 \hat{R}_i} \sum_{k=1}^N \frac{4\omega(\hat{R}_i^2 - \hat{R}_i^{(k-1/2)M\omega})}{\{(k-1/2)^2 M^2 \omega^2 - 4\} \{(k-1/2)^2 \omega^2 - j^2\}} \right] + \sum_{j=1}^N \frac{4(-1)^j}{(2j-1)\pi \{(j-1/2)^2 M^2 \omega^2 - 4\}} \left(2\hat{R}_i - \frac{2j-1}{2} M\omega \hat{R}_i^{(j-1/2)M\omega-1} \right) \cos\left\{ \frac{2j-1}{2} M\omega(n-I)\Delta\theta \right\} \quad (5.10)$$

5.1.3 Shear stress and friction factor calculations

Now, using Soliman & Feingold's (1977) solution for the velocity distribution as a starting point, the shear stress along the pipe wall and the rib wall and tip can be integrated to find a new expression for the non-dimensional shear force per unit length

$$\frac{\hat{F}_\tau}{\hat{L}} = 2M \left[\int_{\theta=0}^{\theta=\alpha} \frac{\partial \hat{U}_1}{\partial \hat{R}} \hat{R} \Big|_{\hat{R}=1} d\theta + \int_{\hat{R}=\hat{R}_i}^{\hat{R}=1} \frac{1}{\hat{R}} \frac{\partial \hat{U}_1}{\partial \theta} \Big|_{\theta=\alpha} d\hat{R} + \int_{\theta=\alpha}^{\theta=\gamma} \frac{\partial \hat{U}_2}{\partial \hat{R}} \Big|_{\hat{R}=\hat{R}_i} \hat{R}_i d\theta \right] \quad (5.11)$$

$$\int_{\theta=0}^{\theta=\alpha} \frac{\partial \hat{U}_1}{\partial \hat{R}} \hat{R} \Big|_{\hat{R}=1} d\theta = \sum_{j=1}^N \frac{4}{(2j-1)(j-1/2)M\omega\pi \{(j-1/2)M\omega + 2\}} + \sum_{j=1}^N 2b_j (-1)^j \quad (5.12)$$

$$\int_{\hat{R}=\hat{R}_i}^{\hat{R}=1} \frac{1}{\hat{R}} \frac{\partial \hat{U}_1}{\partial \theta} \Big|_{\theta=\alpha} d\hat{R} = \sum_{j=1}^N \frac{-2M\omega}{\pi \{(j-1/2)^2 M^2 \omega^2 - 4\}} \left(\frac{1 - \hat{R}_i^2}{2} + \frac{\hat{R}_i^{(j-1/2)M\omega} - 1}{(j-1/2)M\omega} \right) + \sum_{j=1}^N b_j (-1)^j \frac{2j-1}{2} \left(\frac{\hat{R}_i^{-(j-1/2)M\omega} + \hat{R}_i^{(j-1/2)M\omega} - 2}{j-1/2} \right) \quad (5.13)$$

$$\int_{\theta=\alpha}^{\theta=\gamma} \frac{\partial \hat{U}_2}{\partial \hat{R}} \Big|_{\hat{R}=\hat{R}_i} \hat{R}_i d\theta = -\frac{\hat{R}_i^2(\gamma - \alpha)}{2} - \sum_{j=1}^N a_j \hat{R}_i^{jM} \sin(jM\alpha) \quad (5.14)$$

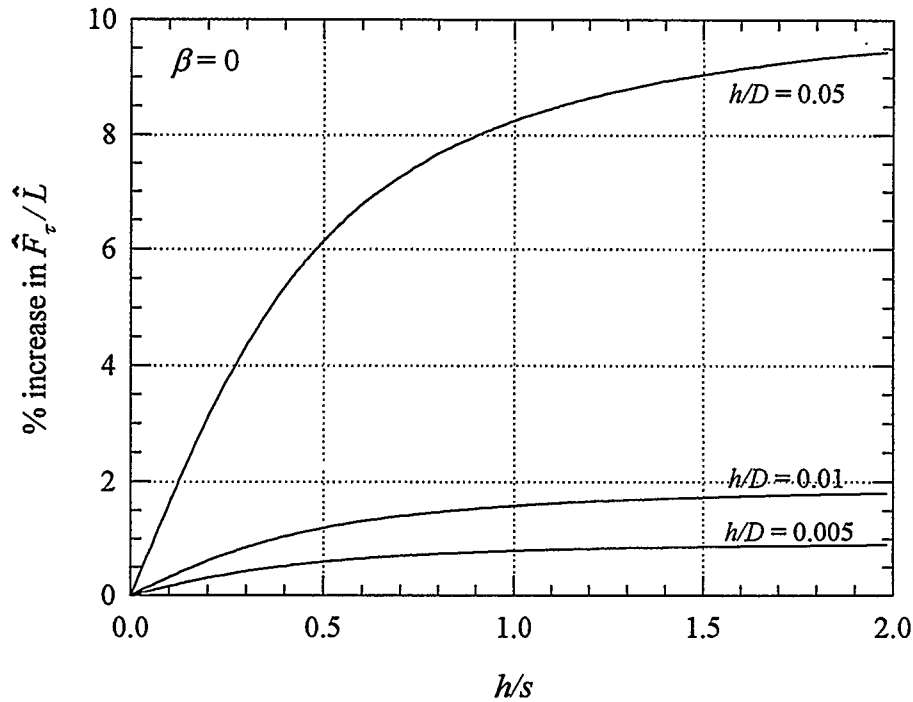


FIGURE 5.2. Effect of blade ribs on dimensionless shear stress per unit length.

For a pipe flow, the integrated shear stress is directly balanced by the pressure gradient. As such, it is convenient to also consider the product of friction factor and Reynolds number λRe which is commonly used in laminar flows since it is a constant for smooth surfaces (i.e. $\lambda Re = 64$ for pipes):

$$\lambda Re = \frac{\pi}{\pi - M\beta(1 - \hat{R}_i^2)} \frac{8}{\hat{U}_b} \quad (5.15)$$

When using (5.15) to compare ribbed and smooth pipes, some ambiguity is involved since the Reynolds number includes a characteristic length, which in the above definition is the radius measured from the pipe centerline to the valley of the ribs (i.e. R_o). However, solving (5.11) for a fixed mass flow rate and pipe radius, it is evident that the addition of ribs will *always* increase the total wall shear stress, as shown in figure 5.2. The physical explanation is simply that the ribs decrease the mass flow rate through the pipe if a fixed pressure gradient is applied. Clearly, for a smooth pipe and

a ribbed pipe of the same cross-sectional flow area, the ribbed pipe will always experience a drag increase, even if the ribs are small and infinitely thin. This result, however, leads to the question of whether or not a proper comparison should be based on an equivalent cross-sectional area or some other effective pipe diameter—an issue which will be examined in the following section.

5.1.4 Implications of protrusion heights

The concept of a protrusion height was introduced by Bechert & Bartenwerfer (1989) and has already been briefly mentioned in Section 2.5. To reiterate, the protrusion height is defined as the distance between the rib tip and the apparent (or average) origin of a viscous shear flow velocity profile over the ribbed surface. Protrusion heights for both longitudinal and cross-flow can be determined and have been illustrated in figure 2.6. Here, for laminar pipe flow with blade riblets, only the longitudinal protrusion height is considered.

Returning now to the question of the proper comparison of ribbed and smooth pipes, it is useful to consider a fundamental principle related to the shear stress in smooth pipes: for a given mass flow rate, an increased shear stress also results if the pipe diameter is decreased. Thus, the shear stress in a ribbed pipe can be made equivalent to that of a different sized (i.e. smaller diameter) smooth pipe. From (5.11) and (5.15) it can be shown that such an equivalent diameter coincides precisely with the effective pipe diameter based on the apparent origin of the velocity profile above the ribs, which can be determined from the longitudinal protrusion height. In other words, the effective diameter as indicated by the apparent origin of the velocity profile in a ribbed pipe is identically the smooth pipe diameter which would produce the same shear stress. The longitudinal protrusion height for laminar pipe flow with blade riblets obtained from (5.11) and (5.15) is shown in figure 5.3 where it is compared with the

results of Bechert & Bartenwerfer (1989) which were determined from conformal mapping of a viscous shear flow over a blade riblet surface. The results are identical, hence, the comparison of smooth and ribbed pipes using an effective diameter based on the protrusion height indicates that the shear stress in laminar flow with ribbed pipes neither decreases nor increases—it remains the same. This result stresses the importance of knowing the effective inner diameter when making statements about friction losses in ribbed pipes. It also implies that viscous effects alone cannot explain the observed drag reduction in turbulent flow.

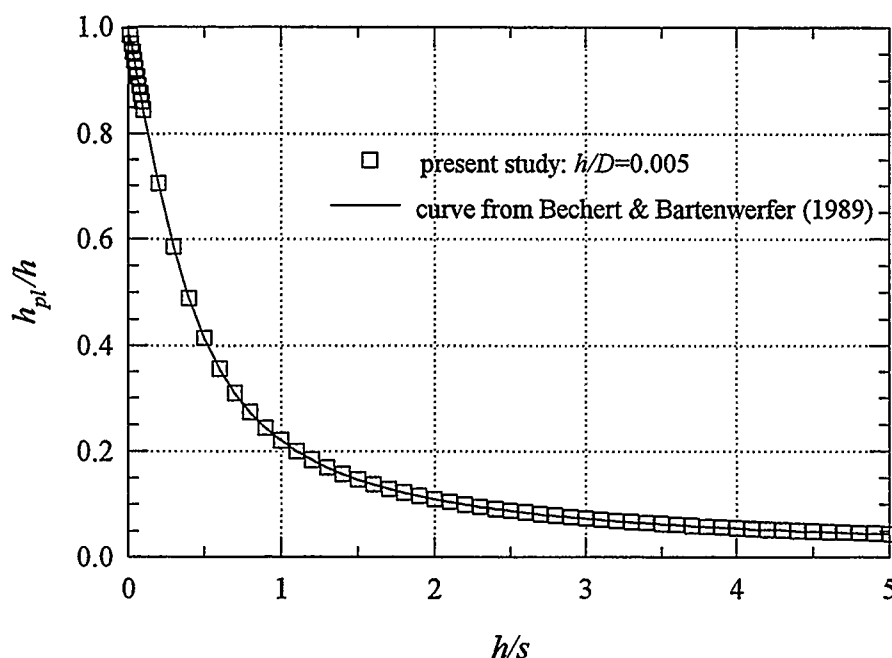


FIGURE 5.3. Longitudinal protrusion height in laminar pipe flow with blade riblets.

5.2 Scaling Parameters for Riblet Drag Reduction

In Section 2.4.1 it was mentioned that aspect ratio h/s is an important parameter which affects the level of drag reduction and the range in which it occurs. This is clearly illustrated in figure 5.4 where direct drag measurements from Bruse *et al.*

(1993)² for blade riblets have been re-plotted using h^+ as the abscissa. Intuitively, it would be expected that riblet height and shape parameters exist which would collapse the self similar data of such a plot onto a single drag reducing curve. Indeed, if the non-dimensional riblet height is scaled with the ratio of longitudinal viscous protrusion height to riblet height, as shown in figure 5.5, a partial collapse is observed with optimum drag reduction occurring at $h^+/(1-h_{pl}/h) \approx 15$. In this figure, additional data for scalloped and triangular riblets from Bruse *et al.* (1993) have also been included. In all cases the longitudinal protrusion height was calculated from expressions given by Bechert & Bartenwerfer (1989). Although the scaling parameter $h^+/(1-h_{pl}/h)$ indirectly includes the riblet shape, it still only provides an optimum drag reducing *height* for a fixed riblet profile. Obviously, an additional scaling parameter for the drag reduction *level* is needed.

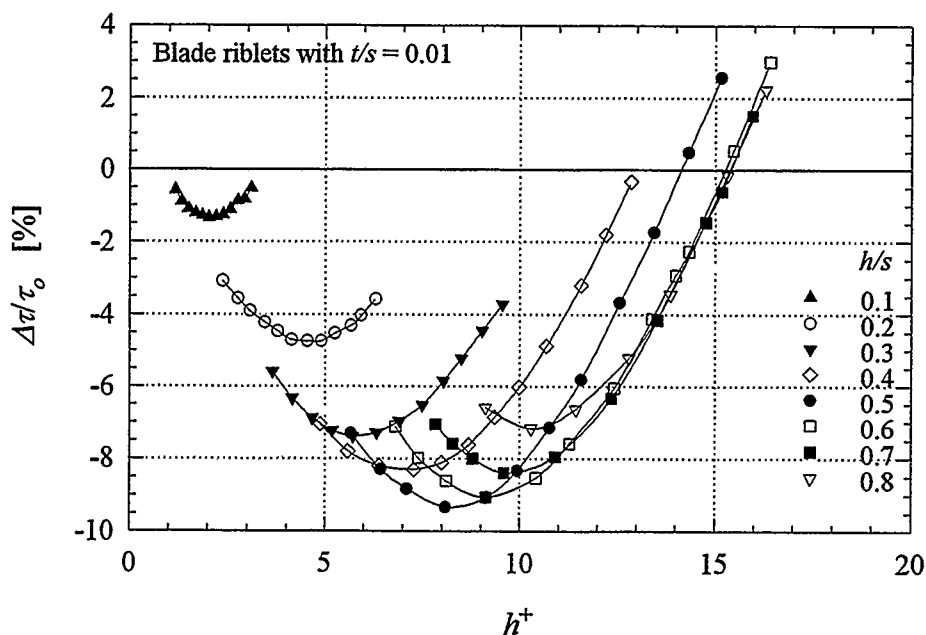


FIGURE 5.4. Effect of aspect ratio on drag reduction (data from Bruse *et al.* 1993).

² The direct drag channel flow measurements from Bruse *et al.* (1993) are used here since they represents the most accurate parametric data available in the literature.

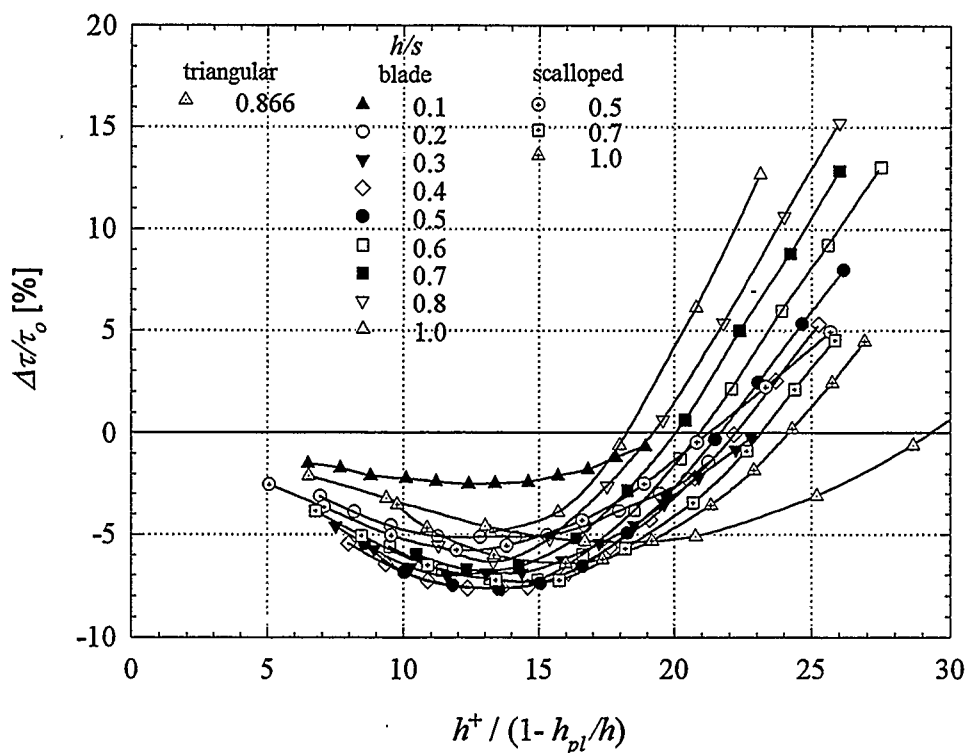


FIGURE 5.5. Scaling of non-dimensional riblet height with ratio of longitudinal protrusion height to riblet height $(1-h_{pl}/h)$ for various riblet shapes.

Bechert *et al.* (1990) have already suggested that drag reduction seems to be proportional to the difference between the longitudinal and cross-flow protrusion heights. Scaling the level of drag reduction in figure 5.5 with the shape factor $(1-h_{pc}/h) / \Delta h/s$ provides a reasonable collapse of the data. This is shown in figure 5.6 where the values of h_{pc}/h and $\Delta h/s$ for the various riblet types were obtained from the plots given in Luchini *et al.* (1991). The scaling parameters presented here were attained by plotting various combinations of viscous protrusion heights versus h/s and choosing factors whose trends matched those observed in the experimental drag reduction data.

For the first time, an almost universal drag reduction curve for riblets has been obtained. Although complete similarity is not achieved, the application of viscous flow protrusion heights as proper scaling parameters for riblet drag reduction certainly suggests that viscous effects do play an important role in the drag reducing mechanism.

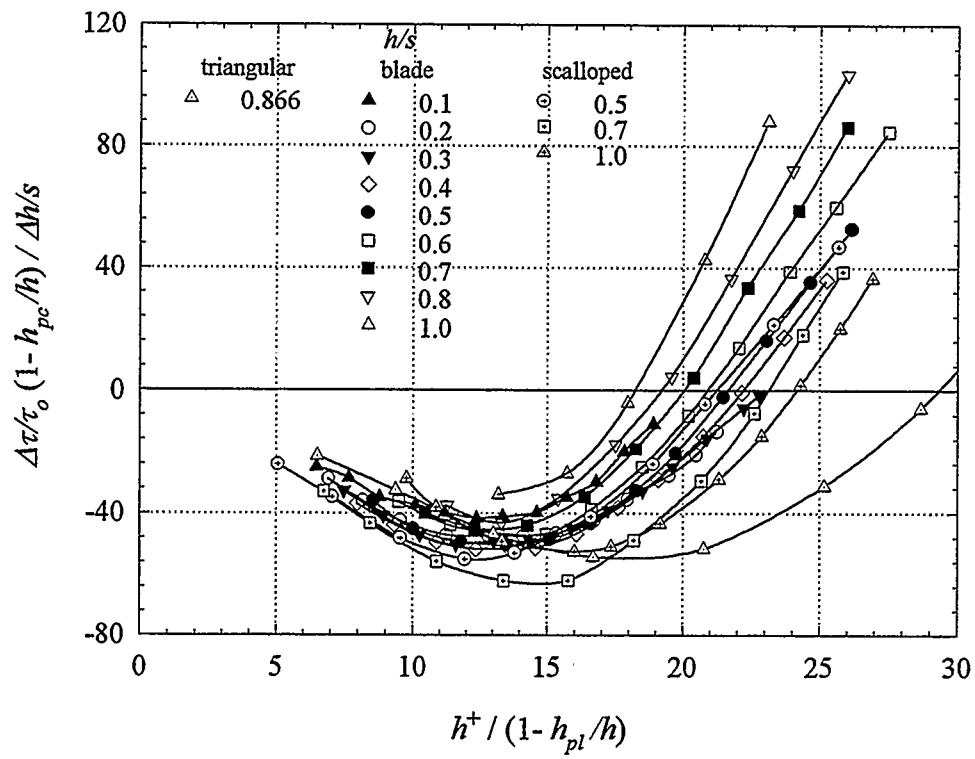


FIGURE 5.6. Scaling of riblet drag reduction with $(1-h_{pc}/h) / \Delta h/s$ for various riblet shapes.

Chapter 6

Drag Reduction Mechanism in a Low Reynolds Number Turbulent Flow

An experimental study comparing turbulence structure over a drag-reducing riblet surface and a smooth pipe wall is presented in this chapter. The measurements were made at a Reynolds number of about 5500, based on the bulk velocity and the mean pipe diameter. Using X-wire anemometry techniques, turbulent statistics as well as detailed radial and azimuthal space-correlations of all three velocity components and turbulent shear stress in the near wall region were obtained. These new measurements provided additional insight into the near-wall dynamical processes which are directly responsible for riblet drag reduction.

6.1 Apparatus and Experimental Techniques

6.1.1 *Test facility*

All experiments were conducted in the open-loop pipe setup shown in figure 6.1, consisting of an adaptable test section, a flow metering section, and a Roots blower. A similar apparatus was used to measure the friction factor in smooth and riblet-lined pipes as described in Chapter 3. Air drawn through the test section from a 1000 m³ laboratory was choked at a single calibrated sonic nozzle, which precisely determined

the mass flow rate ($\pm 0.5\%$) and effectively isolated the test section from any flow or pressure fluctuations induced by the blower.

For this study, several distinct piping arrangements were tested: a smooth reference pipe and two different internally-ribbed pipes. The test section for the smooth reference pipe consisted of a bell-mouth inlet followed by three pieces of aluminum piping with an internal diameter of 95.45 mm and a honed surface finish of better than $R_a = 0.5\ \mu\text{m}$ (relative roughness $\varepsilon/D = 0.000005$). As shown in figure 6.1, the reference pipe section had a combined length of 112 pipe diameters. Concentric alignment between the internal wall surfaces of the three pipe pieces was better than 50 μm , or 0.2 wall units at $Re_b = 5500$. A perforated plate, with 4.5 mm diameter holes on 6.5 mm centers (porosity = 44%), spanned the entire pipe inlet plane immediately following the bell-mouth to promote flow development. Velocity profile measurements taken at cross-sections 21 D , 101 D and 111 D from the inlet indicated that the flow was fully developed at 101 D . Additionally, a linear pressure gradient along the latter portion of the 77 D pipe piece confirmed a fully-developed turbulent flow.

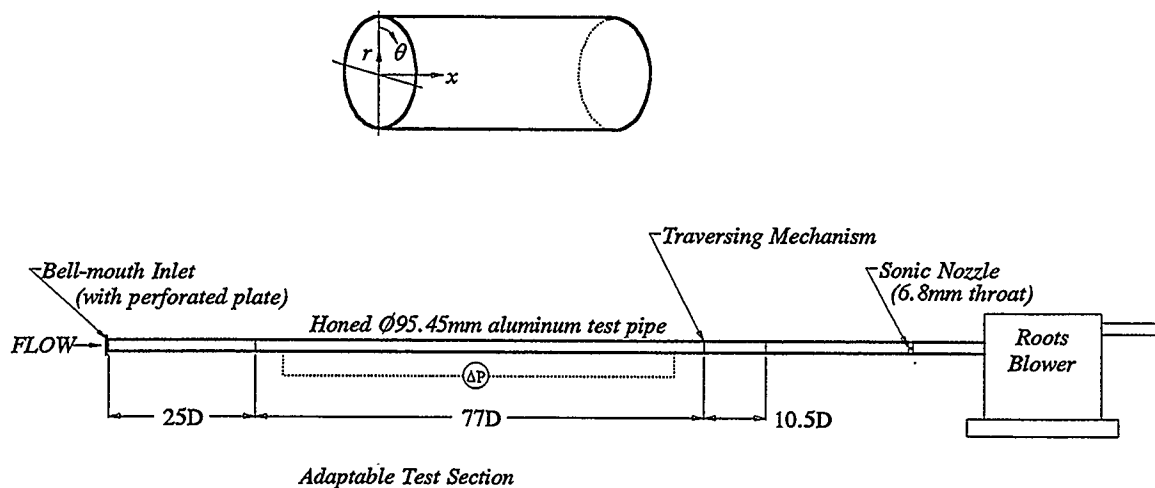


FIGURE 6.1. Open-loop pipe apparatus with adaptable test section.

A pipe identical to the longest smooth reference piece was split in half longitudinally and one half covered with polystyrene blade riblets as shown in figure 6.2(a). This modified pipe was interchanged with the $77 D$ long smooth reference pipe while the inlet and other piping remained the same. The thin blades ($t/s = 0.05$) had height and spacing close to the optimum suggested by Bechert & Bartenwerfer (1989) and were tested at a Reynolds number which gave close to maximum drag reduction. Further details of the blade riblet geometry and flow parameters are found in table 6.1.

An extruded high density polyethylene pipe with an internal scalloped rib profile was also tested. The test section for this configuration consisted of the bell-mouth inlet and perforated plate followed immediately by the 12 m long pipe ($119 D$). Particulars of the pipe and rib geometry are given in table 6.1 while the cross-section is shown schematically in figure 6.2(b). This geometrical configuration was tested at a Reynolds number where little or no drag reduction was expected (drag-neutral surface).

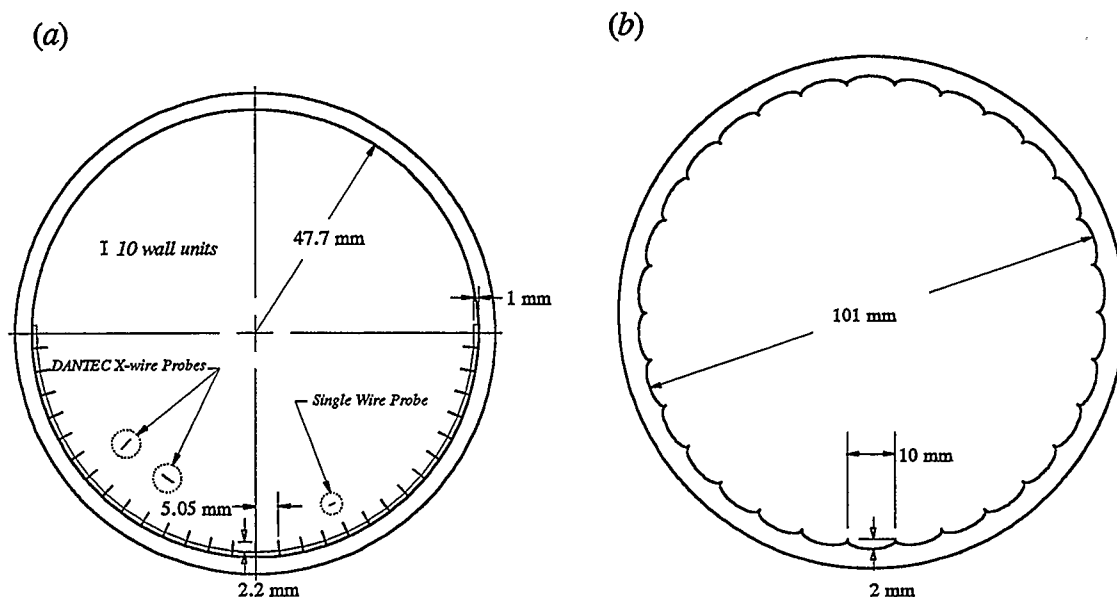


FIGURE 6.2. Cross-sections of riblet pipes: (a) blade ribs covering half of pipe periphery; (b) scalloped ribs.

	Smooth Pipe	Blade Riblets	Scalloped Riblets
Re_b	5500	5500	5100
Re_c	7500	7500	6700
Re_τ	370	380	330
v/u_τ	0.255 mm	0.248 mm	0.306 mm
h/s	—	0.435	0.2
h^+	—	9.0	6.5
s^+	—	20.4	33
h_{pi}/h	—	0.47	0.515
$\Delta h/s$	—	0.12	0.03
t/s	—	0.05	—

TABLE 6.1. Geometry and experimental flow conditions.

6.1.2 Hot-wire anemometry probes

Various single and X-wire probes were used to measure mean and fluctuating velocity in the different pipes. These probes were mounted in a special traversing mechanism which allowed two probes to be independently moved in the radial and azimuthal directions with an accuracy of ± 0.01 mm radially and $\pm 0.25^\circ$ azimuthally. Thus, velocity profiles and radial-azimuthal correlations in a particular pipe cross-section could be measured. For the streamwise velocity profiles and space correlations, modified TSI 1260A-T1.5 single wire probes were used (figure 6.3a). The support needles for these probes were spaced 1.25 mm apart and the 4 μ m diameter platinum coated tungsten sensors had an active length of 1 mm, or only 3-4 viscous wall units, depending on the particular pipe. The profiles and space correlations of the radial and azimuthal velocity components were obtained with two DANTEC 55P51 X-wire probes which could be used in two different end-flow orientations. These probes had 5 μ m

diameter platinum coated tungsten sensors connected between support needles 3 mm apart, with the sensors oriented at 90° to each other, as shown in figure 6.3(b). Gold plating at the ends of each sensor maintained the 1.25 mm long active portion far enough from the support needle tips to minimize aerodynamic interference effects, which can otherwise cause significant errors in shear-stress and fluctuating velocity measurements (Strohl & Comte-Bellot 1973). The separation distance between the individual wires on each probe was 0.9 mm, giving an essentially cubical X-wire probe measurement volume of about 3.5 wall units per side. This dimension was sufficiently small to measure the turbulent shear stress $\overline{u_x u_r}$ (Browne *et al.* 1988), however the measurement of the azimuthal velocity component, particularly in the near wall region, was adversely affected by the mean velocity gradient normal to the pipe wall. A correction applied to the azimuthal measurements is discussed in more detail in §6.1.4.

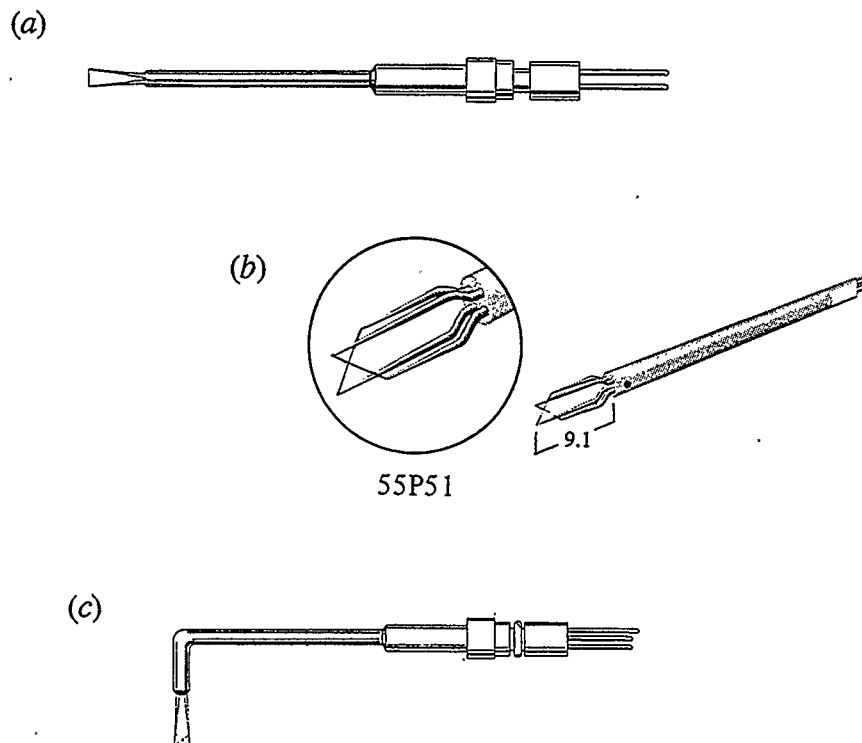


FIGURE 6.3. Hot-wire probes: (a) single wire TSI 1260A-T1.5; (b) DANTEC 55P51 X-wire; (c) TSI 1249A-T1.5 miniature angle X-wire.

In addition, some exploratory measurements directly within the groove of the blade riblets were made using one of the DANTEC 55P51 probes and a TSI 1249A-T1.5 miniature X-wire (figure 6.3c). Since the latter probe with its closely spaced needle supports experienced a significant amount of aerodynamic interference, these exploratory results were somewhat more qualitative. All wires were operated in the constant-temperature mode with an overheat ratio of 1.6 and were corrected for changes in ambient temperature during actual operating conditions.

6.1.3 Probe calibration

The selection of a low Reynolds number flow to study the near wall effects of riblets provides increased spatial resolution at the expense of lower flow velocities. However, even with an overheat ratio of 1.6, buoyancy effects only become important at velocities less than the friction velocity. Calibration of both single and X-wire probes in the end-flow orientation was carried out on the centerline of a laminar pipe flow apparatus capable of accurately developing velocities in the range 0.05-2.0 m/s ($\pm 2\%$). The calibration apparatus consisted of an American DTM-200A bellows type dry test meter to measure the flow rate into a plenum from which the air flow discharged through a 26 mm diameter pipe 120 pipe diameters in length. For the X-wire probes, the directional response was assumed to have the form

$$U_{\text{eff}} = U \sqrt{\cos^2 \phi + k^2 \sin^2 \phi} \quad (6.1)$$

where ϕ is the angle between the velocity vector U and the normal to the wire in the plane of the probe support needles. In (6.1) the velocity component normal to the plane of the needle supports has been neglected since it is not present during calibration. Yaw calibrations performed at several velocities indicated that the yaw coefficient k increased exponentially with decreasing velocity as shown in figure 6.4.

This necessitated an iterative technique to determine the effective cooling velocity U_{eff} for each bridge voltage; the resulting calibration curves were curve-fit with fourth-order polynomials.

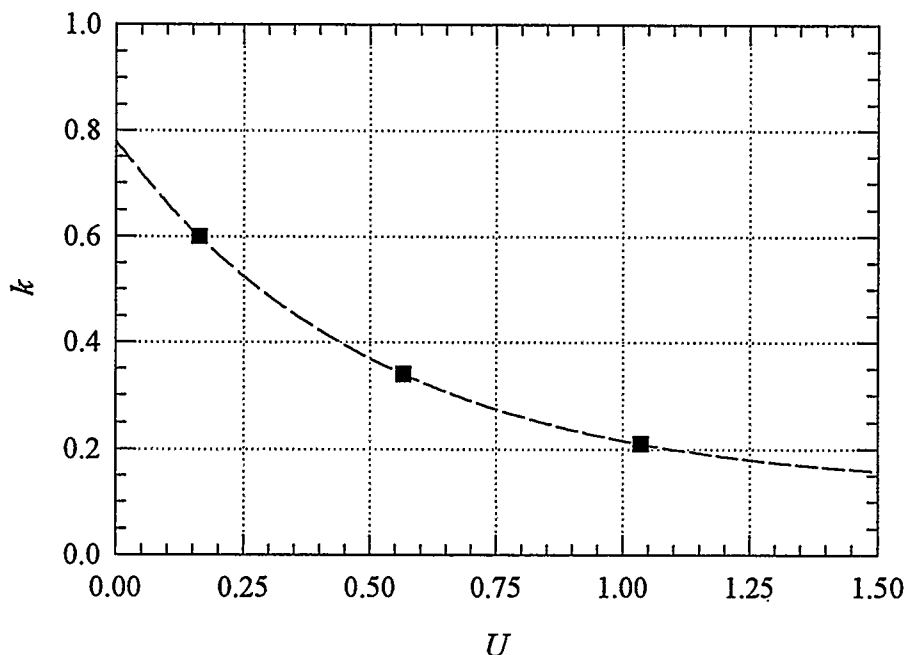


FIGURE 6.4. Variation of yaw coefficient k with velocity for X-wire probes.

6.1.4 Measurement procedures and X-wire signal analysis

Bridge voltage signals from the TSI 150 anemometers were amplified and low-pass filtered (cut-off frequency 400 Hz) using TSI 157 signal conditioners. Simultaneous sampling of each anemometer channel at the rate of 1 kHz was carried out with DC-coupled 12 bit sample-and-hold A/D converters. For every measurement location, sixty records, containing 1024 sample points from each channel, were recorded sequentially and stored. The total sampling duration of about 60 seconds or $15000\tau^*$ (where $\tau^* = \nu/u_r^2$) was sufficient to ensure statistical convergence of ensemble quantities. The accuracy of the measured mean axial velocity ranged from less than 0.5% at the pipe centerline to about 3 % near the wall, while the estimated error for

any of the RMS values was 2-3 %. To obtain the fluctuating velocity components, the average velocity of the entire sixty records (global average), rather than the local average (mean of an individual record), was subtracted from the instantaneous signals. The friction velocity u_τ was determined directly (± 2.5 %) from the pressure drop along the pipe which was measured using a precision micro-manometer.

The use of X-wires to measure instantaneous velocity fluctuations in a highly turbulent three-dimensional velocity field can result in considerable errors, especially if the turbulence is nearly isotropic (Tutu and Chevray 1975). Although large turbulent fluctuations do occur in the near wall region of pipe flow, the turbulence is neither isotropic nor Gaussian—which substantially reduces the errors due to the azimuthal velocity component which result when equation (6.1) is applied to X-wires in a radial plane. Therefore, statistical ensemble averages of shear stress $\overline{u_x u_r}$ and radial velocity fluctuations should be accurate to within a few percent except very close to the wall where the probe spans a substantial mean velocity gradient normal to the wall. However, as mentioned earlier, X-wire measurements in an azimuthal plane close to the wall ($y^+ < 20$) are contaminated since the wire nearer the wall is continuously in a region of lower mean velocity. This results in an inferred velocity vector which is skewed in a direction tangential to the wire experiencing the lower velocity, as shown in figure 6.5. In an attempt to correct the measurements in the azimuthal orientation, the following three-step procedure was applied to ideally find the mean velocity and turbulence intensities at the center of the probe volume: (i) the magnitude and direction of the average velocity vector V for the entire sample was determined by assuming that the effective cooling velocity follows a cosine law behavior, i.e. $k = 0$ in equation (6.1); (ii) next, weighting factors ξ_1 and ξ_2 for the wires were determined using the expressions

$$\frac{\xi_1}{\xi_2} = \tan(\Phi - \psi) \quad (6.2)$$

$$\xi_1 \cdot \xi_2 = 1 \quad (6.3)$$

where Φ is the angle between the second sensor and the probe axis while ψ is the angle between the inferred vector V and the probe axis, in the plane of the probe supports as shown in figure 6.5; (iii) lastly, the entire sample was analyzed again, this time applying the weighting factors to the effective cooling velocities and accounting for the variation of yaw coefficient with velocity. The weighting factors essentially compensate for the mean velocity gradient perpendicular to the planes of the support needles. For statistical quantities, this scheme gave acceptable results and the mean azimuthal velocity was essentially eliminated.

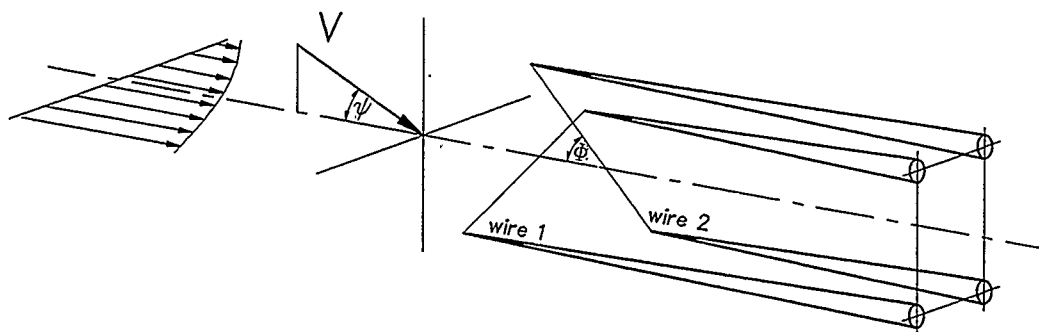


FIGURE 6.5. Inferred velocity vector V resulting from X-wire probe measurement in a mean velocity gradient perpendicular to the planes of the support needles (sensors are oriented at 90° to each other).

6.2 Turbulence Statistics

The measurement of turbulence statistics not only aids in the characterization of a particular flow, but can also increase the confidence in an experimental method when agreement with other measurement techniques is obtained. For a low Reynolds number turbulent pipe flow, a detailed comparison between the hot-wire technique of the present study, LDA, particle image velocimetry (PIV), and direct numerical simulation (DNS) was carried out by Eggels *et al.* (1993). Excellent agreement between the various experimental methods demonstrated that the measurement techniques outlined in Section 6.1 should provide reliable data when applied to the study of the near-wall flow over a riblet surface.

An examination of various velocity and shear stress statistics measured in the smooth pipe, the half-covered blade riblet pipe, and the scalloped-rib plastic pipe follows. The scalloped-rib data followed trends similar to, but less pronounced than, the blade riblet measurements, and are only referred to when illustrating a particular point. Measurements over the smooth half of the blade riblet pipe are not included here since they were essentially the same as those for the completely smooth pipe. The only published data of turbulence statistics for pipe flow over riblets are the streamwise velocity and intensity measurements of Nitschke (1983). Thus, where appropriate, published boundary layer or channel flow data are compared with the present results.

6.2.1 *Mean velocity profiles and turbulence intensities*

The mean streamwise velocity profiles normalized with centerline velocity for the smooth pipe, the blade riblet pipe, and the scalloped-rib pipe are shown in figure 6.6, along with the smooth pipe profile from DNS (Eggels *et al.* 1993). Very low velocity fluid within the blade ribs is quite evident, while the azimuthal variation of the mean

velocity is restricted to a region within two riblet heights above the rib valley. These findings are consistent with the three-dimensional particle tracking velocimetry (3-D PTV) measurements for tapered rectangular riblets in a channel flow by Suzuki & Kasagi (1993) and the hot-wire data of Vukoslavcevic *et al.* (1987) within triangular riblets of a boundary layer flow.

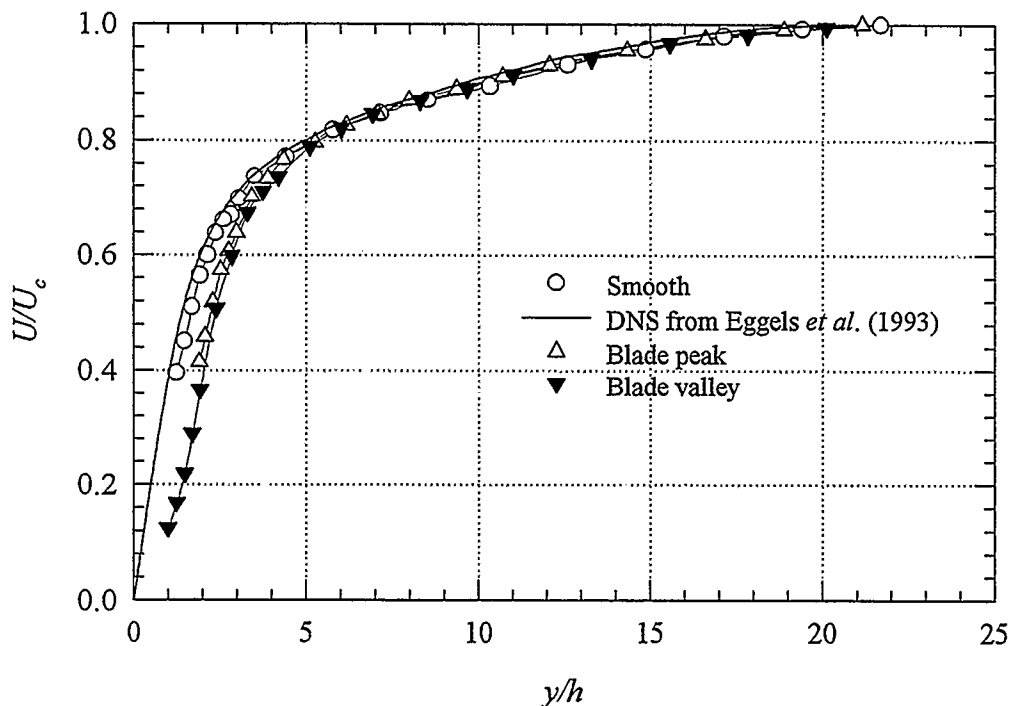


FIGURE 6.6. Mean streamwise velocity above smooth and blade riblet surfaces normalized with the pipe centerline velocity U_c .

Figure 6.7 is a plot of the mean streamwise velocity in non-dimensional wall coordinates for the smooth, blade riblet, and scalloped-rib surfaces; the friction velocity based on the average wall shear stress for each surface is used for normalization. An upward shift in the outer region is evident with the surface producing the most drag-reduction (blade ribs) exhibiting the largest shift. This is the same result found in polymer drag-reducing flows (Virk 1975) and is not entirely unexpected since it is a well-known fundamental principle that flow over rough surfaces with increased drag exhibits a *downward* shift of the velocity profile in the outer region (Schlichting 1975).

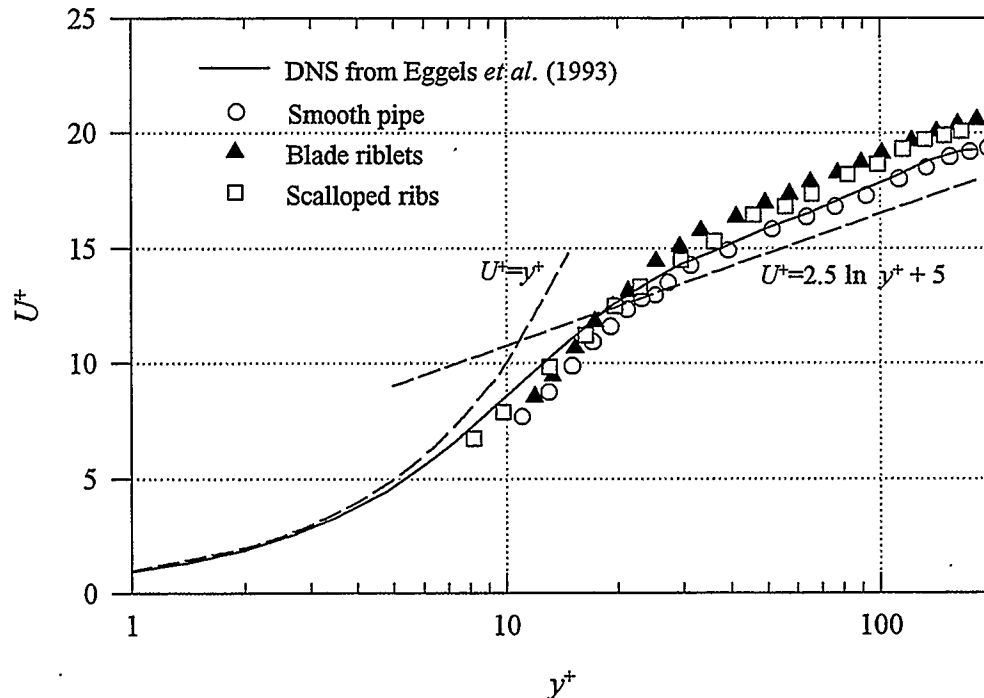


FIGURE 6.7. Streamwise velocity over smooth and riblet surfaces in local wall units.

In the useful comparison of turbulence intensity profiles above smooth and riblet surfaces, a difficulty arises in the choice of the velocity scaling parameter. A comparison of boundary layer flows over a smooth plate (Klebanoff 1954) and rough surface (Corrsin & Kistler 1954) has shown that the friction velocity is the proper scaling velocity for the turbulence intensity of all three velocity components. However, previous riblet studies have used either outer variables (i.e. free-stream or center-line velocity) or the friction velocity of the smooth surface as the velocity scaling parameter. If the turbulence intensity is scaled with the center-line velocity, as in figure 6.8, a reduction for all three components is observed. The largest reduction is in the streamwise intensity which agrees with the results of Suzuki & Kasagi (1993) among others. For a pipe flow over riblets with rounded peaks, Nitschke (1983) also found reductions in the streamwise intensity. Clearly, if the data in figure 6.8 were normalized with the average local friction velocity, the observed reductions would be substantially lower and the smooth and riblet profiles would nearly coincide.

Unfortunately, the degree of error associated with the measurement of the friction velocity ($\pm 2.5\%$) in this study does not allow an unambiguous confirmation of such a scaling phenomena, although there is strong evidence to suggest that the turbulence intensity does scale with the average wall shear stress. However, such a generalization is met with conflicting evidence; Suzuki & Kasagi (1993) found that with *drag-increasing* riblet flows the streamwise intensity is even further reduced while the spanwise and radial intensities are increased, and in polymer drag-reducing flows a large increase in streamwise intensity is observed (Virk 1975). Such contrasting observations clearly indicate that a drag reduction mechanism cannot be inferred from statistical measurements alone. Further insight can be gained by using the local mean velocity as the scaling parameter, as shown in figure 6.9. The smooth wall data agree very well with recent detailed LDA measurements in pipe flow by Durst *et al.* (1993). Over the valley of the blade riblets, large reductions in the streamwise intensity relative to the local mean are accompanied by increases in the radial intensity. Relative to the local mean velocity the azimuthal intensity remains unchanged.

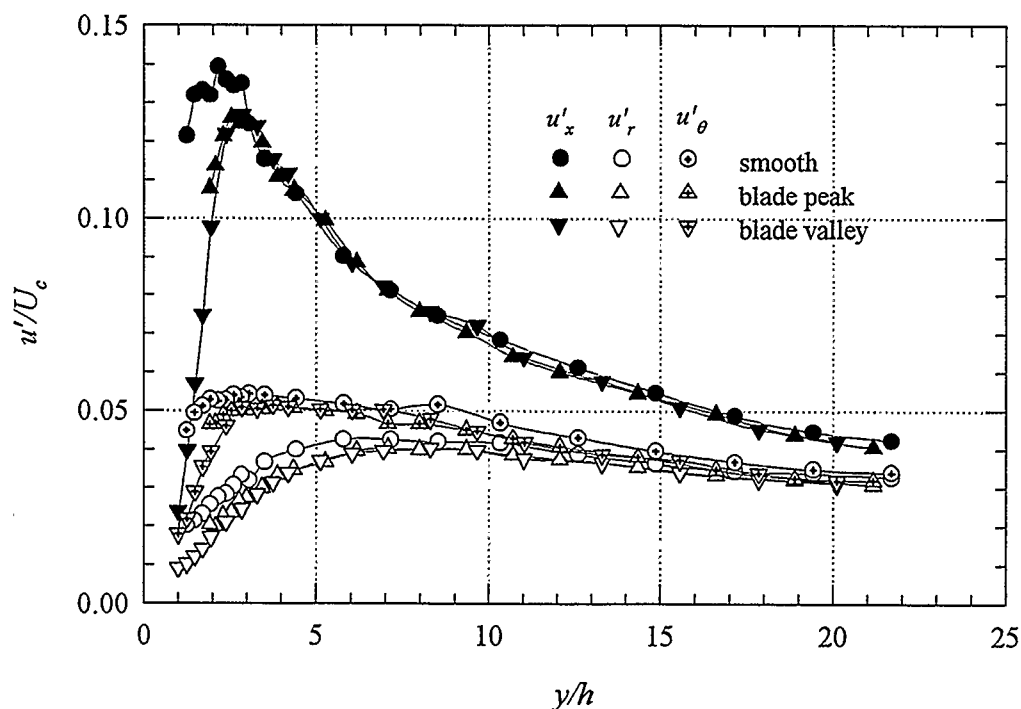


FIGURE 6.8. Turbulence intensities over smooth and blade riblet surfaces.

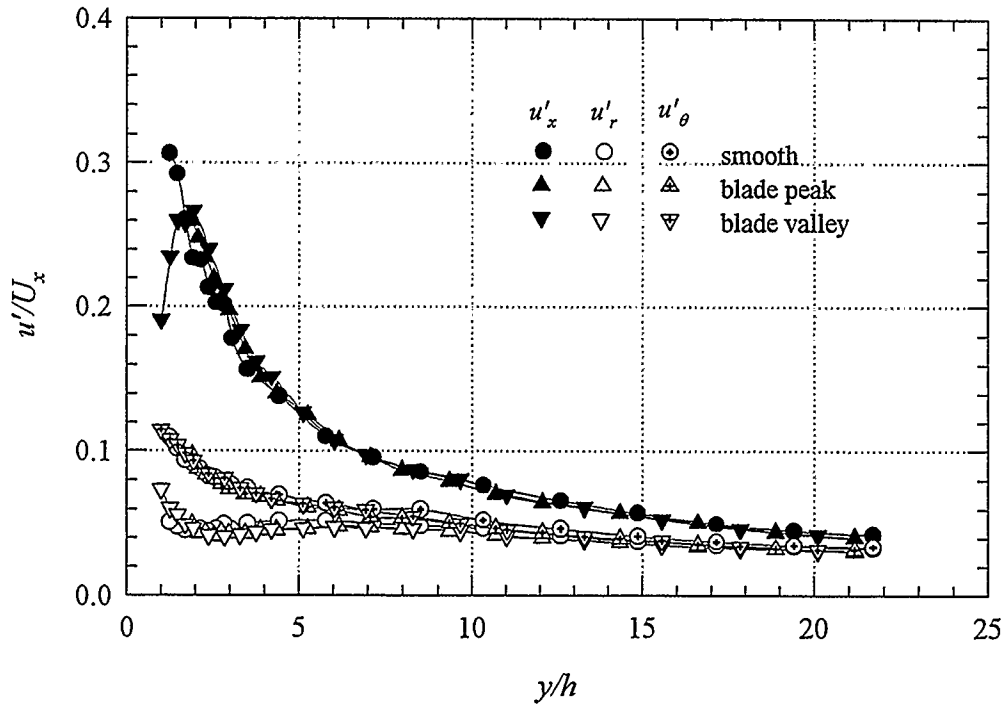


FIGURE 6.9. Turbulence intensities over smooth and blade riblet surfaces normalized with the local mean streamwise velocity.

6.2.2 Reynolds stresses

Suzuki & Kasagi (1993) have compared the diagonal components of the stress anisotropy tensor b_{ij}

$$b_{ij} = \overline{u_i u_j} / \overline{u_i u_i} - \delta_{ij} / 3 \quad i, j = 1, 2, 3 \quad (6.4)$$

where the indices 1, 2 and 3 correspond to the streamwise, normal (or radial), and spanwise (or azimuthal) directions. Their results indicated that very close to the riblet surface, particularly over the valley, the inter-component transfer of kinetic energy from the streamwise to the spanwise component is apparently impeded. They believe that this phenomena is one of the key mechanisms for riblet drag reduction. However, the same trend was observed with riblets which increased the drag. The diagonal components of the stress anisotropy tensor for the pipe flow of the present study are plotted in figure 6.10. These results indicate an opposite trend in the near-wall region;

the kinetic energy transfer becoming more efficient, although, in the buffer region, a reduced inter-component energy transfer is indeed observed. The current results would indicate that cross-stream and radial mixing is enhanced within the riblet valleys but decreased in the region above the ribs.

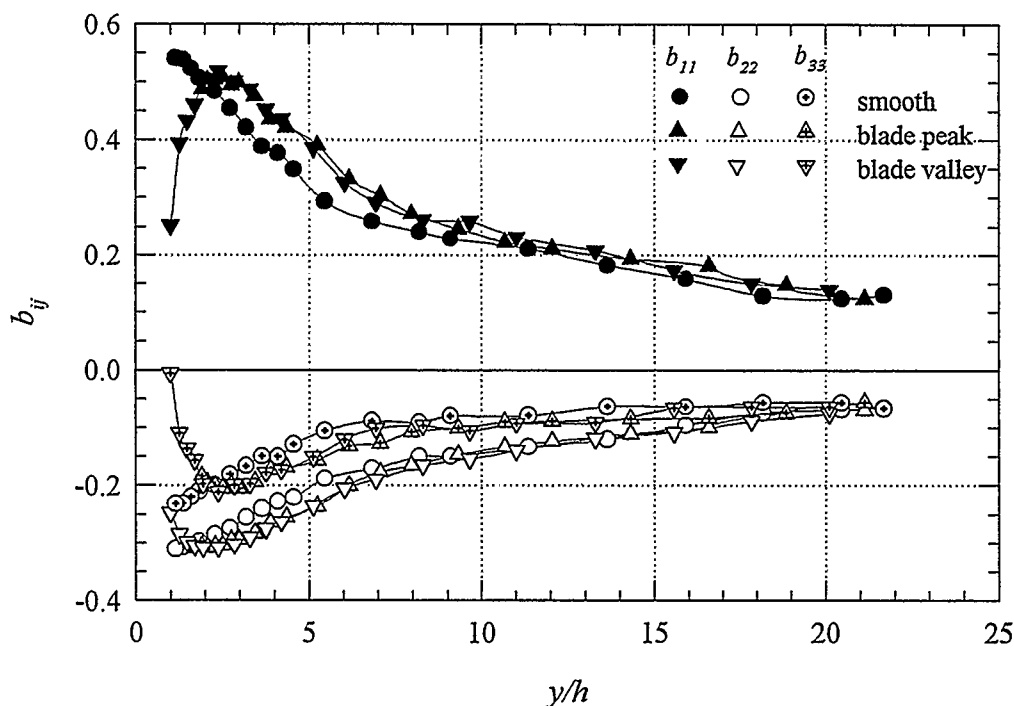


FIGURE 6.10. Diagonal components of the stress anisotropy tensor b_{ij} over smooth and blade riblet surfaces.

The distributions of Reynolds shear stress $\overline{u_x u_r}$ normalized on center-line velocity are plotted in figure 6.11. It is quite evident that a decrease is measured over the riblet surfaces indicating that both riblet surfaces indeed reduce drag. Very low levels of momentum exchange occur near all surfaces. However, if the turbulent shear stress is normalized with the local velocity, as shown in figure 6.12, the unexpected result is that, relative to the local velocity, the momentum exchange is quite large especially over the rib valley. This finding suggests that secondary motions not present in smooth wall flows are produced by the riblets. The skewness and flatness factors of the Reynolds shear stress $u_x u_r$ are plotted in figure 6.13(a, b). Higher levels of skewness

and flatness are observed over both the rib peaks and the valleys which indicates that the frequency of high shear stress producing events is decreased.

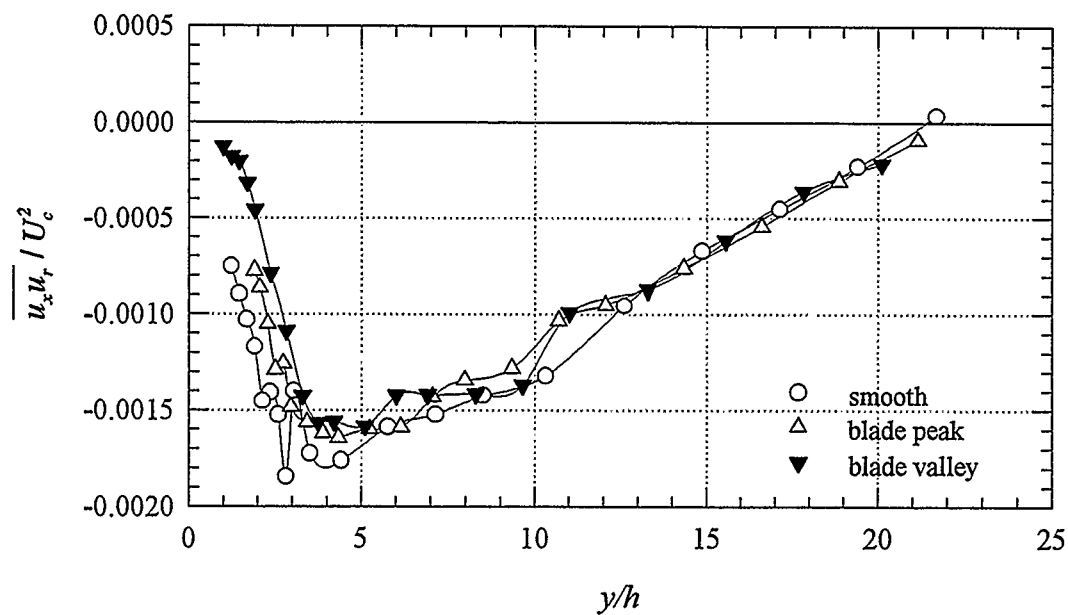


FIGURE 6.11. Comparison of Reynolds shear stress over smooth and blade riblet surfaces normalized with centerline velocity U_c^2 .

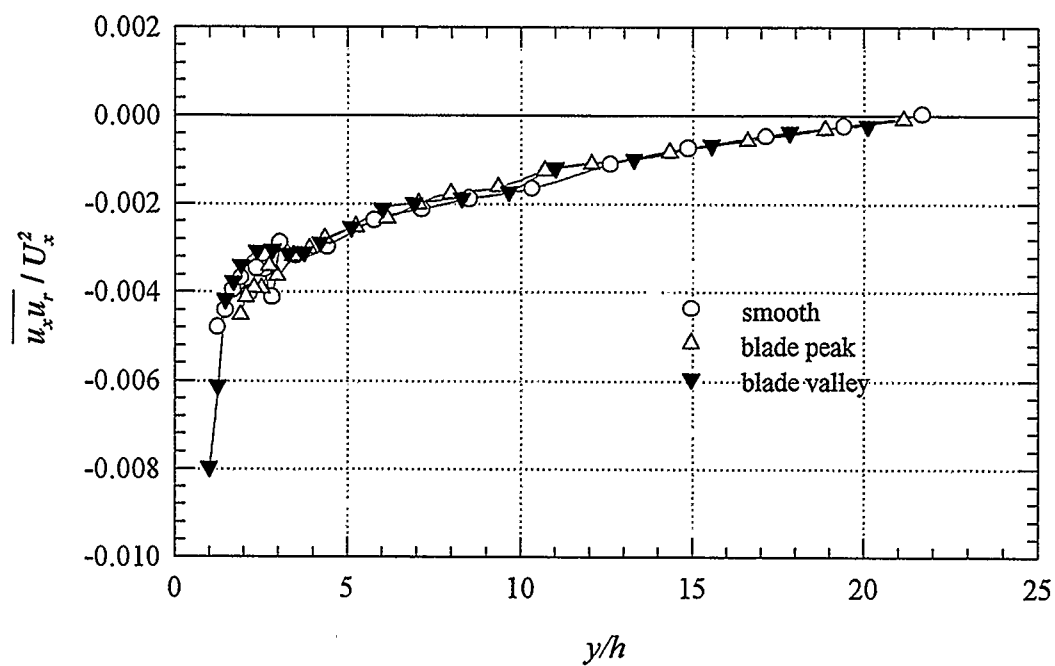


FIGURE 6.12. Reynolds shear stress above smooth and blade riblet surfaces normalized with the local mean streamwise velocity U_x^2 .

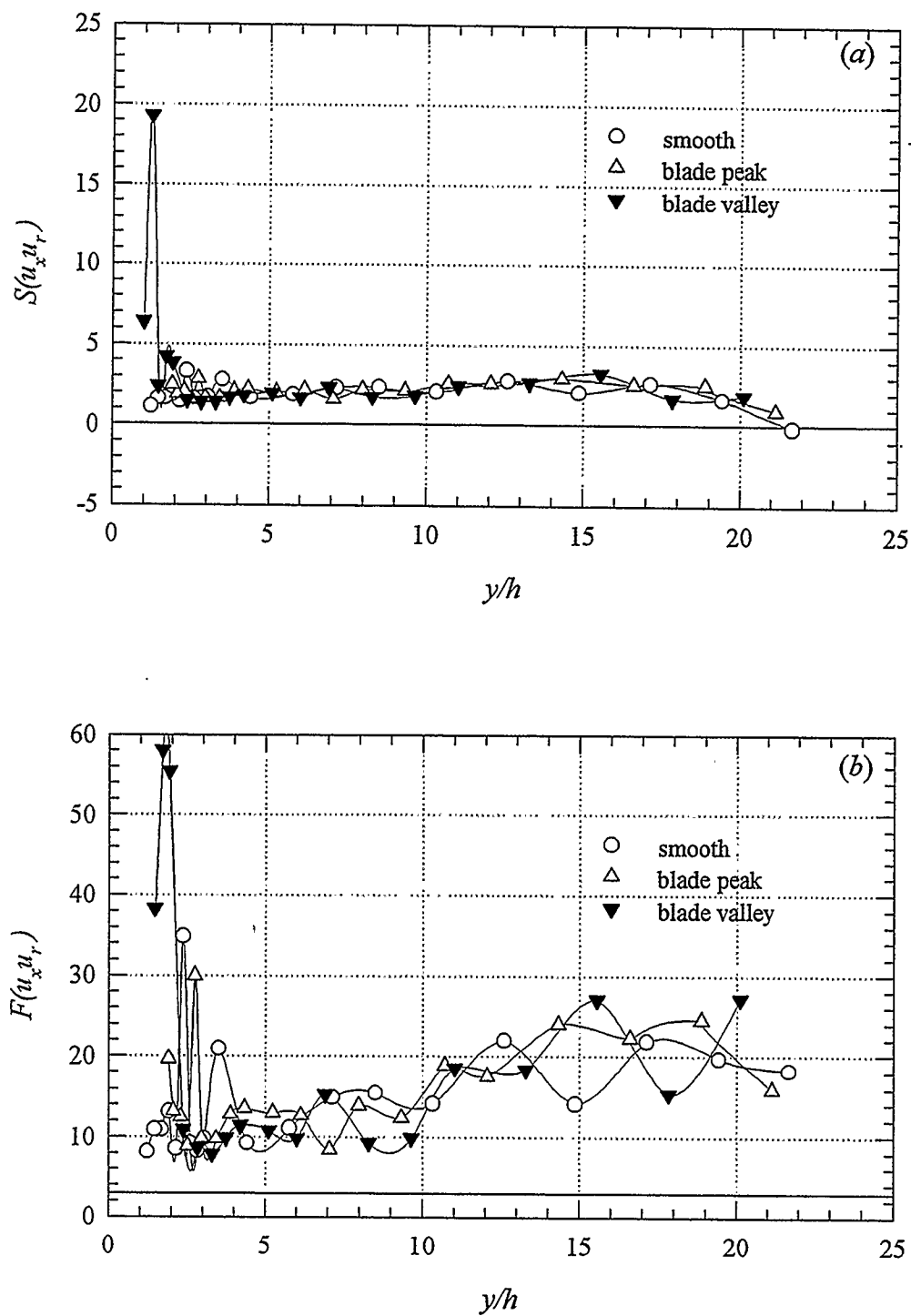


FIGURE. 6.13. Skewness and flatness factors of Reynolds shear stress over smooth and blade riblet surfaces: (a) $S(u_x u_r)$; (b) $F(u_x u_r)$.

6.2.3 Higher-order statistics and triple correlations

Perhaps the most insightful observations from point-statistics arise in the comparison of higher-order moments of the fluctuating velocity components. In general, the third moment of a fluctuating quantity, or *skewness factor*, is defined as

$$S(u) = \frac{\overline{u^3}}{u'^3} \quad (6.5)$$

and the fourth moment, or *flatness factor*, is

$$F(u) = \frac{\overline{u^4}}{u'^4} \quad (6.6)$$

The skewness $S(u_x)$ and flatness $F(u_x)$ factors of the streamwise velocity are shown in Figure 6.14(a, b) where the combination of large positive skewness and flatness near the wall indicates that the most probable streamwise velocity is less than the mean, with occasional large positive velocity fluctuations, respectively. Compared with the smooth wall, an increase in both the skewness and flatness factor is observed over the rib valley while over the rib peak both are reduced. Thus, large positive streamwise fluctuations occur less frequently but with higher velocity above the riblet valley whereas flow over the rib peak becomes more Gaussian. Vukoslavcevic *et al.* (1987) measured the identical trends over triangular ribs while, on the other hand, the DNS by Chu & Karniadakis (1993) of a channel flow with one smooth wall and the other covered with triangular riblets did not produce any of these trends. Incidentally, the streamwise higher-order statistics over the smooth wall portion of the DNS by Chu & Karniadakis (1993), in particular the flatness factor, do not agree well with experiments nor with the smooth channel flow DNS results of Kim, Moin & Moser (1987). These discrepancies can be attributed to insufficient grid resolution in the streamwise direction of the DNS by Chu & Karniadakis (1993).

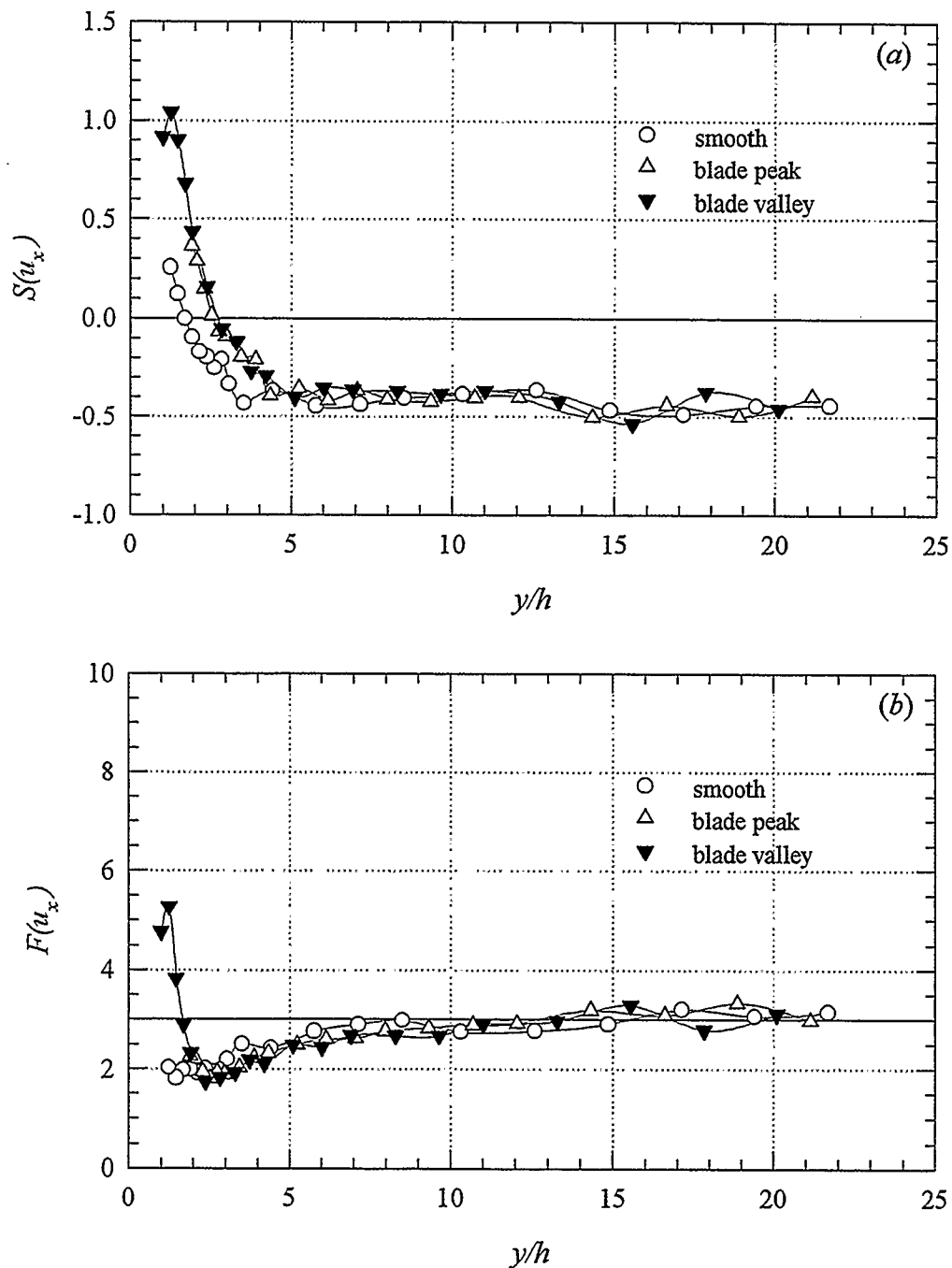


FIGURE 6.14. Skewness and flatness factors of streamwise velocity over smooth and blade riblet surfaces: (a) $S(u_x)$; (b) $F(u_x)$.

The most significant difference between flow over a smooth wall and a riblet surface is found in the skewness of the radial velocity. Figure 6.15(a) indicates quite clearly that the radial skewness factor becomes strongly negative over the riblet valley

whereas over the rib peak it is strongly positive. Here the direction of radial velocity is considered positive away from the wall. The measurements of Pulles (1988) indicate a similar but considerably less pronounced trend while the DNS of Chu & Karniadakis (1993) appears to capture this feature as well.

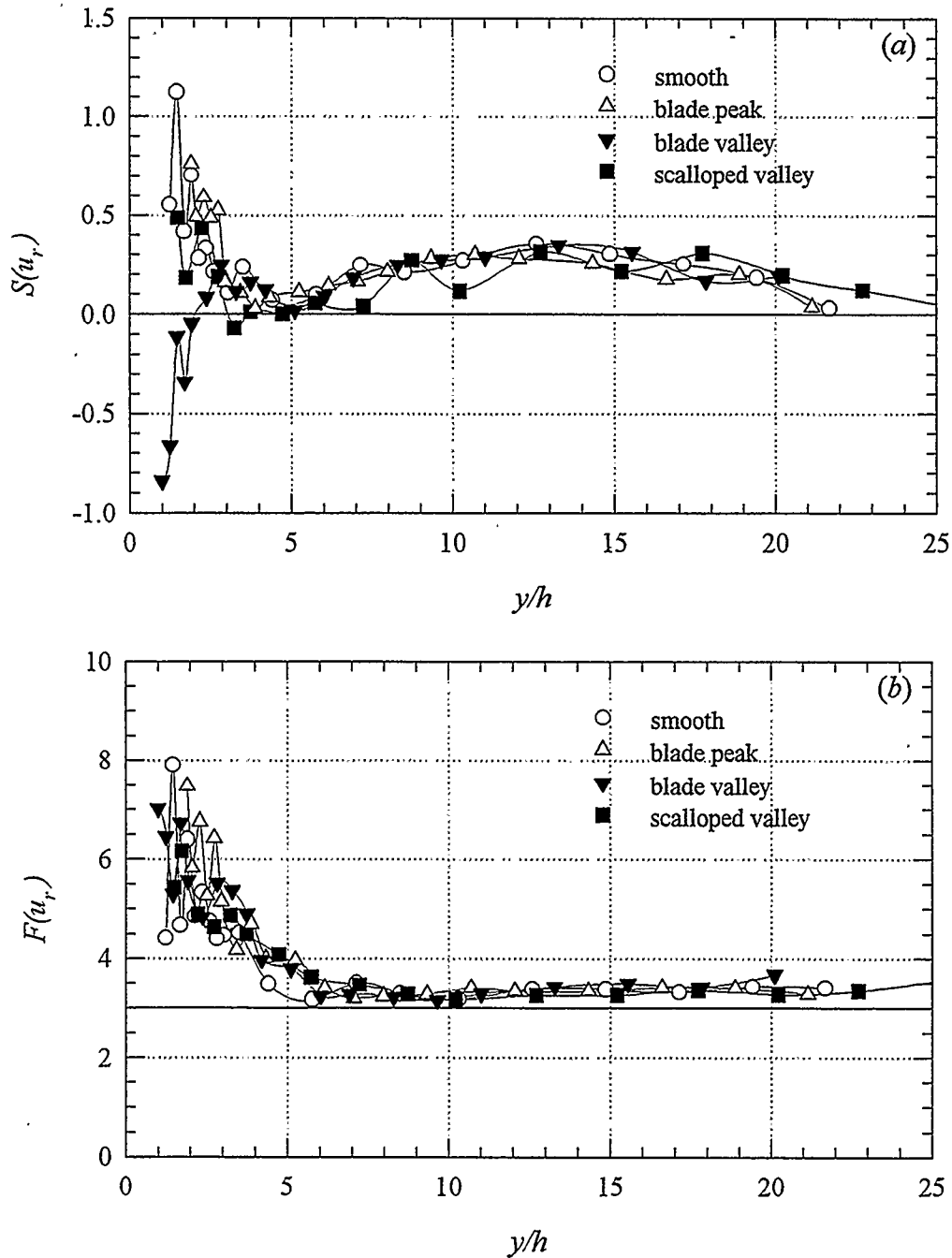


FIGURE 6.15. Skewness and flatness factors of radial velocity over smooth, blade riblet and scalloped riblet surfaces: (a) $S(u_r)$; (b) $F(u_r)$.

The significance of the reversed skewness over the riblet valley is that sweeps of radial velocity towards the wall occur less frequently than over a smooth surface. In addition, it suggests a decoupling of the radial fluctuations between the rib valley and tip, indicating a weakening of turbulent shear stress producing events which then leads to drag reduction. Note that for the scalloped-rib pipe, which exhibits very little drag reduction, only a slight reduction in skewness over the valley region is observed, providing further support to the notion that the reversed skewness may be a key to the mechanism primarily responsible for the observed drag reduction. More details of this phenomena will be discussed in Section 6.3 and Section 6.4. The profiles of radial flatness factor are plotted in figure 6.15(b) where only a slight increase over the riblet surfaces is observed.

Skewness and flatness factors for the azimuthal velocity are shown in figure 6.16(a, b). Almost negligible differences are found except for the regions over the rib valley where the flatness is increased substantially, indicating that the riblets reduce the number of large azimuthal fluctuations. The large skewness factor over the blade-rib valley is due to measurement error, clearly demonstrating the limited ability of the X-wire to resolve the velocity vector in a region of substantial streamwise velocity gradient normal to the wall.

Lastly, plots of shear-stress flux due to radial and streamwise velocity fluctuations $\overline{u_x u_r^2} / \overline{u_x' u_r'^2}$ and $\overline{u_x^2 u_r} / \overline{u_x'^2 u_r'}$ respectively, are shown in figure 6.17(a, b). Differences in both quantities above the riblet valley are evident indicating a modification of the momentum transport over the riblet surface. Plots of $\overline{u_x u_\theta^2} / \overline{u_x' u_\theta'^2}$ and $\overline{u_x^2 u_\theta} / \overline{u_x'^2 u_\theta'}$ are given in figure 6.18(a, b). Again, only over the riblet valley are differences observed.

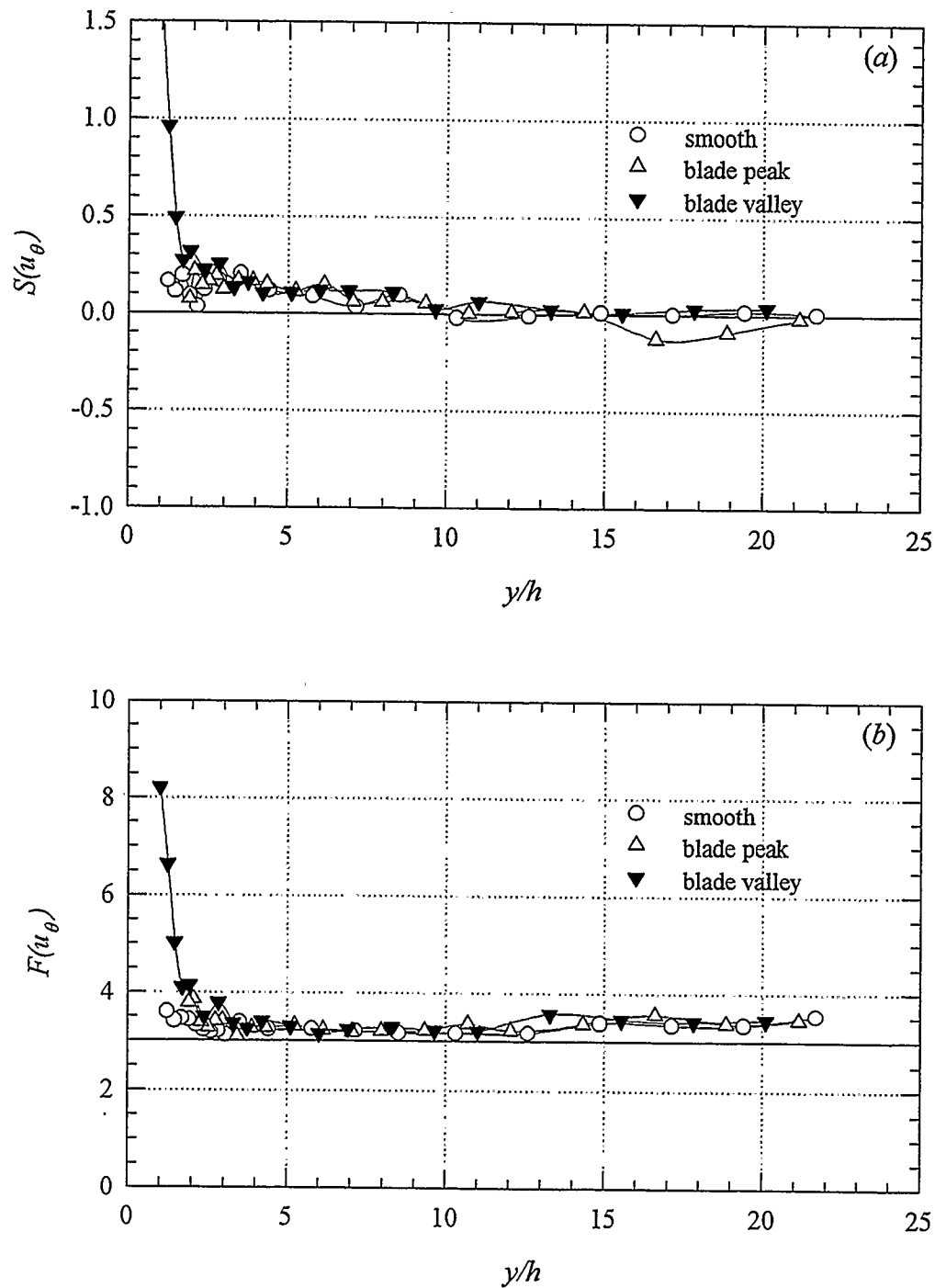


FIGURE 6.16. Skewness and flatness factors of azimuthal velocity over smooth and blade riblet surfaces: (a) $S(u_\theta)$; (b) $F(u_\theta)$.

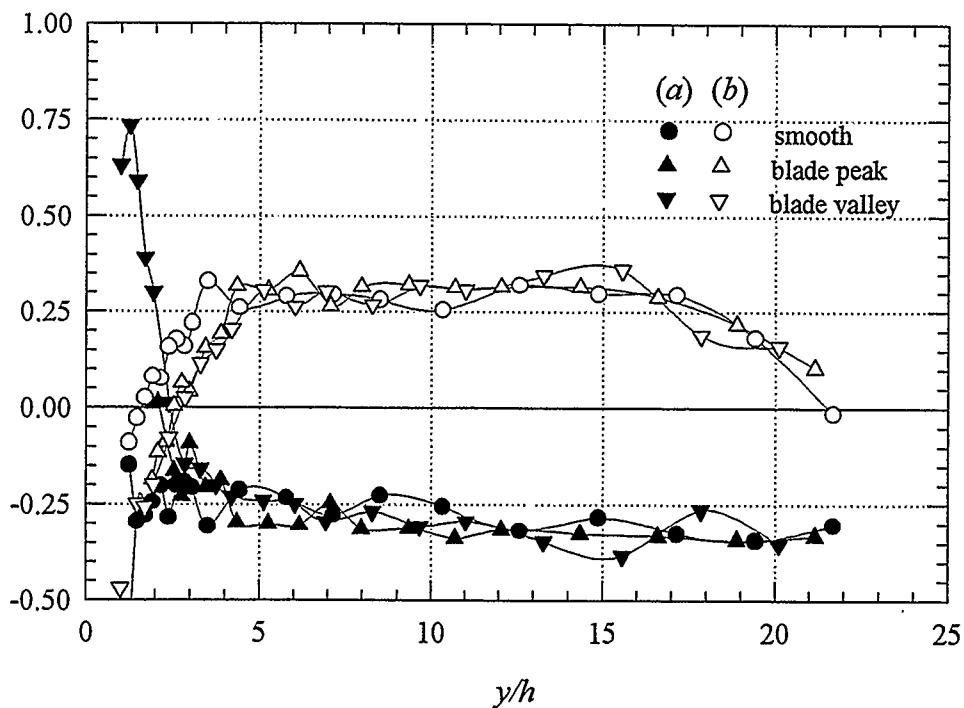


FIGURE 6.17. Shear stress flux due to radial and streamwise velocity fluctuations over smooth and blade riblet surfaces: (a) $\overline{u_x u_r} / \overline{u'_x u'_r}$; (b) $\overline{u_r^2 u_r} / \overline{u_x^2 u'_r}$.

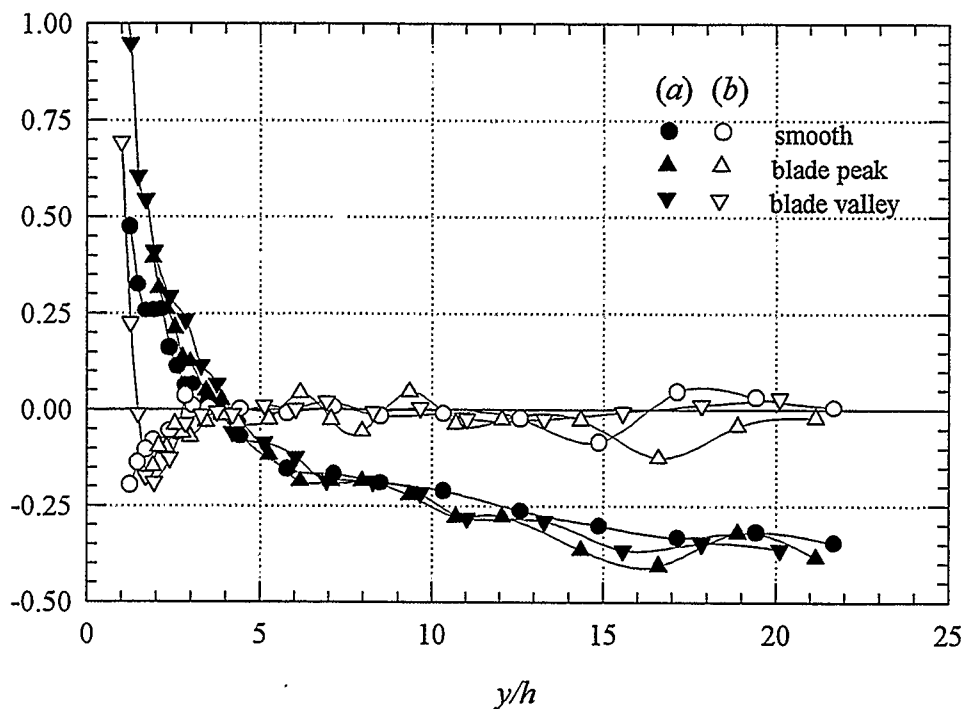


FIGURE 6.18. Shear stress flux due to azimuthal and streamwise velocity fluctuations over smooth and blade riblet surfaces: (a) $\overline{u_x u_\theta} / \overline{u'_x u'_\theta}$; (b) $\overline{u_x^2 u_\theta} / \overline{u_x^2 u'_\theta}$.

6.3 Turbulence Structure

Certain details of the turbulent flow structure can be obtained from space and time correlations, however care must be exercised in drawing any sweeping mechanistic conclusions from the statistics. Correlations are perhaps better used to characterize turbulence structures which have been previously identified from flow visualization studies as well as interrogation of databases generated by DNS. This section documents the radial and azimuthal two-point space correlations obtained within a cross-sectional plane of the pipe using conventional hot-wire anemometry techniques. An in-depth consideration of the relationship between the measured correlations and near-wall dynamics will be dealt with in Section 6.4.

Owing to physical limitations of the probe holders and X-wire support needles, the smallest spatial separation which could be achieved for either the radial or azimuthal correlations was about 10 wall units. To determine the reliability of the hot-wire techniques, radial and azimuthal correlations of streamwise velocity measured with two single-wire probes were compared to those obtained using two X-wire probes. Excellent agreement was found for all cases reported in this study. Where possible, comparisons with relevant published data have been made. Unfortunately, no experimental space correlations for the radial and azimuthal velocity components in pipe flow exist in the literature.

6.3.1 Radial correlations

The general two-point radial correlation function R_{uu} is defined as

$$R_{uu}(r_1, r_2) = \frac{\overline{u(r_1)u(r_2)}}{u'(r_1)u'(r_2)} \quad (6.7)$$

and is measured by fixing one of the probes at the radial position r_1 while radially traversing the other probe (position r_2).

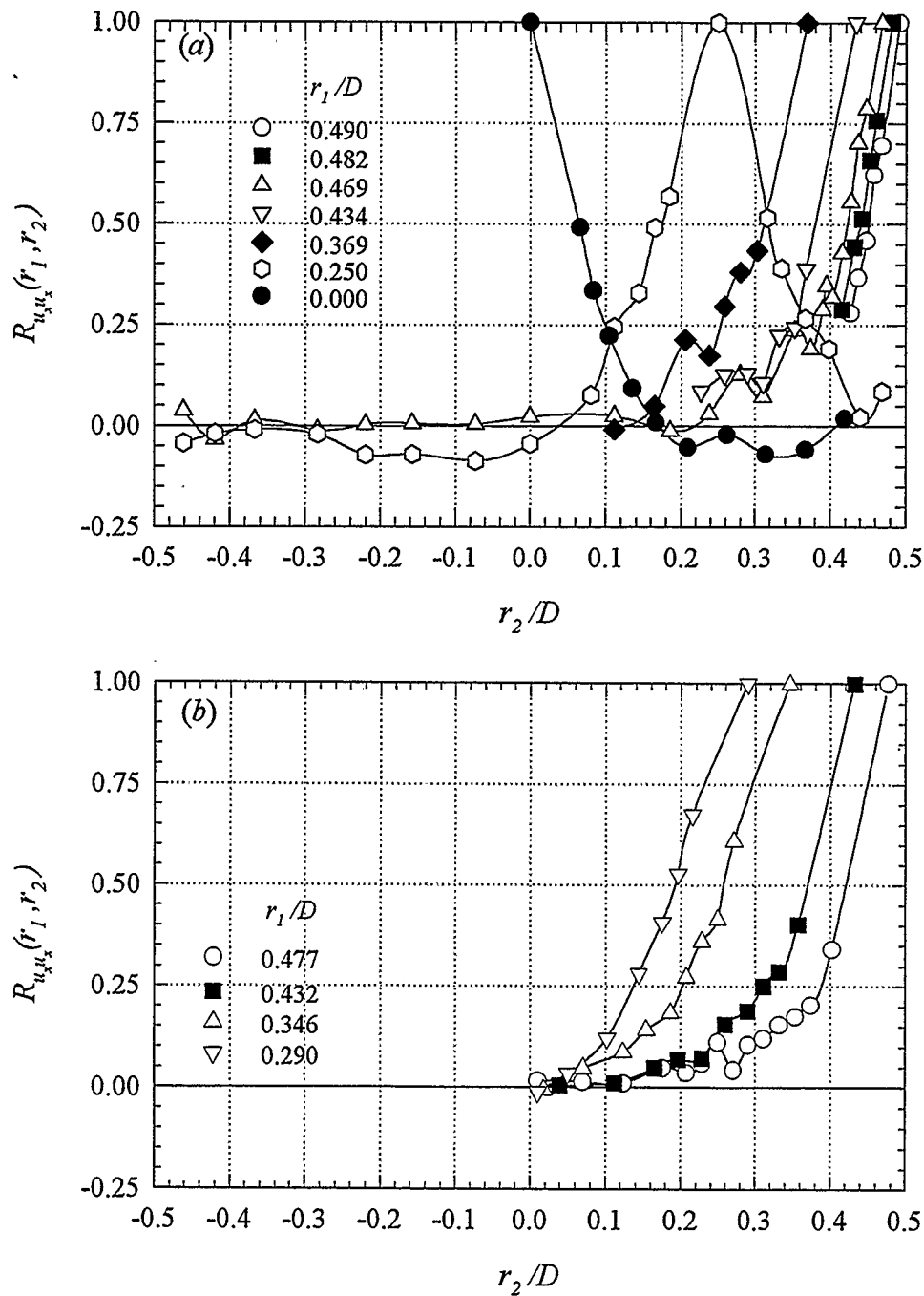


FIGURE 6.19. Two-point radial correlations of streamwise velocity $R_{u_x}(r_1, r_2)$:
(a) smooth surface ; (b) blade riblet surface.

Radial correlations of streamwise fluctuating velocity over the smooth pipe surface are shown in figure 6.19(a). It is evident that the radial correlation length, outward from the wall, becomes narrower for flow nearer the wall. The only low Reynolds

number pipe flow data available for comparison are the PIV results of Westerweel *et al.* (1993), which show consistently wider correlation lengths across the pipe. This discrepancy is likely due to the relatively small statistical sample size of the PIV measurements which were intended to focus on instantaneous turbulence structure rather than statistics. A plot of radial correlations over the blade riblet surface is given in figure 6.19(b). Only slight differences can be observed although the correlation length close to the riblet surface is somewhat less than over the smooth surface. However, if the data are plotted in wall units, based on the average friction velocity, significantly narrower correlations over the blade riblet surface are observed.

Some interesting trends from the radial correlations of fluctuating radial velocity were found. The smooth pipe correlations (figure 6.20a) indicate extremely narrow radial correlation distances in the region very near the wall. For the three reference positions of r_1 closest to the wall, the probe located at r_2 was about 8 wall units downstream of the fixed reference probe. If the near wall region contains numerous vortical structures with a significant azimuthal (spanwise) component of concentrated vorticity, this would explain the fairly strong negative correlation which is observed. Over the blade riblets, figure 6.20(b), the correlation distance is narrower yet with even stronger negative correlations. In the region further from the wall the correlation distances become large, even exceeding the radial correlation length of the streamwise velocity and there is little or no noticeable effect of the riblet surface.

Due to physical limitations of the probe holders, spatial separation distances of less than 25 wall units could not be achieved for the correlations of azimuthal velocity. With the reference probe quite close to the wall the azimuthal velocity is apparently only correlated over a very short radial distance followed by a wider range of weaker negative correlation as shown in figure 6.21. A similar trend is observed for the blade riblets. For these measurements, both probes were located at the same axial position.

The restricted radial distance of azimuthal velocity correlation would suggest that vortical structures with a significant streamwise vorticity component exist in the buffer region.

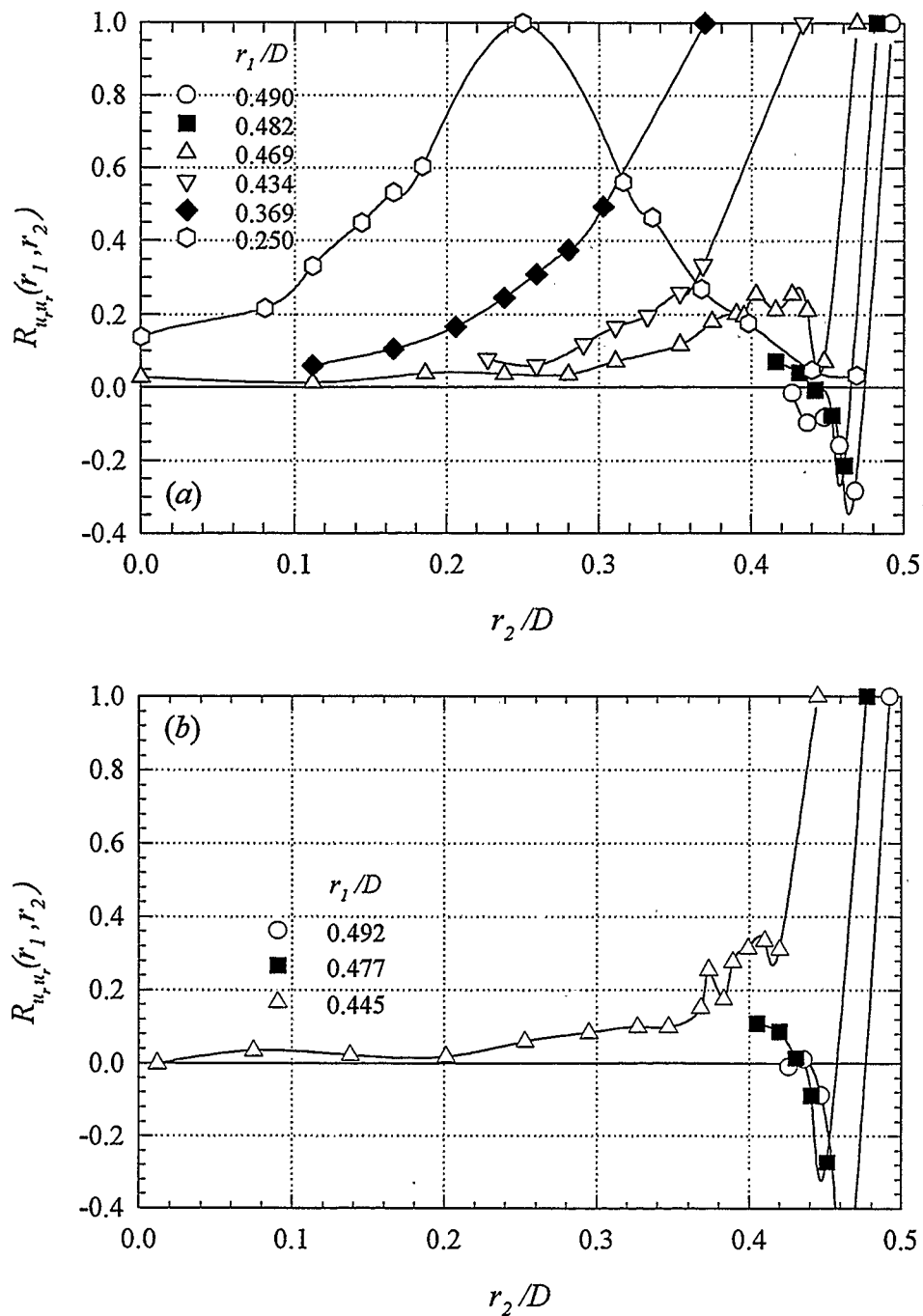


FIGURE 6.20. Two-point radial correlations of radial velocity $R_{u,u_r}(r_1, r_2)$:
(a) smooth surface ; (b) blade riblet surface.

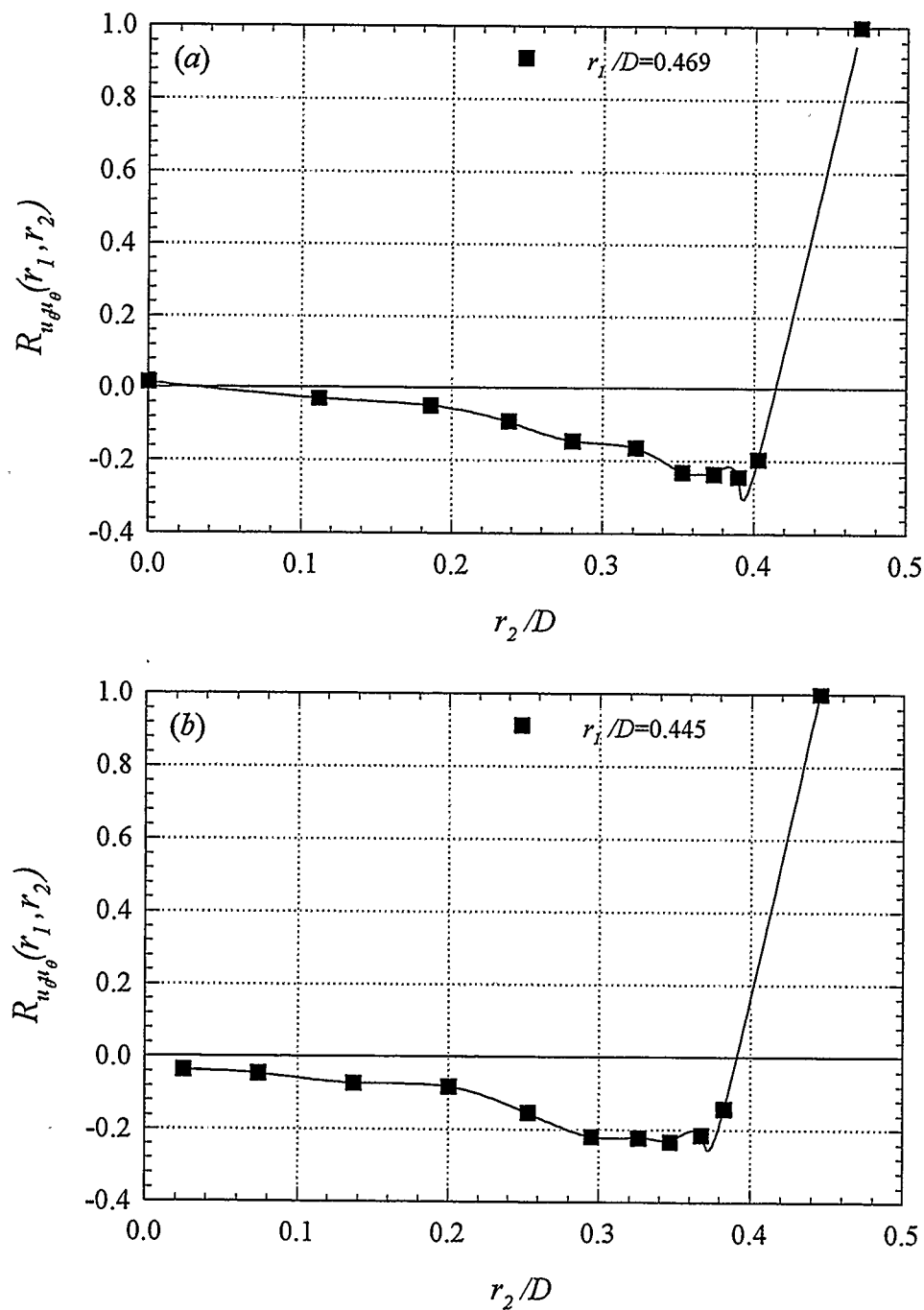


FIGURE 6.21. Two-point radial correlations of azimuthal velocity $R_{u_{\theta}u_{\theta}}(r_1, r_2)$:
 (a) smooth surface ; (b) blade riblet surface.

The final radial correlations presented are those of fluctuating shear stress $u_x u_r$, shown in figure 6.22(a, b). The trends are almost identical to those of the fluctuating

radial velocity with very narrow correlation lengths and strong negative correlations close to the wall. Very near the blade riblet surface, the correlation lengths are shorter with even stronger negative correlations.

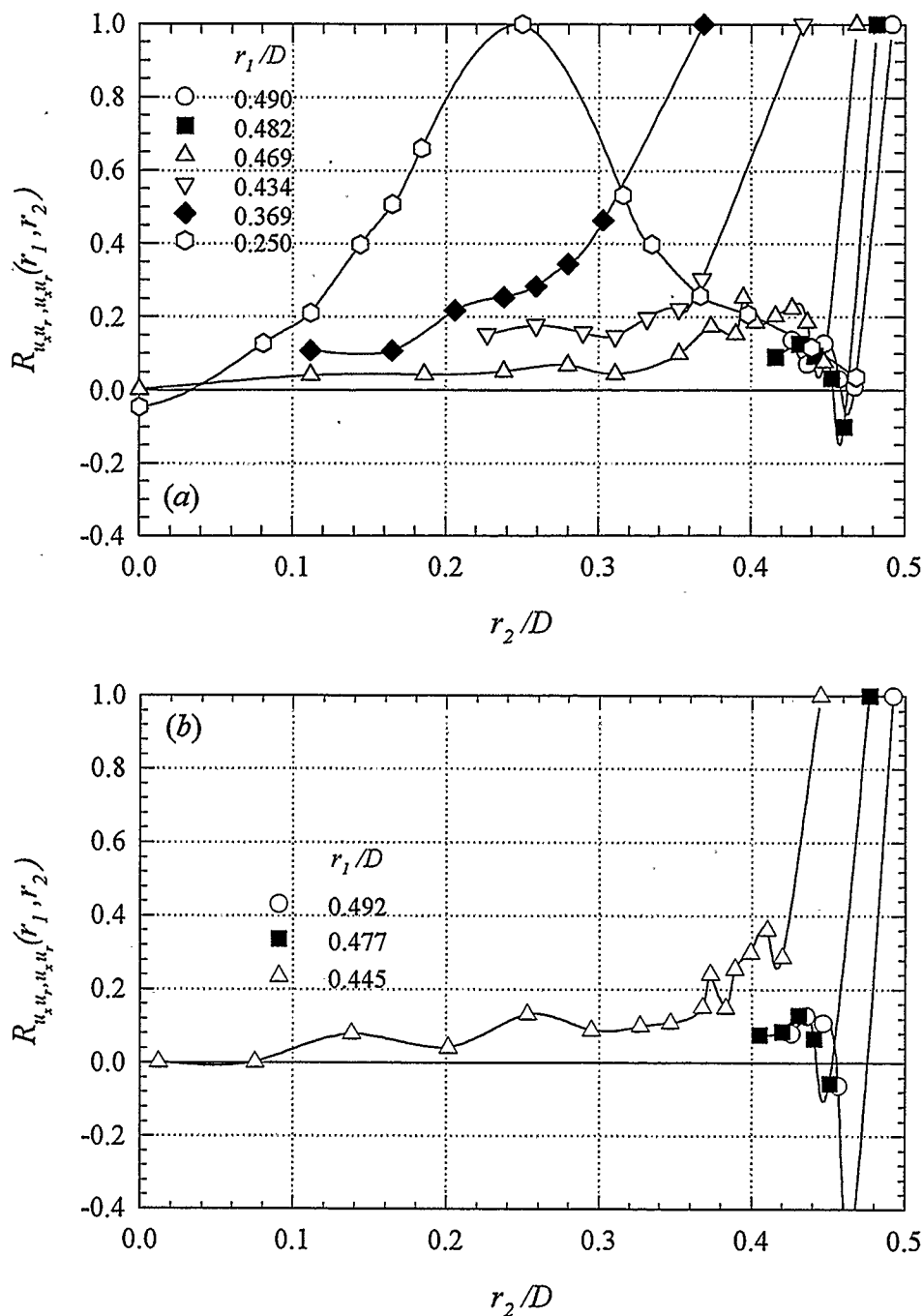


FIGURE 6.22. Two point radial correlations of Reynolds shear stress $R_{u_x u_r, u_x u_r}(r_1, r_2)$:

(a) smooth surface ; (b) blade riblet surface.

6.3.2 Azimuthal correlations

Turning now to the azimuthal correlations, the general correlation function is defined as

$$R_{uu}(r\theta_1, r\theta_2) = \frac{\overline{u(r\theta)_1 u(r\theta)_2}}{\overline{u'(r\theta)_1 u'(r\theta)_2}} \quad (6.8)$$

and is measured by fixing one probe and traversing the second probe in an azimuthal direction. Again, the streamwise fluctuating velocity over the smooth pipe surface is considered first (figure 6.23a). The correlation lengths at distances close to the wall are shorter and have regions of more negative correlation than at distances farther from the wall. Unfortunately, no azimuthal correlations in pipe flows have been previously measured to confirm this trend. However, the spanwise measurements of Antonia & Bisset (1990) in a boundary layer flow, at a somewhat higher Reynolds number, show similar trends although the present data indicate consistently shorter correlation lengths and regions of more negative correlation. The DNS results of Kim, Moin & Moser (1987) for a low Reynolds number channel flow compare quite closely with the present results. The two-point azimuthal correlations over the blade riblet surface, figure 6.23(b), indicate negligible differences compared with the smooth wall showing just slightly reduced azimuthal correlations over the riblet surface. Plotted in local wall units, the azimuthal correlations over the riblet surface are noticeably reduced. This result is in agreement with the image processed flow visualization measurements of Pulles (1988) but contrary to the single wire measurements of Gallagher & Thomas (1984). In polymer drag-reducing flows, the spanwise correlation was increased (Fortuna & Hanratty 1972), however, it is expected that a different drag reducing mechanism governs such flows considering that the peak streamwise turbulence intensity is increased while over riblets it is decreased.

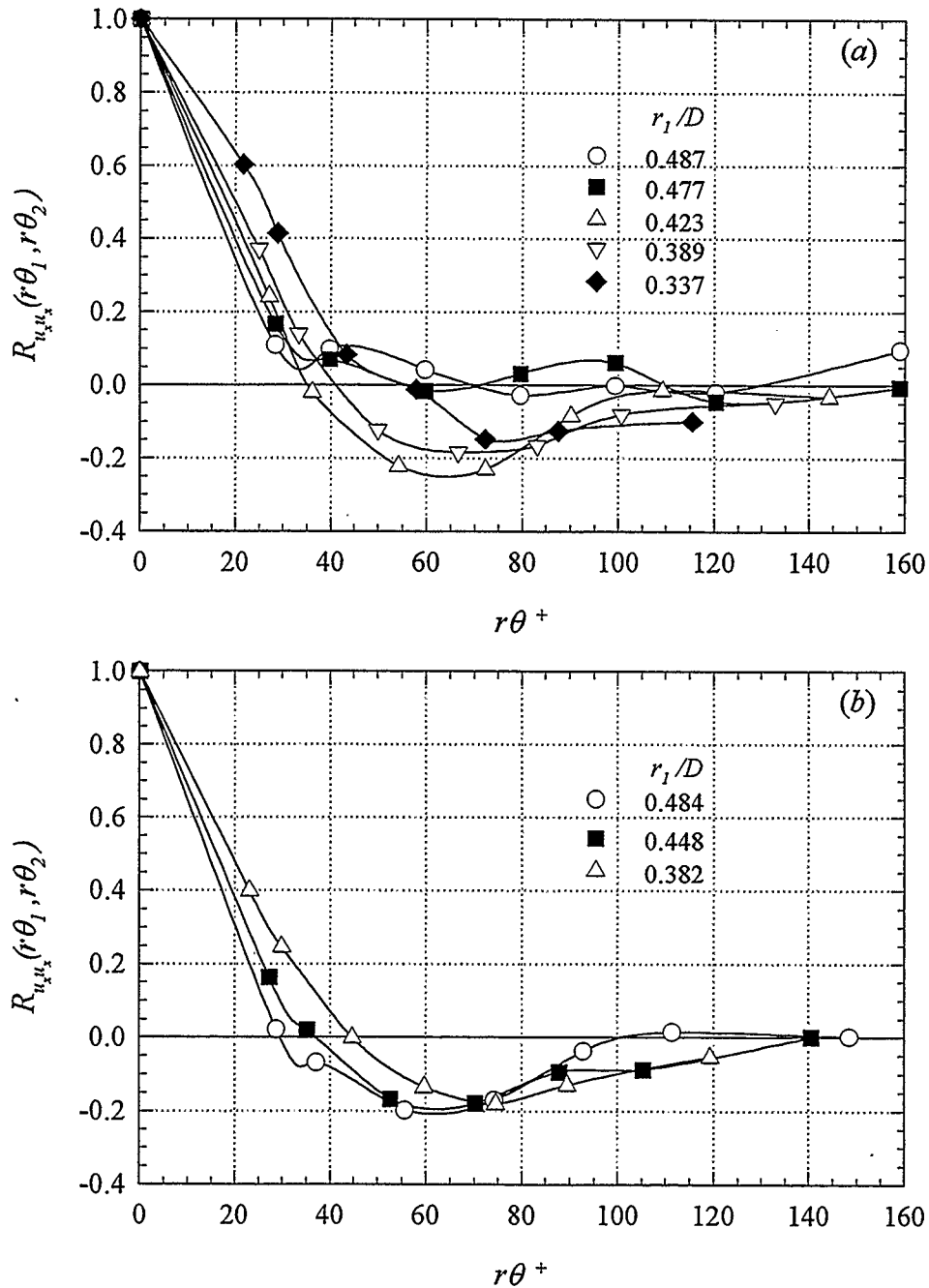


FIGURE 6.23. Two-point azimuthal correlations of streamwise velocity $R_{u_x u_x}(r\theta_1, r\theta_2)$:
(a) smooth surface ; (b) blade riblet surface.

Much like the radial correlation, the smooth wall azimuthal correlation of the radial velocity suggests regions of very concentrated vorticity in the near-wall region, as indicated by the very narrow azimuthal correlation lengths and negative correlation

coefficients in figure 6.24(a). Again, only negligible differences over the blade riblet surface, figure 6.24(b), are observed.

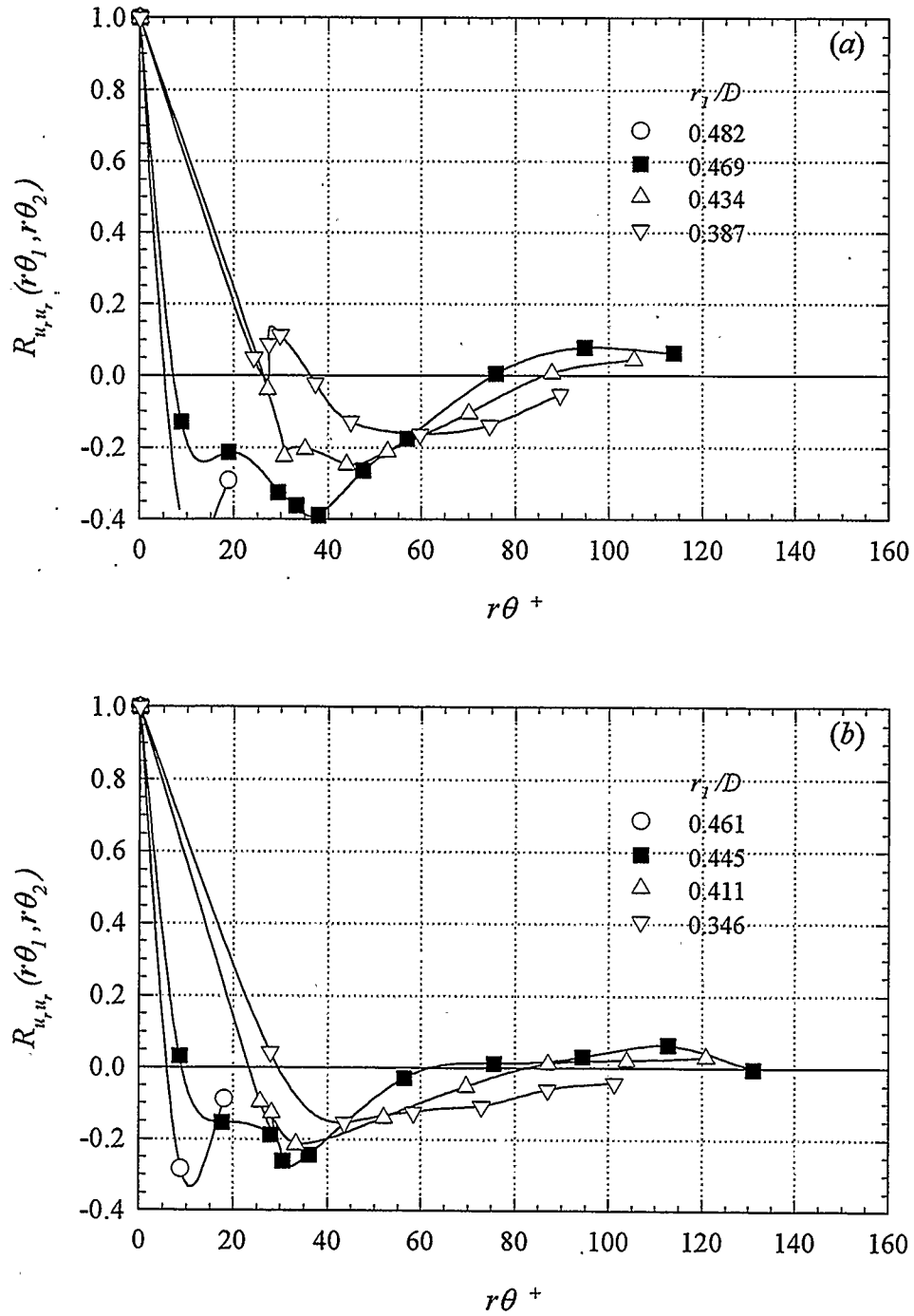


FIGURE 6.24. Two-point azimuthal correlations of radial velocity $R_{u,u_r}(r\theta_1, r\theta_2)$:
(a) smooth surface ; (b) blade riblet surface.

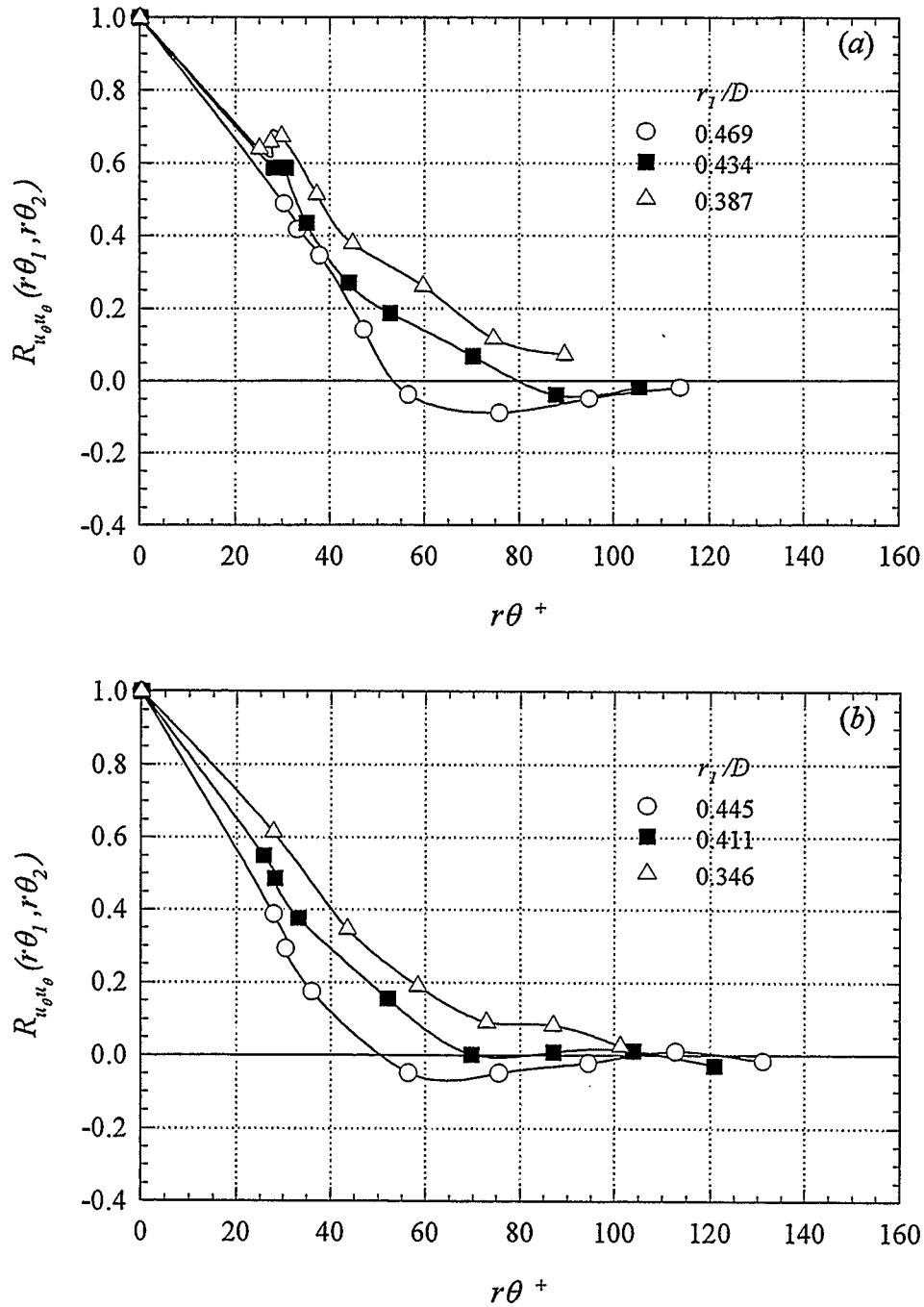


FIGURE 6.25. Two-point azimuthal correlations of azimuthal velocity $R_{u_\theta}(r\theta_1, r\theta_2)$:
(a) smooth surface ; (b) blade riblet surface.

The correlation of fluctuating azimuthal velocity over the smooth wall, shown in figure 6.25(a), indicates that this velocity component experiences the widest azimuthal correlation and as distance from the wall increases so does the width of the correlated

region. Again, there is no experimental data for comparison, only the channel flow DNS of Kim, Moin & Moser (1987) which shows good agreement. The same plot over the blade riblet surface indicates substantially narrower correlation distances, especially close to the rib surface (figure 6.25*b*).

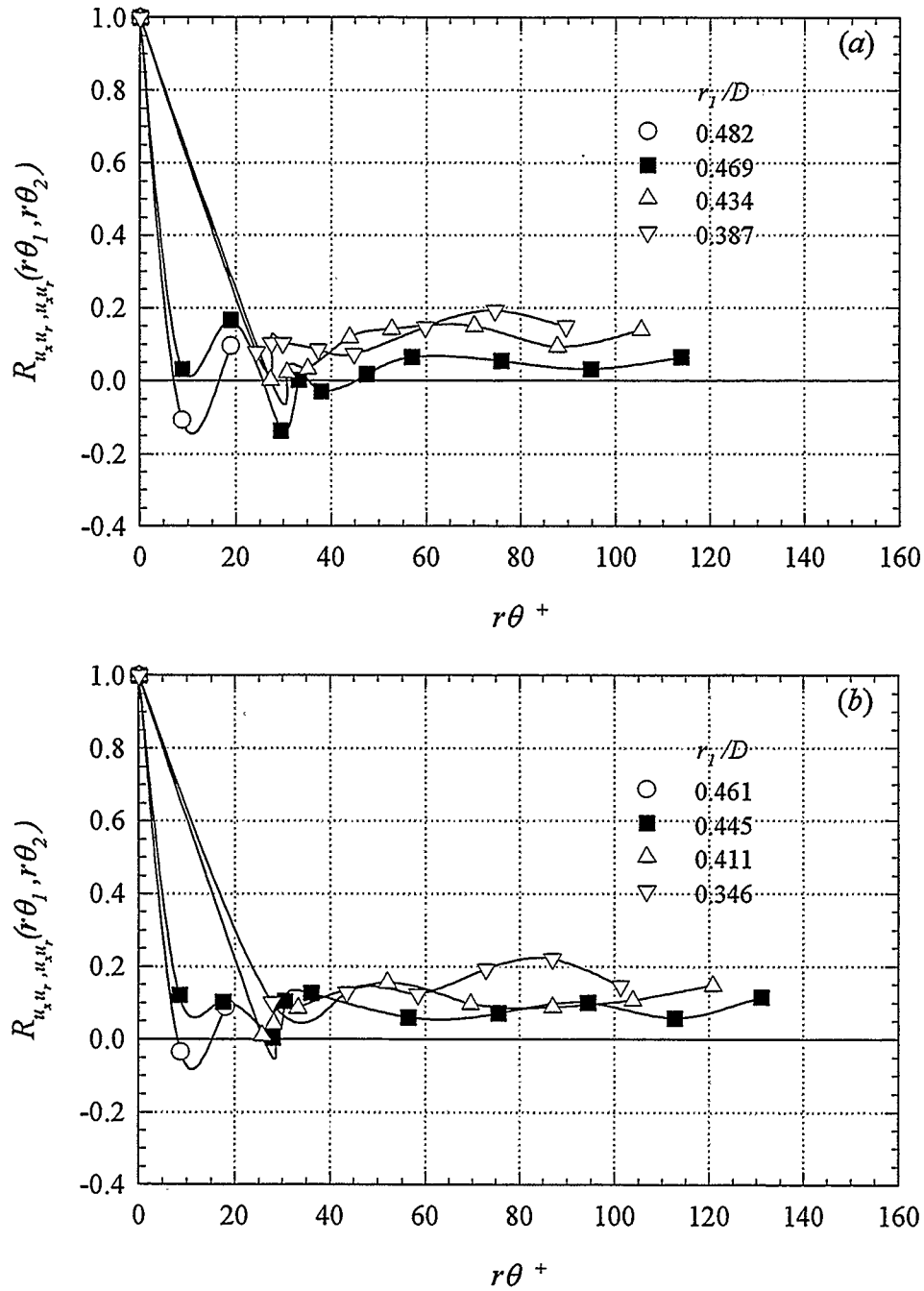


FIGURE 6.26. Two-point azimuthal correlations of Reynolds shear stress

$R_{u_x u_r, u_x u_r}(r\theta_1, r\theta_2)$: (a) smooth surface ; (b) blade riblet surface.

Lastly, the azimuthal correlations of fluctuating shear stress for the smooth and blade riblet surfaces are plotted in figure 6.26(a, b), respectively. Again, the trends are nearly the same as for the azimuthal correlation of radial velocity, with the riblets showing a negligible effect on this two-point correlation.

Summarizing, the measurement of radial and azimuthal two-point correlations over smooth and blade riblet surfaces indicates reductions in some correlation lengths in the near-wall region. Specifically, the correlation of radial velocity and shear stress is somewhat reduced in the radial direction. In the azimuthal direction, the streamwise velocity is slightly less correlated while the correlation of azimuthal velocity is substantially reduced. Generally, the space correlations suggest that narrow vortical structures are predominant in the near-wall region and interact with the riblets. The implications of these two-point space correlations in regards to a specific drag reducing mechanism are discussed in the following section.

6.4 Proposed Drag Reduction Mechanism

Clearly, one of the primary difficulties in determining the drag reducing mechanism for riblets stems from the incomplete understanding of dynamical processes in the near-wall region of turbulent flows over smooth surfaces. During the past decade, significant progress towards the establishment of cause-and-effect relationships for the observed flow behavior has been made by utilizing innovative experimental methods, DNS and new theoretical developments (e.g. Robinson 1990; Grass *et al.* 1991; Smith *et al.* 1991). A remarkably consistent aspect of these efforts is the emerging picture of flow dominated by intense vortex motions, wherein lies the key to turbulent shear stress

production mechanisms and, consequently, drag reduction. Several specific near-wall dynamical processes are considered next.

Smith *et al.* (1991) have effectively combined theoretical modeling studies and a number of 'kernel' experiments to elucidate some basic fluid dynamic phenomena believed to be relevant to turbulent wall flows. Instead of attempting to extract causal information from fully-developed turbulent flows, these 'kernel' experiments introduce controlled vortices into an otherwise laminar boundary layer and trace the resulting interaction through the use of hydrogen bubble wire and dye injection techniques. On the theoretical side, lagrangian numerical methods are used to calculate the inviscid temporal development of vortex lines over a background shear flow. A specific result of the experimental studies is the observation that low-speed streaks in the near-wall region can be induced by a streamwise vortex passing close to the surface. The vortex core induces the high and low-speed regions on the viscous flow near the wall which characterizes the near-wall streak structure. Furthermore, Smith *et al.* (1991) have shown that a convecting streamwise vortex close to the wall can induce a focused eruptive growth of the surface shear flow which becomes a dominant shear stress producing event. Additional details on the dynamics of near-wall turbulence are described by Smith *et al.* (1991).

Returning now to the azimuthal and radial correlation measurements of the present study, the presence of intense vortices in the near-wall region is confirmed by the very narrow (≈ 10 wall units) shear stress correlations perpendicular to the streamwise direction. Considering that drag-reduction with riblets of height greater than 20 wall units is never observed, it would appear that riblets interfere predominantly with the viscous-inviscid interactions of a convecting vortex structure over the surface shear flow. More specifically, the riblets provide a different shear flow boundary condition for motions induced by a vortex structure passing close to the surface. Smith *et al.*

(1990) have already suggested that riblets would inhibit the induction of lateral flow near the surface which can reduce the effectiveness of convecting vortices in provoking focused eruptions of the surface shear layer. The substantially reduced azimuthal correlation of the azimuthal velocity which was observed over the blade riblets and the reduced radial correlation distance of the radial velocity seem to quantitatively confirm this conjecture. Furthermore, the observation of Bechert *et al.* (1990) that cross-flow over riblet peaks will separate even in the limit of vanishing Reynolds number suggests that the induction of even weak lateral flow will create secondary streamwise vorticity at the riblet peaks. This would tend to weaken any surface layer eruptions due to the opposing sense of vorticity with respect to the vortex core which originally induced the lateral velocity. Such a process would also explain the negative skewness of radial velocity over the riblet valley since it would become more difficult to induce upward velocities in the riblet grooves. A schematic of the process described here is shown in figure 6.27 for clarification. Bacher & Smith (1985) originally proposed a very similar mechanism although they indicated that the primary function of the secondary vortices would be to weaken the streamwise vortices which spawned them. More importantly, however, it would appear that the secondary vortices weaken the surface layer eruptions.

The reduced azimuthal correlation distance of the azimuthal velocity also suggests that the near-wall sweep motions, which follow the focused eruptions, are restricted in their lateral movement. It could be argued that the riblets predominantly affect the large scale sweep motion near the wall, since the data of Brodkey *et al.* (1974) have shown that sweep events dominate close to the wall ($y^+ < 10$) while further away it is the ejection events which dominate. However, in the near-wall region where sweeps dominate, the contribution of the turbulent shear stress relative to the total shear stress is drastically reduced. This indicates that the ejection events, occurring somewhat

further away from the wall, make a far greater contribution to the shear stress. Thus, interference with the focused eruptions in the buffer region is more likely the prevailing effect of the riblets.

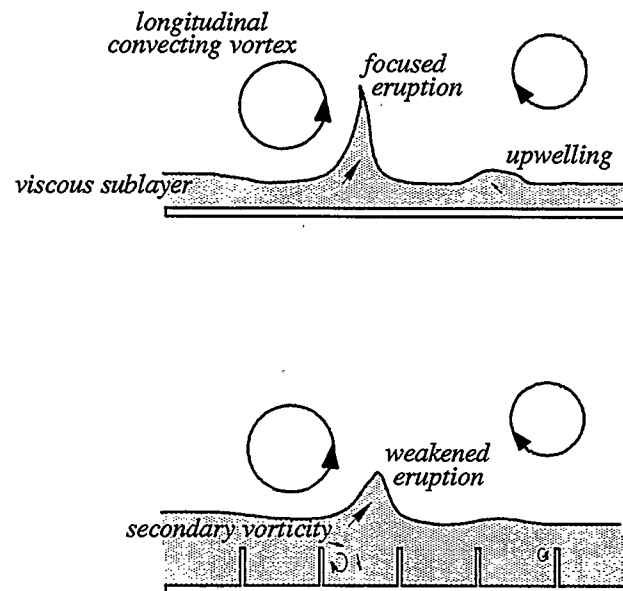


FIGURE 6.27. Schematic of proposed riblet drag reduction mechanism.

Further indirect support for an altered viscous-inviscid interaction as the primary drag reducing mechanism of riblets can be found by considering two other types of drag-reducing flows. Bruse *et al.* (1993) have measured small amounts of drag reduction (1.5 %) using streamwise aligned strings elevated above the wall, or a 'hairy' surface as they refer to it. Only when the strings are in very close proximity to the wall (one or two wall units) is a slight drag reduction observed since the strings act as rib-like structures. Movement farther away from the wall (only three or four wall units) results in a significant drag increase. Obviously, lateral velocity can be induced between the strings and the wall which could lead to elevated levels of wall shear stress and reduced interactions with the vortex core inducing the lateral velocities. In

polymer drag-reducing flows, on the other hand, the interaction of long-chain polymers with the intense vortex motion and viscous shear stress in the buffer region occurs directly, without the additional 'expense' of an increased surface area to procure the interaction—the result is substantially higher amounts of drag reduction than for riblet flows.

One additional mechanism will briefly be considered due to its perplexing nature. A particularly striking feature of the riblet DNS by Chu & Karniadakis (1993) is the presence of flow reversals within the triangular grooves. This finding has far-reaching implications since it suggests that flow separation within the grooves plays a role in the drag reduction process. Conceivably, the streamwise convection of a strong spanwise vortex over the riblet surface could induce local flow separations due to the induced adverse pressure gradient. Although this would result in a locally negative surface shear stress, such an occurrence would be accompanied by a strong shear-producing event farther away from the wall. Thus, it seems unlikely that flow reversals should be present in riblet flows. To test this hypothesis, a single wire probe was mounted deep within the blade grooves. Acknowledging that flow reversals are difficult to detect with hot-wire probes, a test was first performed to characterize the hot-wire bridge voltage signature during an actual controlled flow reversal. If, during normal operation, the positive-displacement blower in figure 6.1 is quickly brought to a halt, the rapid flow deceleration produces a momentary flow reversal in the pipe due to the restriction of the sonic nozzle. The trace in figure 6.28(a) indicates the character of the time signature for such a controlled flow disturbance. Notice the rectified voltage signal indicating the flow reversal and the final voltage level with no flow. When several lengthy high-rate acquisitions of the hot-wire signal under normal flow conditions were made, no evidence of this type of signature was found, as shown in a

typical time trace of bridge voltage in figure 6.28(b). The voltage level with no flow is also indicated for reference.

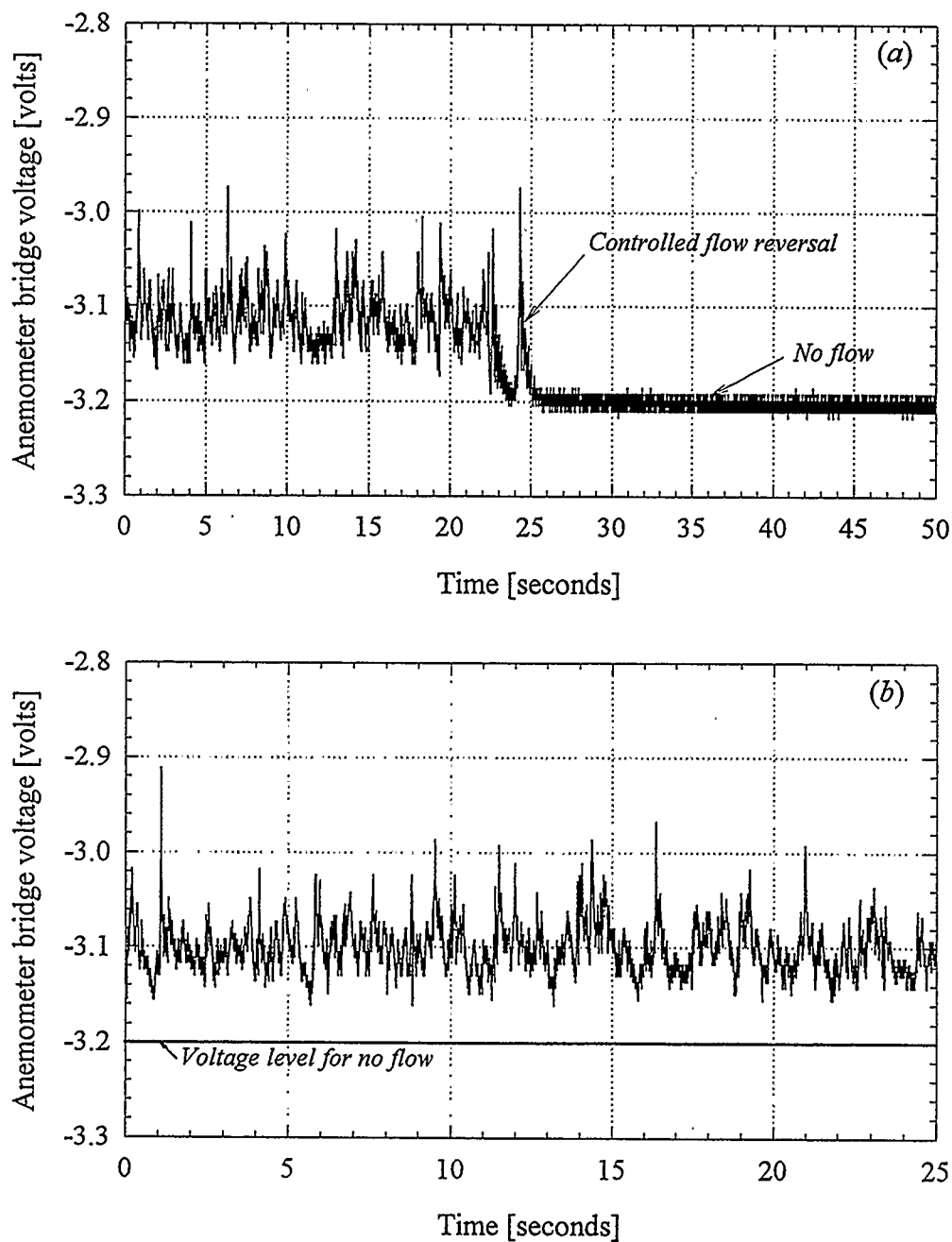


Figure 6.28. Experimental test for presence of flow reversals in a blade riblet valley (single wire probe located in riblet groove midway between valley floor and blade peak): (a) bridge voltage signature of controlled flow reversal; (b) bridge voltage signal during normal operation showing absence of flow reversals.

It would appear that there is no experimental evidence for the existence of flow reversals within riblet grooves in an overall favorable pressure gradient flow. The flow reversals observed in the DNS study (Chu & Karniadakis 1993) are perhaps products of the numerical scheme applied to the rather coarse streamwise grid (resolution ≈ 40 wall units) and somewhat insufficient spanwise domain of the simulation. In addition, the presence of modulatory velocity correlations in the streamwise direction and the non-random appearance of extended spanwise flow reversal regions in the simulation, would indicate a purely numerical effect. A grid independence check would certainly clarify this issue, since sufficient resolution in all directions is necessary to simulate near-wall dynamical processes (Zang 1991).

Based on evidence from the present radial and azimuthal velocity and shear stress correlations, 'kernel' experiments and theoretical considerations summarized by Smith *et al.* (1991), and viscous flow considerations outlined by Bruse *et al.* (1993), it seems that the alteration of the viscous-inviscid interaction process in the near-wall region is a plausible physical explanation of the riblet drag reduction mechanism.

Chapter 7

Conclusions

A detailed study of drag reduction in pipe flow with riblets has been conducted. The effect of small surface ribs or grooves on turbulent pipe flows was investigated from several perspectives in an endeavor to elucidate the drag reduction mechanism. First, friction factor measurements were carried out in smooth and riblet-lined pipes over a wide range of Reynolds numbers utilizing both laboratory and field experiments. Next, a theoretical study of the viscous effects near the wall was undertaken in order to determine whether drag reduction in laminar flow with ribbed pipes is possible. Lastly, an experimental study comparing the turbulence statistics and structure over a drag-reducing blade riblet surface and a smooth pipe wall was performed. A summary of the most important findings from this combined approach follows.

Friction factor measurements

Careful measurements of friction factor in smooth and riblet-lined pipes have provided unambiguous confirmation of drag reduction in turbulent pipe flow with properly sized riblets. Drag reduction of about 7 percent was attained at a non-dimensional height of about 15 viscous wall units using sharp-peaked triangular riblets of equal height and spacing. A significant amount of drag reduction already occurs at

very small non-dimensional riblet heights and riblet scaling trends in pipe flow were found to be virtually identical to those of channel or boundary layer flows. An experiment in which only half of the pipe periphery was covered with riblets resulted in drag reduction of about half that measured with a completely lined pipe. This test confirmed that the riblet drag reduction mechanism is a very localized phenomenon.

Sufficient experimental evidence was obtained from a field experiment to suggest that levels of drag reduction similar to that measured in the laboratory can be obtained in field applications. Furthermore, even higher levels of drag reduction can be expected with riblets in high Reynolds number flows since pipe walls with relatively small roughness are no longer hydraulically smooth.

Theoretical consideration of viscous effects

An analytical solution of laminar flow with blade type riblets established that, for a ribbed and smooth pipe of the same cross-sectional area, the ribbed pipe will always experience a drag increase, even if the ribs are small and infinitely thin. However, a comparison of smooth and ribbed pipes using an effective diameter based on the apparent origin of the velocity profile (or protrusion height) indicates that the shear stress remains unchanged. The result stresses the importance of knowing the effective diameter when making statements about friction losses in ribbed pipes and also implies that viscous effects alone cannot explain the observed drag reduction in turbulent flow.

However, the viscous sublayer within turbulent flows does play an important role in the drag reducing mechanism since proper scaling parameters for riblet drag reduction result from the consideration of longitudinal and cross-flow protrusion heights in viscous flows. If the non-dimensional riblet height is scaled with the ratio of

longitudinal protrusion height to riblet height, optimum drag-reduction for several different geometrical riblet shapes occurs at a value of $h^+/(1-h_{pl}/h) \approx 15$. Furthermore, scaling the level of drag reduction with the shape factor $(1-h_{pc}/h) / \Delta h/s$ provides a reasonable collapse of the data. Thus, an almost universal drag reduction curve for riblets has been obtained.

Experimental investigation of turbulence structure

Single wire and X-wire anemometry techniques were used to obtain detailed two-point radial and azimuthal space correlations of all three velocity components and the turbulent shear stress in the near-wall region over a smooth pipe wall, a drag-reducing blade riblet surface and an approximately drag-neutral scalloped riblet pipe. Profiles of higher-order statistics were also measured. The findings and their implications towards the drag reduction mechanism are presented here.

The azimuthal variation of the mean streamwise velocity was restricted to a region within two riblet heights above the rib valley for drag-reducing blade riblets. This indicates that only the turbulence structures very near the riblet surface experience the direct effect of individual ribs while dynamical processes occurring further from the wall are affected in a more indirect manner. When non-dimensionalized with wall units based on the local friction velocity, the streamwise velocity profile over the drag-reducing riblet surface is shifted upwards in the outer region; an observation which is consistent with other drag-reducing flows.

Measurements of turbulence intensity indicated that all three velocity components were reduced over the riblet surface when scaled with outer variables, such as mean centerline velocity, although there would appear to be some evidence that the

turbulence intensity over riblet surfaces scales with the wall shear stress. When scaled with the local mean streamwise velocity, the measurements over the rib valley indicate large reductions in streamwise intensity accompanied by increases in the radial intensity. These results suggest that weak streamwise vorticity is generated between the ribs which enhances the level of radial fluctuations in the otherwise viscous, slow-moving fluid in and above the riblet valley.

Comparing the diagonal components of the stress anisotropy tensor, the inter-component transfer of kinetic energy from the streamwise to the spanwise component is impeded in the buffer region over the riblet surface. In the region just above the riblet valley the local kinetic energy transfer appears to become more efficient. The current results would indicate that cross-stream and radial mixing are enhanced within the riblet valleys but decrease in the region farther above the ribs. A similar conclusion results when the turbulent shear stress is normalized on the local velocity; measurements indicate that the *local* momentum exchange just over the riblet valley is larger than over a smooth surface or the riblet peaks. This simply suggests that secondary motions not present in smooth wall flows are produced by the riblets and azimuthal velocities are more difficult to induce over the riblet surface. However, the riblet surface decreases the frequency of important high shear stress producing events, as indicated by the higher skewness and flatness factors of the turbulent shear stress observed over both the rib peaks and valleys.

Compared with a smooth wall, an increase in both the skewness and flatness factors of streamwise velocity is observed over the rib valley while over the rib peak both are reduced. Thus, large positive streamwise fluctuations occur less frequently above the riblet valley. The flatness factor of the azimuthal velocity is increased substantially over the rib valley indicating that riblets also reduce the number of large azimuthal fluctuations.

The most significant difference between flow over a smooth wall and a drag-reducing riblet surface is found in the skewness factor of the radial velocity. Over the rib valley the skewness factor becomes strongly negative whereas over the rib peak, as well as the smooth wall, it is positive. This result suggests that it is more difficult to induce upward velocities in the riblet groove than downward velocities. Thus, the increased local intensity of radial velocity fluctuations observed over the riblet valley would be due to larger radial velocities downward into the grooves.

Radial two-point velocity correlations over the smooth pipe wall indicate that the streamwise velocity is quite widely correlated compared with the azimuthal and radial velocities which experience very narrow correlation lengths near the wall. Very close to the wall, strong negative correlations of radial velocity and fluctuating shear stress are observed. These correlation lengths signify streamwise convecting vortical structures of limited radial dimension in the buffer region. Furthermore, all radial correlations are somewhat reduced over the riblet surface indicating that the ribs interact with these vortex structures.

Turning to the two-point azimuthal correlations, the low and high-speed streamwise velocity regions characteristic of the near-wall streak structure are observed. Over the riblet surface, the spanwise extent of this structure is somewhat reduced. Similar to the radial correlations, narrow azimuthal correlation lengths of both radial velocity and fluctuating shear stress were observed near the wall, with only slight reductions over the riblet surface. However, for the azimuthal velocity, a substantial reduction in the azimuthal correlation length over the riblet surface was observed. The latter observation indicates that lateral flow near the riblet surface is reduced.

Together, the two-point radial and azimuthal correlations of all three velocity components and fluctuating shear stress provide a more complete picture which

confirms the existence of intense vortical structures in the near-wall region. The streamwise convecting vortices have significant components of spanwise and streamwise vorticity and a characteristic dimension, perpendicular to the vortex core, of less than 20 wall units.

The most important conclusion of this study is that riblets appear to inhibit the induction of lateral flow near the surface, thus reducing the ability of convecting vortices to provoke focused eruptions of the surface layer. Specifically, vortex induced cross-flow above the ribs will create secondary streamwise vorticity of the opposite sense at the rib peaks which would tend to weaken any surface layer eruptions. Numerous measurements of single point statistics and two-point radial and azimuthal velocity correlations provide both qualitative and quantitative support of this drag reducing mechanism.

References

- ANTONIA, R.A. & BISSET, D.K.** 1990 Spanwise structure in the near-wall region of a turbulent boundary layer. *J. Fluid Mech.* **210**, 437-458.
- BACHER, E.V. & SMITH, C.R.** 1985 A Combined Visualization-Anemometry Study of the Turbulent Drag Reducing Mechanisms of Triangular Micro-Groove Surface Modifications. *ALAA Paper 85-0548*.
- BATH, T.D.** 1968 Channeled Flow at the Pipe Surface in Gas Transmission Pipelines. *MRI Project No. 3123-C, Final Report*, Midwest Research Institute, Kansas City, Missouri.
- BECHERT, D.W.** 1987 Experiments on Three-Dimensional Riblets. In *Proc. Turbulent Drag Reduction by Passive Means, Royal Aeronautical Society, London, Sept. 15-17, 2*, 425-431.
- BECHERT, D.W. & BARTENWERFER, M.** 1989 The viscous flow on surfaces with longitudinal ribs. *J. Fluid Mech.* **206**, 105-125.
- BECHERT, D.W., BARTENWERFER, M. & HOPPE, G.** 1990 Turbulent drag reduction by non-planar surfaces—a survey on the research at TU/DLR Berlin. In *Structure of Turbulence and Drag Reduction* (ed. A. Gyr) *IUTAM Symposium Zurich, Switzerland, July 25-28, 1989*, Springer-Verlag, 525-543.
- BECHERT, D.W., BARTENWERFER, M., HOPPE, G. & REIF, W.E.** 1986 Drag reduction mechanisms derived from shark skin. *Proc. 15th Congress of the International Council of the Aeronautical Sciences, London, Sept. 7-12, Paper ICAS-86-1.8.3*, 1044-1068.

- BENEDICT, R.P.** 1984 *Fundamentals of Temperature, Pressure and Flow Measurements*, 3rd. Ed., John Wiley & Sons.
- BENHALILOU, M., ANSELMET, F., LIANDRAT, J. & FULACHIER, L.** 1991 Experimental and numerical investigation of a turbulent boundary layer over riblets. In *Proc. 8th Symposium on Turbulent Shear Flows, Munich, Sept. 9-11, Paper 18-5*.
- BLAKE, K.A.** 1976 The design of piezometer rings. *J. Fluid Mech.* **78**, 415-428.
- BRODKEY, R.S., WALLACE, J.M. & ECKELMANN, H.** 1974 Some properties of truncated turbulence signals in bounded shear flows. *J. Fluid Mech.* **63**, 209.
- BROWNE, L.W.B., ANTONIA, R.A. & SHAH, D.A.** 1988 Selection of wires and wire spacing for X-wires. *Experiments in Fluids* **6**, 286-288.
- BRUSE, M., BECHERT, D.W., VAN DER HOEVEN, J.G.TH., HAGE, W. & HOPPE, G.** 1993 Experiments with conventional and with novel adjustable drag-reducing surfaces. In *Near-Wall Turbulent Flows* (ed. R.M.C. So, C.G. Speziale & B.E. Launder) Elsevier, 719-738.
- CARPENTER, P.W.** 1990 Status of Transition Delay Using Compliant Walls. In *Viscous Drag Reduction in Boundary Layers* (ed. D.M. Bushnell & J.N. Hefner) *Prog. Astronautics and Aeronautics* **123**, AIAA, 79-113.
- CHOI, H., MOIN, P. & KIM, J.** 1991 On the effect of riblets in fully developed laminar channel flows. *Phys. Fluids A* **3**(8), 1892-1896.
- CHOI, H., MOIN, P. & KIM, J.** 1992 Direct numerical simulation of turbulent flow over riblets. *CTR Manuscript* **137**.

- CHOI, K.-S.** 1989 Near-wall structure of a turbulent boundary layer with riblets. *J. Fluid Mech.* **208**, 417-458.
- CHU, D.C. & KARNIADAKIS, G.E.** 1991 Numerical investigation of drag reduction in flow over surfaces with streamwise aligned riblets. *AIAA Paper 91-0518*.
- CHU, D.C. & KARNIADAKIS, G.E.** 1993 A direct numerical simulation of laminar and turbulent flow over riblet-mounted surfaces. *J. Fluid Mech.* **250**, 1-42.
- CORRSIN, S. & KISTLER, A.L.** 1954 The free-stream boundaries of turbulent flows. *NACA Tech. Note 3133*.
- COUSTOLS, E., COUSTEIX, J. & BELANGER, J.** 1987 Drag reduction performance on riblet surfaces and through outer layer manipulators. In *Proc. Turbulent Drag Reduction by Passive Means, Royal Aeronautical Society, London, Sept. 15-17, 2*, 250-289.
- DJENIDI, L., ANSELMET, F. & FULACHIER, L.** 1987 Influence of a riblet wall on boundary layers. In *Proc. Turbulent Drag Reduction by Passive Means, Royal Aeronautical Society, London, Sept. 15-17, 2*, 310-329.
- DJENIDI, L., LIANDRAT, J., ANSELMET, F. & FULACHIER, L.** 1989 Numerical and experimental investigation of the laminar boundary layer over riblets.. *Applied Scientific Research* **46**, No. 3, 263-270.
- DURST, F., JOVANOVIC, J. & SENDER, J.** 1993 Detailed measurements of the near wall region of turbulent pipe flow. In *Proc. Fluids Engineering Conference, Washington D.C., June 20-24, FED-Vol. 146*.

- EGGELS, J.G.M., UNGER, F., WEISS, M.H., WESTERWEEL, J., ADRIAN, R.J., FRIEDRICH, R. & NIEUWSTADT, F.T.M. 1993 Fully developed turbulent pipe flow: a comparison between direct numerical simulation and experiment. (to be published in *J. Fluid Mech.*).
- FORTUNA, G. & HANRATTY, T.J. 1972 The influence of drag-reducing polymers on turbulence in the viscous sublayer. *J. Fluid Mech.* **53**, 575-586.
- GALLAGHER, J.A. & THOMAS, A.S.W. 1984 Turbulent Boundary Layer Characteristics Over Streamwise Grooves. *AIAA Paper 84-2185*.
- GRASS, A.J., STUART, R.J. & MANSOUR-TEHRANI, M. 1991 Vortical structures and coherent motion in turbulent flow over smooth and rough boundaries. *Phil. Trans. of R. Soc. Lond. A*, **336**, 35-65.
- HINZE, J.O. 1975 *Turbulence*, 2nd Ed., McGraw-Hill.
- HOOSHMAND, A. 1985 An Experimental Investigation of the Influence of a Drag Reducing, Longitudinally Aligned, Triangular Riblet Surface on the Velocity and Streamwise Vorticity Fields of a Zero-Pressure Gradient Turbulent Boundary Layer. *Ph.D. Dissertation*, University of Maryland.
- HOOSHMAND, A., YOUNGS, R.A., WALLACE, J.M. & BALINT, J.-L. 1983 An Experimental Study of Changes in the Structure of a Turbulent Boundary Layer Due to Surface Geometry Changes. *AIAA Paper 83-0230*.
- KENNEDY, J.F., HSU, S.-T. & LIN, J.-T. 1973 Turbulent Flows Past Boundaries with Small Streamwise Fins. *Journal of the Hydraulics Division, Proceedings of the American Society of Civil Engineers* **99**, No. HY4, 605-616.
- KIM, J., MOIN, P. & MOSER, R. 1987 Turbulence statistics in fully developed channel flow at low Reynolds number. *J. Fluid Mech.* **177**, 133-166.

- KLEBANOFF, P.S.** 1954 Characteristics of turbulence in a boundary layer with zero pressure gradient. *NACA Tech. Note* 3178.
- KLINE, S.J. & MCCLINTOCK, F.A.** 1953 Describing Uncertainties in Single-Sample Experiments. *Mechanical Engineering*, 3-8.
- KLINE, S.J., REYNOLDS, W.C., SCHRAUB, F.A. & RUNSTADLER, P.W.** 1967 The structure of turbulent boundary layers. *J. Fluid Mech.* 30, 741-773.
- KLINE, S.J. & RUNSTADLER, P.W.** 1959 Some Preliminary Results of Visual Studies of the Flow Model of the Wall Layers of the Turbulent Boundary Layer. *J. Applied Mechanics, Transactions of the ASME, Series E.* 166-170.
- KRAMER, M.** 1939 Einrichtung zur Verminderung des Reibungswiderstands. *Reichspatentamt, Patentschrift Nr. 669897, Klasse 62b, Gruppe 408.* Patentierte vom 17. März 1937 an.
- LAUFER, J.** 1954 The structure of Turbulence in Fully Developed Pipe Flow. *NACA Technical Report* 1174.
- LAUNDER, B.E. & LI, S.** 1989 A numerical study of riblet effects on laminar flow through a plane channel. *Applied Scientific Research* 46, No. 3, 271-279.
- LEUTHEUSSER, H.J.** 1963 Turbulent Flow in Rectangular Ducts. *Journal of the Hydraulics Division, Proceedings of the American Society of Civil Engineers* 89, No. HY3, 1-19.
- LIU, C.K., KLINE, S.J. & JOHNSTON, J.P.** 1966 An experimental study of turbulent boundary layers on rough walls. *Report MD-15*, Thermosciences Division, Department of Mechanical Engineering, Stanford University.
- LIU, K.N., CHRISTODOULOU, C., RICCIUS, O. & JOSEPH, D.D.** 1990 Drag Reduction in Pipes Lined with Riblets. In *Structure of Turbulence and Drag Reduction* (ed. A. Gyr) *IUTAM Symposium Zurich, Switzerland, July 25-28, 1989*, Springer-Verlag, 545-551.

- LUCHINI, P., MANZO, F. & POZZI, A. 1991 Resistance of a grooved surface to parallel flow and cross-flow. *J. Fluid Mech.* **228**, 87-109.
- LYNN, T.B., GERICH, D.A. & BECHERT, D.W. 1989 LEBU-Manipulated Flat Plate Boundary Layers: Skin Friction and Device Drag Measured Directly. presented at: *IAHR Drag Reduction '89 Conference*, Davos, Switzerland, July 31-August 3.
- MERKLE, C.L. & DEUTSCH, S. 1990 Drag Reduction in Liquid Boundary Layers by Gas Injection. In *Viscous Drag Reduction in Boundary Layers* (ed. D.M. Bushnell & J.N. Hefner) *Prog. Astronautics and Aeronautics* **123**, AIAA, 351-412.
- MOTIER, J.F. & CARRIER, A.M. 1989 Recent Studies on Polymer Drag Reduction in Commercial Pipelines. In *DRAG REDUCTION IN FLUID FLOWS: Techniques for Friction Control* (ed. R.H.J. Sellin & R.T. Moses) Ellis Horwood, 197-204.
- NAGIB, H.M., WARK, C.E. & NAGUID, A.M. 1989 Effects of Blade Manipulators on Turbulence Production and Why They Are Not LEBUs. In *DRAG REDUCTION IN FLUID FLOWS: Techniques for Friction Control* (ed. R.H.J. Sellin & R.T. Moses) Ellis Horwood, 107-114.
- NAKAO, S.-I. 1991 Application of V Shape Riblets to Pipe Flows. *J. Fluids Engineering* **113**, 587-590.
- NIKURADSE, J. 1926 Untersuchungen über die Geschwindigkeitsverteilung in turbulenten Strömungen. *Forsch. Arb. Ing.-Wes.* **281**.
- NIKURADSE, J. 1930 Turbulente Strömung in nichtkreisförmigen Rohren. *Ingenieur-Archiv* **1**, 306-332.
- NIKURADSE, J. 1932 Gesetzmäßigkeiten der turbulenten Strömung in glatten Rohren. *Forsch. Arb. Ing.-Wes.* **356**.
- NIKURADSE, J. 1933 Strömungsgesetze in rauhen Rohren. *Forsch. Arb. Ing.-Wes.* **361**.

- NITSCHKE, P.** 1983 Experimentelle Untersuchung der turbulenten Strömung in glatten und längsgerillten Rohren. *Max-Planck-Institut für Strömungsforschung, Göttingen, Bericht 3/1983*, Diplomarbeit (M.Sc. Thesis).
- PARK, S.-R. & WALLACE, J.M.** 1993 Flow field alteration and viscous drag reduction by riblets in a turbulent boundary layer. In *Near-Wall Turbulent Flows* (ed. R.M.C. So, C.G. Speziale & B.E. Launder) Elsevier, 749-760.
- POLLARD, A., SAVILL, A.M. & THOMANN, H.** 1989 Turbulent pipe flow manipulation: some experimental and computational results for single manipulator rings. *Applied Scientific Research* **46**, No. 3, 281-290.
- PRANDTL, L.** 1925 Über die ausgebildete Turbulenz. *Zeitschrift für angewandte Mathematik und Mechanik* **5**, 136-139.
- PULLES, C.J.A.** 1988 Drag reduction of turbulent boundary layers by means of grooved surfaces. *Ph.D. Thesis*, Technical University of Eindhoven.
- PULLES, C.J.A., KRISHNA PRASAD, K. & NIEUWSTADT, F.T.M.** 1989 Turbulence measurements over longitudinal micro-grooved surfaces. *Applied Scientific Research* **46**, No. 3, 197-208.
- REIDY, L.W. & ANDERSON, G.W.** 1988 Drag reduction for external and internal boundary layers using riblets and polymers. *AIAA Paper 88-0138*.
- ROBINSON, S.K.** 1990 A review of vortex structures and associated coherent motions in turbulent boundary layers. In *Structure of Turbulence and Drag Reduction* (ed. A. Gyr) *IUTAM Symposium Zurich, Switzerland, July 25-28, 1989*, Springer-Verlag, 23-50.
- ROHR, J., ANDERSON, G.W. & REIDY, L.W.** 1989 An Experimental Investigation of the Drag Reducing Effects of Riblets in Pipes. In *DRAG REDUCTION IN FLUID FLOWS: Techniques for Friction Control* (ed. R.H.J. Sellin & R.T. Moses) Ellis Horwood, 263-270.

- RUNSTADLER, P.W., KLINE, S.J. & REYNOLDS, W.C.** 1963 An experimental investigation of the flow structure of the turbulent boundary layer. *Report MD-8*, Thermosciences Division, Department of Mechanical Engineering, Stanford University.
- SAVILL, A.M.** 1987 Effects of Turbulent Boundary Layer Structure of Longitudinal Riblets Alone and in Combination with Outer Layer Devices. In *Flow Visualization IV: Proceedings of the 4th International Symposium on Flow Visualization*, Paris (ed. C. Charnay) Hemisphere, 303.
- SCHLICHTING, H.** 1979 *Boundary-Layer Theory*, 7th Ed., McGraw-Hill.
- SMITH, C.R., WALKER, J.D.A., HAIDARI, A.H. & SOBRUN, U.** 1991 On the dynamics of near-wall turbulence. *Phil. Trans. of R. Soc. Lond. A*, **336**, 131-175.
- SMITH, C.R., WALKER, J.D.A., HAIDARI, A.H. & TAYLOR, B.K.** 1990 Hairpin vortices in turbulent boundary layers: the implications for reducing surface drag. In *Structure of Turbulence and Drag Reduction* (ed. A. Gyr) *IUTAM Symposium Zurich, Switzerland, July 25-28, 1989*, Springer-Verlag, 51-58.
- SOLIMAN, H.M. & FEINGOLD, A.** 1977 Analysis of Fully Developed Laminar Flow in Longitudinal Internally Finned Tubes. *The Chemical Engineering Journal* **14**, 119-128.
- STROHL, A. & COMTE-BELLOT, G.** 1973 Aerodynamic effects due to configuration of x-wire anemometers. *J. Appl. Mech.* **40**, 661-666.
- SUZUKI, Y. & KASAGI, H.** 1993 Drag Reduction Mechanism on Micro-grooved Riblet Surface. In *Near-Wall Turbulent Flows* (ed. R.M.C. So, C.G. Speziale & B.E. Launder) Elsevier, 709-718.
- TAYLOR, G.I.** 1915 Eddy motion in the atmosphere. *Philosophical Transactions of the Royal Society of London, Series A*, **215**, 1-26.

- THEODORSEN, T.** 1952 Mechanism of turbulence. *2nd Midwestern Conf. on Fluid Mech., Ohio State University*, 1-18.
- TOMS, B.A.** 1949 Some Observations of the Flow of Linear Polymer Solutions Through Straight Tubes at Large Reynolds Numbers. *Proc. First International Congress on Rheology, Vol. II*, 135-141.
- TOWNSEND, A.A.** 1956 *The Structure of Turbulent Shear Flow*. Cambridge University Press.
- TUTU, N.K. & CHEVRAY, R.** 1975 Cross-wire anemometry in high intensity turbulence. *J. Fluid Mech.* **71**, 785-800.
- VIRK, P.S.** 1975 Drag reduction fundamentals. *AIChE Journal* **21**, 625-656.
- VIRK, P.S. & WAGGER, D.L.** 1990 Aspects of Mechanisms in Type B Drag Reduction. In *Structure of Turbulence and Drag Reduction* (ed. A. Gyr) *IUTAM Symposium Zurich, Switzerland, July 25-28, 1989*, Springer-Verlag, 201-213.
- VUKOSLAVCEVIC, P., WALLACE, J.M. & BALINT, J.-L.** 1987 On the mechanism of viscous drag reduction using streamwise aligned riblets: a review with new results. In *Proc. Turbulent Drag Reduction by Passive Means, Royal Aeronautical Society, London, Sept. 15-17, 2*, 290-309.
- WALLACE, J.M., ECKELMANN, H. & BRODKEY, R.S.** 1972 The wall region in turbulent shear flows. *J. Fluid Mech.* **54**, 39.
- WALSH, M.J.** 1980 Drag Characteristics of V-Groove and Transverse Curvature Riblets. In *Viscous Flow Drag Reduction* (ed. G.R. Hough) *Prog. Astronautics and Aeronautics* **72**, AIAA, 168-184.

- WALSH, M.J. 1982 Turbulent Boundary Layer Drag Reduction Using Riblets. *AIAA Paper 82-0169*.
- WALSH, M.J. 1990 Riblets. In *Viscous Drag Reduction in Boundary Layers* (ed. D.M. Bushnell & J.N. Hefner) *Prog. Astronautics and Aeronautics* **123**, AIAA, 203-261.
- WALSH, M.J. & WEINSTEIN, L.M. 1978 Drag and Heat Transfer on Surfaces with Small Longitudinal Fins. *AIAA Paper 78-1161*
- WESTERWEEL, J., ADRIAN, R.J., EGGELS, J.G.M. & NIEUWSTADT, F.T.M. 1993 Measurements with particle image velocimetry of fully developed turbulent pipe flow at low Reynolds number. In *Laser applications in Fluid Mechanics* (ed. R.J. Adrian *et al.*). Springer-Verlag.
- WILKINSON, S.P. & LAZOS, B.S. 1987 Direct Drag and Hot-Wire Measurements on Thin-Element Riblet Arrays. In *IUTAM Symposium on Turbulence Management and Relaminarization* (ed. H.W. Liepmann & R. Narasimha) *Bangalore, India, January 19-23*. Springer-Verlag.
- WILLMARTH, W.W. & LU, S.S. 1972 Structure of the Reynolds stress near the wall. *J. Fluid Mech.* **55**, 65-92.
- ZANG, T.A. 1991 Numerical simulation of the dynamics of turbulent boundary layers: perspectives of a transition simulator. *Phil. Trans. of R. Soc. Lond. A*, **336**, 95-102.